Structures and dynamics of the subcontinental lithospheric mantle over the Central and Eastern North American continent, constrained by numerical modeling based on tomography models

by

Jayasamudi Medini Abeysinghe Abeysinghe Mudiyanselage

B.S., University of Peradeniya, 2022

A THESIS

submitted in partial fulfillment of the requirements for the degree

MASTER OF SCIENCE

Department of Geology
College of Arts and Sciences

KANSAS STATE UNIVERSITY
Manhattan, Kansas

2026

Approved by:

Major Professor
Dr. Claudia Adam

Copyright

©Jayasamudi Abeysinghe Mudiyanselage 2026.

Abstract

Although earthquakes are typically concentrated along plate boundaries, significant seismicity also occurs within the continental interior, in particular along the Central and Eastern United States (CEUS). In this study, we model the stress induced by mantle convection in CEUS. We consider several global and regional tomography models. Seismic velocity anomalies from the tomography models are converted into density anomalies. Then we compute the instantaneous mantle flow induced by these anomalies, as well as the inferred tectonic regimes and maximum shear stress, SH_{max}. The derived tectonic regimes are compared to the surface observations obtained from earthquakes focal mechanisms, to assess if the mantle convection may be responsible for the intraplate seismicity in CEUS. The results show that tomography model and viscosity law strongly affect the modeled tectonic regimes, whereas the conversion factor has only a minor influence. The best overall agreement is obtained with the TX2019slab global model (Lu et al., 2019) with Adam et al. (2021) seismic velocity anomalies to density anomalies conversion factor $R_{\rho/vs}$, and depth-dependent viscosity based on CAM2022 model (Priestley et al., 2024). Most global tomography models recover the compressive regimes observed in the northeastern North American continent, whereas this pattern is generally not reproduced by regional models, suggesting that it may be driven by larger-scale processes. The mantle upwellings beneath BR-RGR (Basin and Range-Rio Grande Rift), region A (Nebraska), region B (Great Lakes, Ontario, Canada), and Bermuda remain across the most tested models, for most of the implemented model parameters, suggesting that these features are real rather than model artifacts. A high-density anomaly between the ETSZ (Eastern Tennessee Seismic Zone) and NMSZ (New Madrid Seismic Zone) is consistently seen in the models and may reflect dense or foundering lithosphere. Overall, these results indicate that large-scale mantle dynamics plays an important role in intraplate seismicity in

the CEUS. Additional regional shallower processes may be required to explain the remaining misfits, such as the extension observed along the ETSZ, which none of the models or other previous models proposed in the literature have been able to reproduce.

Table of Contents

List of Figures vii
List of Tables xvii
Acknowledgements xviii
Chapter 1 - Introduction 1
Chapter 2 - Background study 4
2.1 Seismicity characteristics in the Central and Eastern United States (CEUS) 4
2.1.1 New Madrid Seismic Zone (NMSZ) 6
2.1.2 Eastern Tennessee Seismic Zone (ETSZ) 7
2.1.3 Central Virginia Seismic Zone (CVSZ) 7
2.1.4 South Carolina Seismic Zone (SCSZ) 8
2.1.5 Giles County Seismic Zone (GCSZ) 8
2.2 Studies on causes for the origin of intraplate seismicity 8
2.2.1 Gravitational Potential Energy (GPE) 9
2.2.2 Glacial Isostatic Adjustment (GIA) 9
2.2.3 Anthropogenic activities 10
2.2.4 Pre-existing weakness zones 10
2.2.5 Mantle dynamics 10
2.3 Hypothesis 12
2.4 Objectives 13
2.5 Potential impact 13
Chapter 3 - Methods 14
3.1 Viscosity laws 15
3.2 Tomography models 17
3.2.1 Global tomography models 17
3.2.2 Regional tomography models 18
3.3 Conversion factors 20
3.4 Geodynamic modeling 20
3.5 Tectonic regimes and SH_{max} computation 22
3.6 Surface observation comparison 23

3.7 Quantitative assessment of tectonic regime and SH_{max} orientations correlation 24
Chapter 4 - Results 27
4.1 Tomography models 27
4.1.1 Global tomography models 27
4.1.2 Regional tomography models 43
4.2 Influence of the viscosity 59
4.3 Conversion factors 64
4.3.1 Conversion factors from previous studies 64
4.3.2 Conversion factor including an elastic model 65
Chapter 5 - Discussion 67
5.1 Sensitivity of model parameters 67
5.1.1 Tomography models 67
5.1.2 Viscosity laws 73
5.1.3 Conversion factors 78
5.2 Comparison with former studies 78
Chapter 6 - Conclusion 87
References 89
Appendix 97
Appendix 1 97
Appendix 2 98

List of Figures

Figure 1.1: Seismicity in the Central and Eastern United States (CEUS), extracted from Saxena et al. (2021), including seismic zones: New Madrid Seismic Zone (NMSZ), Eastern Tennessee Seismic Zone (ETSZ), South Carolina Seismic Zone (SCSZ), Giles County Seismic Zone (GCSZ) and Central Virginia Seismic Zone (CVSZ). The earthquakes that occurred over the period December 2011–December 2018 and had Mw > 2.5 are plotted as colored circles. The size and color of a circle represent the event's magnitude and depth. The earthquake catalog is obtained from the United States Geological Survey at https://earthquake.usgs.gov/earthquakes/search/. 3

Figure 2.1: Seismicity in the Central and Eastern United States (CEUS) based on the study by Levandowski et al. (2018) (a), Snee and Zoback (2020) (b), and Heidbach et al. (2018) (c). Circled areas are the Rio Grande Rift and major seismic zones, including New Madrid Seismic Zone (NMSZ), Eastern Tennessee Seismic Zone (ETSZ), South Carolina Seismic Zone (SCSZ), Giles County Seismic Zone (GCSZ) and Central Virginia Seismic Zone (CVSZ). Tectonic regimes are indicated by colors: extension(red), compression(blue) and strike-slip (green). Lines represent the orientation of SHmax. Black dots represent the earthquake locations. The magenta lines mark state boundaries (https://www.census.gov/geographies/mapping-files/time-series/geo/carto-boundary-file.html). These three databases were studied for the comparison of surface observations. . 5

Figure 3.1: Lithosphere Asthenosphere Boundary (LAB) used in this study and derived from CAM2016 (Priestley et al., 2019), (a), WINTERC-G (Fullea et al., 2021), (b) and CAM2022 (Priestley et al., 2024), (c)..... 16

Figure 3.2: Variations of seismic velocity anomaly, dvs, imaged by different global tomography models considered in this study at 200 km depth, a) TX2019slab (Lu et al., 2019); b) SEMUCB-WM1 (French and Romanowicz, 2014); c) SPiRaL (Simmons et al., 2021). The black lines are the 0 and 2500 m isolines (data from Tozer et al., (2019)). 18

Figure 3.3: Variations of seismic velocity anomaly, dvs, imaged by different regional tomography models considered in this study at 200 km depth, a) CSEM_North_America model (Fichtner et al., 2018) ; b) CURSA2021(Zhou et al., 2022); c) DNA13(Porritt et al.,

2014); d) SATONA (Hua et al., 2025). The black lines are the 0 and 2500 m isolines (data from Tozer et al. (2019)). 19
Figure 3.4: Illustration of the model parameters. Depth cross sections at latitude 45ºN across the SEMUCB-WM1 tomography model (French & Romanowicz, 2015) (a), the density anomalies computed by considering Adam et al. (2022) conversion factor (b), and the viscosity ($\eta_6(z)$) (c). Here we use CAM2022 model (Priestley et al., 2024) for the base of the lithosphere. The arrows in panel b represent the convection pattern induced by the density anomalies. 21
Figure 3.5: Illustration of the method used to define tectonic regimes (from Heidbach et al. (2018)). The definition uses SH_{max} (maximum horizontal stress), Sh_{min} (minimum horizontal stress) and S_V (vertical stress). Normal fault regime occurs where the vertical stress is larger than the horizontal stresses (a); strike-slip fault regime occurs where the vertical stress is the intermediate principal stress (b); thrust fault regime occurs where the vertical stress is smaller than the horizontal stresses (c). 23
Figure 3.6: Stress maps showing observed tectonic regimes across the CEUS based on the study by Levandowski et al. (2018) (a) and Snee and Zoback (2020) (b). Lines represent the orientation of SH_{max}. Extension regimes are displayed in red, compression regimes in blue, strike slip in green, while the unknown regimes are displayed in black. Black dots represent the earthquake locations. The magenta lines mark state boundaries (https://www.census.gov/geographies/mapping-files/time-series/geo/carto-boundary-file.html). Levandowski et al. (2018) is used for the comparison between modeled and observed tectonic regimes. 24
Figure 3.7: Illustration of our quantification of the fit between observed tectonic regimes (a) and modeled tectonic regimes (b). Matching cells are assigned a value of 0 (magenta color box), while different cells are assigned a value of 1 (red color box) in the resulting misfit output (c). The black boxes represent the one degree by one degree grid used in our study. 25
Figure 3.8: Illustration of our quantification of the difference (c) between observed SH_{max} orientations (a) and modeled SH_{max} orientations (b). This calculation is performed only when the modeled regimes reproduce the observed ones. The black boxes represent the one degree by one degree grid used in our study. 26

Figure 4.1: Modeled tectonic regimes and mantle flow. (a) Modeled tectonic regimes and SH_{max} directions computed with the SEMUCB-WM1 tomography model (French & Romanowicz, 2014) at 99 km depth. The model uses a depth dependent viscosity based on the CAM2022 lithosphere thickness (Priestley et al., 2024), (viscosity law $\eta_3(z)$, section 3.1), and the conversion factor between seismic velocity anomalies and density anomalies, $R_{\rho/vs}$, developed by Adam et al. (2021). Lines represent the orientation of SH_{max}. Extension regimes are displayed in red, compression regimes in blue and strike slip in green. The gray map represents the topography (data from Tozer et al. (2019)) and black dots the seismicity (data from Levandowski et al. (2018)). Thin black lines mark the state boundaries. The lowermost panels display the instantaneous mantle flow at different latitude, (b) latitude 40ºN, (c) latitude 47ºN and (d) latitude 55ºN. Abbreviations used in the Figure 4.1 are BR-RGR for Basin and Range-Rio Grande Rift, JDF for the Juan de Fuca Plate, MOR for the Mid Oceanic Ridge and MAR for the Mid-Atlantic Ridge. Arrows in the lower panel indicate the instantaneous flow induced by the density anomalies..... 28

Figure 4.2: Modeled tectonic regimes varying with depth for the SEMUCB-WM1 model. The viscosity is depth dependent based on CAM2022 model (viscosity law $\eta_3(z)$, section 3.1) and the $R_{\rho/vs}$ is from Adam et al. (2021). Panels a-k: each panel shows the modeled tectonic regimes (see color scale legend) and the SH_{max} directions at depths reported on top of each panel. Black dots: seismicity from Levandowski et al. (2018). l) Surface observations taken from Levandowski et al. (2018). The black (a-k) and magenta (l) lines mark state boundaries (https://www.census.gov/geographies/mapping-files/time-series/geo/carto-boundary-file.html). 30

Figure 4.3: Variation of tectonic regimes with depth for the SEMUCB-WM1 model across the Central and Eastern United States (CEUS). The viscosity is depth dependent based on CAM2022 model (viscosity law $\eta_3(z)$, section 3.1) and the $R_{\rho/vs}$ is from Adam et al. (2021). Circled areas are the Basin and Range - Rio Grande Rift (BR-RGR) and the major seismic zones, including New Madrid Seismic Zone (NMSZ), Eastern Tennessee Seismic Zone (ETSZ), South Carolina Seismic Zone (SCSZ), Giles County Seismic Zone (GCSZ) and Central Virginia Seismic Zone (CVSZ). Panels a-k: each panel shows the modeled tectonic regimes (see color scale legend) and the SH_{max} directions at depths reported on top of each panel. Black dots: seismicity from Levandowski et al. (2018). l) Surface observations taken

from Levandowski et al. (2018). The black (a-k) and magenta (l) lines mark state boundaries (https://www.census.gov/geographies/mapping-files/time-series/geo/carto-boundary-file.html). 32
Figure 4.4: Same as Figure 4.1, for the SPiRaL tomography model (Simmons et al., 2021). Regions A, B, anc C are the upwelling zones indentified from the corresponding depth cross sections of the SEMUCB-WM1 tomography model (Figure 4.1). 34
Figure 4.5: Same as Figure 4.2, for SPiRaL tomography model (Simmons et al., 2021). 35
Figure 4.6: Same as Figure 4.3, for the SPiRaL tomography model (Simmons et al., 2021). 36
Figure 4.7: Same as Figure 4.1, for the TX2019slab tomography model (Lu et al., 2019). Regions A, B, anc C are the upwelling zones indentified from the corresponding depth cross setions of the SEMUCB-WM1 tomography model (Figure 4.1). 38
Figure 4.8: Same as Figure 4.2, for the TX2019slab tomography model (Lu et al., 2019). 39
Figure 4.9: Same as Figure 4.3, for the TX2019slab tomography model (Lu et al., 2019). 41
Figure 4.10: RMS (Root Mean Square) between the observed tectonic regimes, and the regimes modeled from the SEMUCB-WM1(French & Romanowicz, 2014), SPiRaL (Simmons et al., 2021) and TX2019slab (Lu et al., 2019) tomography models (see section 3.6 for the RMS computation description). The viscosity is depth dependent based on CAM2022 model (viscosity law $\eta_3(z)$, section 3.1) and the conversion factor between seismic velocity anomalies and density anomalies, $R_{\rho/vs}$ from Adam et al. (2021). Best fits are associated with an RMS~0.7 (yellow regions). 42
Figure 4.11: (a) Modeled tectonic regimes and SH_{max} directions computed with the DNA13 regional tomography model (Porritt et al., 2014) at 99 km depth. The model uses a depth dependent viscosity based on the CAM2022 lithosphere thickness (Priestley et al., 2024), (viscosity law $\eta_3(z)$, section 3.1), and the conversion factor between seismic velocity anomalies and density anomalies, $R_{\rho/vs}$, developed by Adam et al. (2021). Lines represent the direction of SH_{max}. Extension regimes are displayed in red, compression regimes in blue and strike slip in green. The gray map represents the topography (data from Tozer et al. (2019)) and black dots the seismicity (data from Levandowski et al. (2018)). Thin black lines mark the state boundaries. The lowermost panels display the instantaneous mantle flow at different latitude, (b) latitude 40ºN, (c) latitude 47ºN and (d) latitude 35ºN. Abbreviations used in the Figure 4.11b, JDF for the Juan de Fuca Plate and MOR for Mid

Ocean Ridge. Arrows in the lower panel indicate the instantaneous flow induced by the density anomalies. Regions A and B are the upwelling zones indentified from the corresponding depth cross setions of the SEMUCB-WM1 global tomography model (Figure 4.1). The magenta box outlines the area covered by the regional tomography model data.. 44
Figure 4.12: Variation of tectonic regimes with depth for the DNA13 tomography model (Porritt et al., 2014) across the Central and Eastern United States (CEUS). The viscosity is depth dependent based on CAM2022 model (viscosity law $\eta_3(z)$, section 3.1) and the $R_{\rho/vs}$ is from Adam et al. (2021). Circled areas are the Basin and Range - Rio Grande Rift (BR-RGR) and the major seismic zones, including New Madrid Seismic Zone (NMSZ), Eastern Tennessee Seismic Zone (ETSZ), South Carolina Seismic Zone (SCSZ), Giles County Seismic Zone (GCSZ) and Central Virginia Seismic Zone (CVSZ). Panels a-k: each panel shows the modeled tectonic regimes (see color scale legend) and the SH_{max} directions at depths reported on top of each panel. Black dots: seismicity from Levandowski et al. (2018). l) Surface observations taken from Levandowski et al. (2018). The black (a-k) and magenta (l) lines mark state boundaries (https://www.census.gov/geographies/mapping-files/time-series/geo/carto-boundary-file.html). 46
Figure 4.13: Same as Figure 4.11, for the CURSA2021 tomography model (Zhou et al., 2022). Regions A and B are the upwelling zones indentified from the corresponding depth crosssections of the SEMUCB-WM1 global tomography model (Figure 4.1). 48
Figure 4.14: Same as Figure 4.12, for the CURSA2021 tomography model (Zhou et al., 2022). 50
Figure 4.15: Same as Figure 4.11, for the CSEM_North_America model (Fichtner et al., 2018). Regions A and B are the upwelling zones indentified from the corresponding depth crosssections of the SEMUCB-WM1 global tomography model (Figure 4.1). 51
Figure 4.16: Same as Figure 4.3, for the CSEM_North_America model (Fichtner et al., 2018). 52
Figure 4.17: Same as Figure 4.1, for the SATONA tomography model (Hua et al., 2025). Regions A, B, anc C are the upwelling zones indentified from the corresponding depth crosssections of the SEMUCB-WM1 global tomography model (Figure 4.1). 53
Figure 4.18: Same as Figure 4.2, for the SATONA tomography model (Hua et al., 2025). 55
Figure 4.19: RMS (Root Mean Square) between the observed tectonic regimes, and the regimes modeled from the DNA13 (Porritt et al., 2014), CURSA2021 (Zhou et al., 2022), CSEM_North_America (Fichtner et al., 2018) and SATONA (Hua et al., 2025) regional

tomography models (see section 3.6 for the RMS computation description). The viscosity is depth dependent based on CAM2022 model (viscosity law $\eta_3(z)$, section 3.1) and the conversion factor between seismic velocity anomalies and density anomalies, $R_{\rho/vs}$ from Adam et al. (2021). Best fits are associated with an RMS ~ 0.85 (cyan regions). 56

Figure 4.20: Modeled tectonic regimes with different viscosity laws discussed in section 3.1 using SEMUCB-WM1 tomography model (French & Romanowicz, 2014), (a) constant viscosity(η_1), (b) depth dependent viscosity with 100 km thick lithosphere($\eta_2(Z)$), (c) depth dependent viscosity with LAB CAM2022($\eta_3(Z)$), (d) temperature dependent viscosity($\eta_4(T)$), (e) depth and temperature dependent viscosity ($\eta_5(T,Z)$), (f) depth dependent viscosity with WPB ($\eta_6(Z)$) and (g) temperature dependent viscosity with WPB ($\eta_7(T)$) at 77 km depth. The conversion factor between seismic velocity anomalies and density anomalies, $R_{\rho/vs}$ is from Adam et al. (2021). h) Surface observations taken from Levandowski et al. (2018). The gray map represents the topography (data from Tozer et al. (2019)) and black dots the seismicity (data from Levandowski et al. (2018)). The black (a-g) and magenta (h) lines mark state boundaries (https://www.census.gov/geographies/mapping-files/time-series/geo/carto-boundary-file.html). Regions A and B are the extensional zones associated with upwellings seen in the depth cross-sections of the SEMUCB-WM1 tomography model (Figure 4.1). The green and blue boxes indicate the modeled tectonic regimes for models with (f, g) and without WPB (c,d) for $\eta_3(Z)$ and $\eta_4(T)$ respectively..... 60

Figure 4.21: Same as Figure 4.21, i.e., modeled tectonic regimes but at 99 km depth. The red star indicates the location of Bermuda..... 62

Figure 4.22: RMS (Root Mean Square) between the observed tectonic regimes and the modeled tectonic regimes using the viscosity laws discussed in section 3.1 using SEMUCB-WM1 tomography model (French & Romanowicz, 2014). The conversion factor between seismic velocity anomalies and density anomalies, $R_{\rho/vs}$ from Adam et al. (2021). Best fits are associated with an RMS ~ 0.75 (yellow regions). 63

Figure 4.23: Variation of modeled tectonic regimes using different conversion factors between seismic velocity anomalies and density anomalies, $R_{\rho/vs,}$ (a) Adam et al. (2021), (b) Karato (2008), (c) Simmons et al. (2009), (d) Steinberger and Calderwood (2006) and (e) Lee et al.

(2011) with SEMUCB-WM1 tomography model (French & Romanowicz, 2014) at 99 km depth. The viscosity is depth dependent based on CAM2022 model (viscosity law $\eta_3(Z)$, section 3.1). The gray map represents the topography (data from Tozer et al. (2019)) and black dots the seismicity (data from Levandowski et al. (2018)). f) Surface observations taken from Levandowski et al. (2018). The black(a-e) and magenta(f) lines mark state boundaries (https://www.census.gov/geographies/mapping-files/time-series/geo/carto-boundary-file.html). Regions A and B correspond to the extensional zones associated with upwellings seen in the depth crosssections of the SEMUCB-WM1 tomography model (Figure 4.1). 64

Figure 4.24: Modeled tectonic regimes with a 3D anelastic model (a) and with a 1D anelastic model (i.e., $\boldsymbol{R\rho/v}$ from Adam et al. (2021)) (b). The 3D anelastic component is from Debayle et al. (2020), and we use the SEMUCB-WM1 tomography model and constant viscosity (viscosity law η_1, section 3.1) at 99 km depth. 66

Figure 5.1: Modeled tectonic regimes at depth 99 km using (a) the SEMUCB-WM1 tomography model (French & Romanowicz, 2015), (b) the SPiRaL tomography model (Simmons et al., 2021), and (c) TX2019slab tomography model (Lu et al., 2019) (c), as well as the $R_{\rho/vs}$ from Adam et al. (2021) and the depth dependent viscosity based on CAM2022 (viscosity law $\eta_3(Z)$, section 3.1). Corresponding depth cross-sections of the density anomalies and the induced mantle flow are shown at latitude 33ºN in panels d-f and latitude 36ºN in panels g-i, respectively. 71

Figure 5.2: Modeled tectonic regimes at 99 km depth modeled from a) the DNA13 tomography model (Porritt et al., 2014), b) the CSEM_North_America tomography model (Fichtner et al., 2018), (c) the CURSA2021 tomography model (Zhou et al., 2022) and d) the SATONA tomography model (Hua et al., 2025), using the $R_{\rho/vs}$ from Adam et al. (2021) and a depth dependent viscosity based on CAM2022 (viscosity law $\eta_3(z)$, section 3.1). Corresponding depth cross-sections are shown at latitude 33ºN in panels e-h and latitude 36ºN in panels i-l, respectively. 72

Figure 5.3: Modeled tectonic regimes at 99 km depth with different viscosity laws using SEMUCB-WM1 tomography model (French & Romanowicz, 2014). (a) constant viscosity(η_1), (b) depth dependent viscosity with 100 km thick lithosphere ($\eta_2(Z)$), (c) depth dependent viscosity with LAB CAM2022 ($\eta_3(Z)$), (g) temperature dependent viscosity

(η_4(T)), (h) depth and temperature dependent viscosity (η_5(T,Z)), (i) depth dependent viscosity with WPB (η_6(Z)) and (j) temperature dependent viscosity with WPB (η_7(T)). The conversion factor between seismic velocity anomalies and density anomalies, $R_{\rho/vs}$ is from Adam et al. (2021). Corresponding depth cross-sections are shown at latitude 36ºN in panels d-f and k-n. 75
Figure 5.4: RMS (Root Mean Square) between the observed tectonic regimes and the modeled tectonic regimes using the viscosity laws discussed in section 3.1, the SEMUCB-WM1 tomography model (French & Romanowicz, 2014) and the conversion factor between seismic velocity anomalies and density anomalies, $R_{\rho/vs}$ from Adam et al. (2021). The viscosity laws are as follows: constant viscosity (η_1), depth dependent viscosity with 100 km thick lithosphere (η_2(Z)), depth dependent viscosity with LAB CAM2022 (η_3(Z)), temperature dependent viscosity (η_4(T)), depth and temperature dependent viscosity (η_5(T,Z)), depth dependent viscosity with WPB (η_6(Z)) and temperature dependent viscosity with WPB (η_7(T)). Best fits are shown by red stars. 77
Figure 5.5: a) S wave imaging of the mantle structure showing two fast anomalies (A and C) and a slow anomaly (B); b) Schematic interpretation of mantle structure beneath the Rio Grande rift and surrounding regions, extracted from Gao et al. (2004). The stippled pattern in shallow mantle shows the lithosphere. Arrows represent the mantle flow direction, and wavy lines represent mantle enriched volatiles. 81
Figure 5.6: a) Shear wave velocity maps at 100 km depth and location of the CC' profile (white line) along which the LA RISTRA experiment has been conducted; b) C–C′ cross section lies on southern part of the LA RISTRA passive experiment. They identify an upwelling beneath the Jemez Lineament (JL), which they term the Jemez Upwelling, modified from Sosa et al. (2014). 82

Appendix Figure 1 : Modeled tectonic regimes at depth 99 km using the TX2019slab tomography model (Lu et al., 2019) with depth dependent viscosity laws, $\eta_2(Z)$, (a), $\eta_3(Z)$, (b) $\eta_6(Z)$, (c) (section 3.1) as well as the $R_{\rho/vs}$ from Adam et al. (2021). Corresponding depth cross-sections of the density anomalies and the induced mantle flow are shown at latitude 45ºN in panels d-f and latitude 40ºN in panels g-i, respectively. 98
Appendix Figure 2 : Modeled tectonic regimes at depth 99 km using the SPiRaL tomography model (Simmons et al., 2021), with temperature and both depth and temperature dependent viscosity laws, $\eta_4(T)$, (a), $\eta_5(T,Z)$, (b) and $\eta_7(T)$, (c) (section 3.1) as well as the $R_{\rho/vs}$ from Adam et al. (2021). Corresponding depth cross-sections of the density anomalies and the induced mantle flow are shown at latitude 45ºN in panels d-f and latitude 40ºN in panels g-i, respectively. 99
Appendix Figure 3 : Modeled tectonic regimes at depth 99 km using the SEMUCB-WM1 tomography model (French & Romanowicz, 2015), with temperature and both depth and temperature dependent viscosity laws, $\eta_4(T)$, (a), $\eta_5(T,Z)$, (b) and $\eta_7(T)$, (c) (section 3.1) as well as the $R_{\rho/vs}$ from Adam et al. (2021). Corresponding depth cross-sections of the density anomalies and the induced mantle flow are shown at latitude 45ºN in panels d-f and latitude 40ºN in panels g-i, respectively. 100
Appendix Figure 4 : Modeled tectonic regimes at depth 99 km using the SEMUCB-WM1 tomography model (French & Romanowicz, 2014), (a), SPiRaL tomography model (Simmons et al., 2021), (b), TX2019slab tomography model (Lu et al., 2019), (c) DNA13 (Porritt et al., 2014), (g), CURSA2021 (Zhou et al., 2022), (h), CSEM_North_America (Fichtner et al., 2018), (i) and SATONA (Hua et al., 2025), (j). The models use the same depth dependent viscosity (viscosity law $\eta_3(Z)$, section 3.1), based on the CAM2022 lithosphere thickness (Priestley et al., 2024). Corresponding depth cross-sections of the density anomalies and the induced mantle flow are shown at latitude 36ºN in panels d-f and g-j. Triangles mark the zone between NMSZ and ETSZ..... 101
Appendix Figure 5 : Modeled tectonic regimes at depths greater than 200 km for SATONA regional tomography model (Hua et al., 2025). The model use depth dependent viscosity (viscosity law $\eta_3(Z)$, section 3.1), based on the CAM2022 lithosphere thickness (Priestley et al., 2024). Yellow dashed line represents the dripping high Vs body region found by Hua et al. (2025). 102

Appendix Figure 6 : Modeled tectonic regimes at depths greater than 200 km for CURSA2021 regional tomography model (Zhou et al., 2022). The model use depth dependent viscosity (viscosity law $\eta_3(Z)$, section 3.1), based on the CAM2022 lithosphere thickness (Priestley et al., 2024). Yellow dashed line represents the dripping high Vs body region found by Hua et al. (2025). 103
Appendix Figure 7 : Modeled tectonic regimes at depths greater than 200 km for CSEM_North_America regional tomography model (Fichtner et al., 2018). The model use depth dependent viscosity (viscosity law $\eta_3(Z)$, section 3.1), based on the CAM2022 lithosphere thickness (Priestley et al., 2024). Yellow dashed line represents the dripping high Vs body region found by Hua et al. (2025). 104
Appendix Figure 8 : Modeled tectonic regimes at 99 km depth with different viscosity laws using SPiRaL tomography model (Simmons et al., 2021). (a) constant viscosity(η_1), (b) depth dependent viscosity with 100 km thick lithosphere ($\eta_2(Z)$), (c) depth dependent viscosity with LAB CAM2022 ($\eta_3(Z)$), (g) temperature dependent viscosity ($\eta_4(T)$), (h) depth and temperature dependent viscosity ($\eta_5(T,Z)$), (i) depth dependent viscosity with WPB ($\eta_6(Z)$) and (j) temperature dependent viscosity with WPB ($\eta_7(T)$). The conversion factor between seismic velocity anomalies and density anomalies, $R_{\rho/vs}$ is from Adam et al. (2021). Corresponding depth cross-sections are shown at latitude 36ºN in panels d-f and k-n. 105
Appendix Figure 9 : Variation of tectonic regimes with depth for the SPiRaL tomography model (Simmons et al., 2021) across the Central and Eastern United States (CEUS). The viscosity is depth dependent based on CAM2022 model with WPB(viscosity law $\eta_6(Z)$, section 3.1) and the $R_{\rho/vs}$ is from Adam et al. (2021). Circled areas are the Basin and Range - Rio Grande Rift (BR-RGR) and the major seismic zones, including New Madrid Seismic Zone (NMSZ), Eastern Tennessee Seismic Zone (ETSZ), South Carolina Seismic Zone (SCSZ), Giles County Seismic Zone (GCSZ) and Central Virginia Seismic Zone (CVSZ). Panels a-k: each panel shows the modeled tectonic regimes (see color scale legend) and the SH_{max} directions at depths reported on top of each panel. Black dots: seismicity from Levandowski et al. (2018). l) Surface observations taken from Levandowski et al. (2018). The black (a-k) and magenta (l) lines mark state boundaries (https://www.census.gov/geographies/mapping-files/time-series/geo/carto-boundary-file.html). 106

List of Tables

Table 4.1 : Modeled regimes over CEUS and other regions included in this study based on the studied global and regional tomography models using depth dependent viscosity based on CAM2022 model (viscosity law $\eta_3(z)$, section 3.1) and $R_{\rho/vs}$ from Adam et al. (2021). C, E and SS denote compression, extension and strike slip regimes respectively. 58

Table 5.1 : RMS values for viscosity models for various depths (33-473 km). Notation of the viscosity laws are described in section 3.1 76

Acknowledgements

This thesis would not have been possible without the support and guidance of many individuals and institutions, to whom I wish to express my sincere gratitude.

First and foremost, I extend my deepest thanks to my supervisor, Dr. Claudia Adam. Her constant encouragement, thoughtful feedback, and unwavering guidance have been invaluable throughout my master's journey, shaping both my academic work and my personal growth in profound ways.

I am also sincerely grateful to my committee members, Dr. Michael Gurnis and Dr. Brice Lacroix, for their insightful comments and constructive contributions that meaningfully strengthened this project.

My appreciation goes to Dr. Matthew Brueseke, Head of the Department, and to all the faculty, staff, and my friends in the Department of Geology at Kansas State University. Their support and kindness helped and encouraged me to complete my project successfully.

I gratefully acknowledge the financial support provided by the National Science Foundation and the Department of Geology at Kansas State University, which made this research possible.

Finally, my heartfelt thanks go to my family and the wonderful Manhattan community. Their unconditional love, constant encouragement, and steady presence carried me through every stage of this journey.

Chapter 1 - Introduction

Earthquakes that occur away from plate boundaries form the intraplate seismicity. Intraplate seismicity often occurs in the Central and Eastern United States (CEUS) and is mostly concentrated along several seismic zones such as New Madrid Seismic Zone (NMSZ) and Eastern Tennessee Seismic Zone (ETSZ) (Figure 1) (Saxena et al., 2021). The origin of the CEUS intraplate seismicity is still debated and can vary from one region to another. Intraplate earthquakes can have significant impacts on public safety, infrastructure damage and economic stability. Understanding the causes of these earthquakes is important for improving earthquake risk predictions and for understanding the Earth's dynamic processes.

There are several hypotheses for the origin of intraplate seismicity in CEUS. A few of them are Glacial Isostatic Adjustment (GIA) (Grollimund and Zoback, 2001; Mazzotti et al., 2005; Muir-Wood, 2000), Gravitational Potential Energy (GPE) (Ghosh et al., 2019; Saxena et al., 2021), far field stresses (Humphreys and Coblentz, 2007), fault interaction where faults can be inactive after ruptures while large earthquakes shift between faults nearby, due to tectonic loading and stress changes (Liu and Stein, 2016), pre-existing weakness zones (Saxena et al., 2021; Zhan et al., 2016), stress concentration in the crust due to lateral heterogeneities in the lithosphere (Li et al., 2007) or mantle dynamics (Forte et al., 2007; Saxena et al., 2021). While each of these ideas offers valuable insights, relationship between mantle dynamics and intraplate seismicity remains relatively underexplored. Therefore, in this study we explore the hypothesis that mantle dynamics may contribute to the origin of intraplate seismicity in some regions of the CEUS.

To test this hypothesis, we use regional and global tomography models to obtain seismic velocity anomalies. Although, several studies have used tomography models to study the causes of intraplate seismicity, their conclusion depend on the specific tomography model. Different tomography models use different input data and inversion methods to obtain the result . Therefore, different tomography models provide different models of the Earth's structure. If a feature appears in only one or a few tomography models, it may be unreliable. However, if it shows in multiple models, it is more favorable to be a real feature of the Earth's structure. Therefore, considering several tomography models is important for identifying errors in the modeling process. In this study, we considered several global and regional tomography models.

Seismic velocity anomalies obtained from the tomography models are converted into density anomalies using different conversion factors. From the resulting density anomalies, we compute the instantaneous mantle flow, the induced tectonic regimes and maximum shear stresses, SH_{max}. These derived stresses are compared to the tectonic regimes and SH_{max} derived from focal mechanisms (Snee and Zoback, 2020), to see if mantle convection may be responsible for some of the intraplate seismicity. Additionally, we conduct a sensitivity test of the model parameters, namely the input tomography models, the velocity to density conversion factor and the viscosity laws. This allows us to better understand the influence of mantle dynamics on intraplate seismicity in the CEUS.

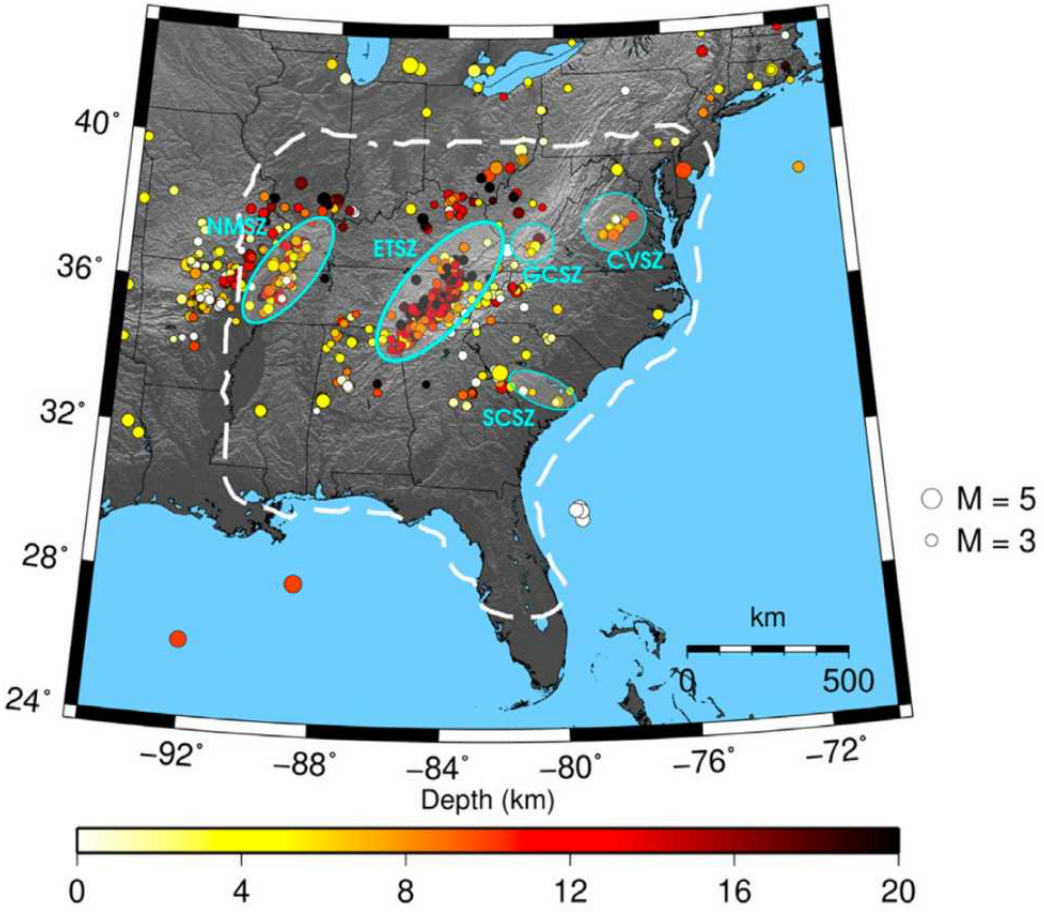

Figure 1.1: Seismicity in the Central and Eastern United States (CEUS), extracted from Saxena et al. (2021), including seismic zones: New Madrid Seismic Zone (NMSZ), Eastern Tennessee Seismic Zone (ETSZ), South Carolina Seismic Zone (SCSZ), Giles County Seismic Zone (GCSZ) and Central Virginia Seismic Zone (CVSZ). The earthquakes that occurred over the period December 2011–December 2018 and had Mw > 2.5 are plotted as colored circles. The size and color of a circle represent the event's magnitude and depth. The earthquake catalog is obtained from the United States Geological Survey at https://earthquake.usgs.gov/earthquakes/search/.

Chapter 2 - Background study

As discussed in the introduction, the origin of the CEUS intraplate seismicity is still debated, and it can vary from one region to another. In this chapter, we describe the main characteristics of the CEUS intraplate seismicity and summarize the main hypotheses proposed in the literature to account for it.

2.1 Seismicity characteristics in the Central and Eastern United States (CEUS)

Seismicity in CEUS is very complex and therefore different studies have been conducted on intraplate seismicity concentrating along the seismic zones such as New Madrid Seismic Zone, Eastern Tennessee Seismic Zone, South Carolina Seismic Zone, Central Virginia Seismic Zone, and Giles County Seismic Zone (Figure 2.1). Most of these zones are associated with ancient fault systems that may have been reactivated under present day stress conditions. Although the strain rate is relatively low when compared with regions near plate boundaries (Saxena et al., 2021), CEUS has a significant historical and present-day seismicity, stressing the need to understand the related subsurface geodynamic processes (Becker et al., 2015; Biryol et al., 2016; Ghosh et al., 2019; Saxena et al., 2021). Observations based on focal mechanisms, borehole breakouts, drilling induced fractures, overcoring and hydraulic fractures (Heidbach et al., 2018), reveal that the eastern US is mainly under compression, the western part, which encompasses the Rio Grande Rift is characterized by an extensional regime, while the central part of our study area is a mix of strike slip and extension regimes (Figure 2.1). Note that the regimes along some of the seismic zones vary according to the authors. This is discussed in more details in the following sub-sections. Such a set-up and diversity of tectonic regimes make the CEUS an ideal region to study the underlying mechanism of intraplate seismicity and to assess where and how earth processes influence the seismicity.

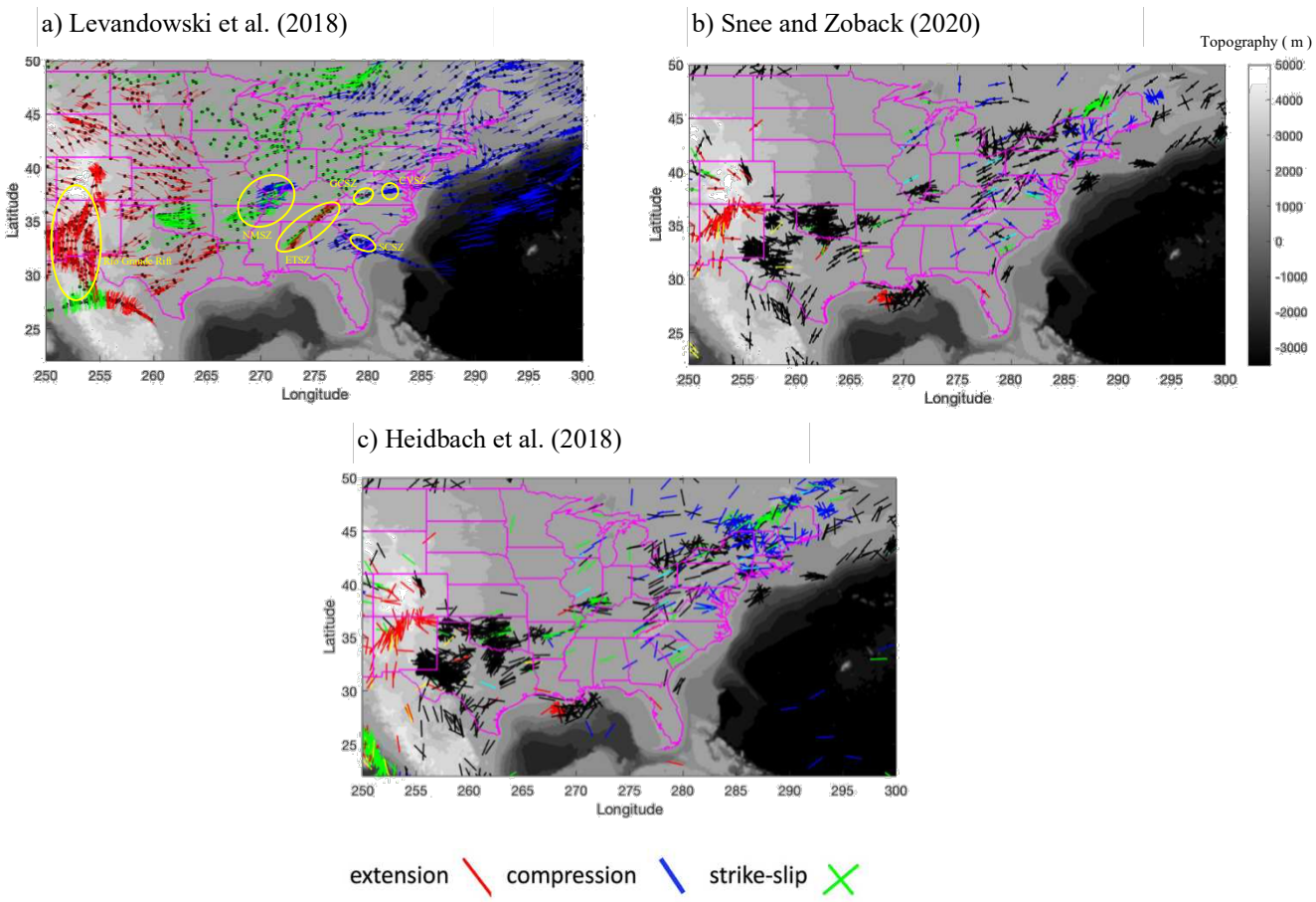

Figure 2.1: Seismicity in the Central and Eastern United States (CEUS) based on the study by Levandowski et al. (2018) (a), Snee and Zoback (2020) (b), and Heidbach et al. (2018) (c). Circled areas are the Rio Grande Rift and major seismic zones, including New Madrid Seismic Zone (NMSZ), Eastern Tennessee Seismic Zone (ETSZ), South Carolina Seismic Zone (SCSZ), Giles County Seismic Zone (GCSZ) and Central Virginia Seismic Zone (CVSZ). Tectonic regimes are indicated by colors: extension(red), compression(blue) and strike-slip (green). Lines represent the orientation of SHmax. Black dots represent the earthquake locations. The magenta lines mark state boundaries (https://www.census.gov/geographies/mapping-files/time-series/geo/carto-boundary-file.html). These three databases were studied for the comparison of surface observations.

2.1.1 New Madrid Seismic Zone (NMSZ)

New Madrid seismic zone is one of the most seismically active regions of intraplate in CEUS, with magnitude rarely exceeding M3 earthquakes (Craig et al., 2017). Several Researchers have studied the cause for this seismicity on the region. Chen et al. (2014) use a 3-D P-wave velocity model of the crust and upper mantle down to 400 km depth to explore structural heterogeneity and its influences on the generation of intraplate earthquakes in the NMSZ. They observe that the large crustal earthquakes in the NMSZ are generally located close to the boundary between the low and high velocity anomalies zone in the lower crust and upper mantle, where the lithospheric strength is weak. Additionally, they suggest that tectonic stress may concentrate there and be transferred to the upper crust, leading to the large intraplate earthquakes. Levandowski et al. (2016) analyze seismic velocity, gravity, and topography to develop a 3-D crustal and upper mantle density model, revealing a dense lower crust beneath the NMSZ. They interpret the gravity-driven stress (due to density variations) and regional tectonic stress (far-field stress) that comes from the movement of tectonic plates and mantle flow interfere constructively make NMSZ with the highest deviatoric stress in the region. Snee and Zoback (2020) present a quantitative study of relative principal stress magnitudes across North America. They propose the NMSZ experiences significantly more compression than in the surrounding regions and suggest localized stress sources are related to ongoing seismicity. Levandowski et al. (2018) suggest, stresses in NMSZ are consistent over a large area but distinct from adjacent areas with a mix of strike slip and compression regimes. They report difference in fault friction and pore pressure cannot fully explain by these stress differences.

2.1.2 Eastern Tennessee Seismic Zone (ETSZ)

The Eastern Tennessee seismic zone is the second most seismically active region in the CEUS (Gallen and Thigpen, 2018). Researchers model the history of landscape evolution above the ETSZ. They interpret, the weak rock zone located above the seismic zone at ETSZ which has exposed for erosion adequate to reactivate pre-existing faults and regional stress field (Gallen and Thigpen, 2018). Powel and Thomas , 2016 propose, earthquake activity in ETZS is due to a large-scale shear zone which formed during the Grenville orogeny and assembly of supercontinent Rodinia. Snee and Zoback (2020) find ETSZ has strike-slip regimes in their database, while Levandowski et al. (2018) report extension regimes in that same region, distinct from adjacent regions.

2.1.3 Central Virginia Seismic Zone (CVSZ)

The Central Virginia seismic zone is an intraplate seismic region in the eastern United States. A seismic reflection study by Coruh et al. (1988) present a correlation between earthquake hypocenters and subsurface structural features imaged in the crust. They suggest seismic activity within the CVSZ may be related to the reactivation of pre-existing thrust faults forming the roof of the antiformal structure and associated faults. The 2011 5.7 Mw Mineral, Virginia mainshock represents the largest earthquake that occurred in the CVSZ (Tuttle et al., 2021). Tuttle et al. (2021) analyze more than 40 earthquakes and induce liquefaction features associated with this event and identify two generations of liquefaction. Their findings emphasize the need for additional surveys and dating to better constrain the seismic hazard potential in CVSZ.

2.1.4 South Carolina Seismic Zone (SCSZ)

The South Carolina Seismic Zone is associated with a rift basin formed during the Mesozoic rifting along with the breakup of Pangea(Shah et al., 2023). Using high-resolution aeromagnetic data, borehole sample data and reprocessed seismic reflection subsurface structures, Shah et al. (2023) identify Paleozoic and Mesozoic structures. They suggest failed rift basin features, such as favorably oriented faults, a sub-basin and potentially weakened lithosphere might contribute to intraplate seismicity in SCSZ.

2.1.5 Giles County Seismic Zone (GCSZ)

The Giles County seismic zone is located along the New River Valley in Giles County. Murphy et al. (2019) work on intraplate seismicity and geomorphology in the Southeastern United States. They use CitcomS to model stresses from input density, temperature and viscosity. They demonstrate local gravitational body forces play a key role in controlling the intraplate stress field in the Southeastern United States. Their models predict normal regimes in the surrounding area of GCSZ.

2.2 Studies on causes for the origin of intraplate seismicity

There are several hypotheses for the origin of intraplate seismicity in CEUS. Some of them are Glacial Isostatic Adjustment (GIA) (Grollimund and Zoback, 2001; Mazzotti et al., 2005; Muir-Wood, 2000), Gravitational Potential Energy (GPE) (Ghosh et al., 2019; Saxena et al., 2021), far field stresses (Humphreys and Coblentz, 2007), fault interaction where faults can be inactive after ruptures while large earthquakes shift between faults nearby, due to tectonic loading and stress changes (Liu and Stein, 2016), pre-existing weakness zones (Saxena et al., 2021; Zhan et al., 2016), stress concentration in the crust due to lateral heterogeneities in the lithosphere (Li et al.,

2007) or mantle dynamics (Forte et al., 2007; Saxena et al., 2021). We discuss these main hypotheses below.

2.2.1 Gravitational Potential Energy (GPE)

The stresses induced by variations in topography, and/or by variations of the density and thickness of the crust and/or lithosphere constitute the GPE (Pascal and Cloetingh, 2009, Saxena et al., 2021). Ghosh et al. (2019) find that GPE alone cannot account for the seismicity observed in CEUS but coupling of GPE and large-scale mantle flow can generate earthquakes.

2.2.2 Glacial Isostatic Adjustment (GIA)

GIA studies examine how the Earth's crust slowly rebound or adjust over time after melting of ice sheets. Wu and Johnston (2000) study North American plate by addressing intraplate deformation caused by GIA. They develop a model incorporating sphericity and self-gravitation, showing that post glacial unloading can trigger earthquakes in Charlevoix, in Michigan and Wabash Valley in between Illinois and Indiana. However, they state that rebound stress is insufficient to cause M8 earthquakes near NMSZ. In contrast, Ghosh et al. (2019) suggest that GIA alone does not account for the stresses associated with intraplate earthquakes but in combination with variation in topography and crustal thickness, and coupling with large-scale mantle flow, it contributes to the occurrence of earthquakes.

2.2.3 Anthropogenic activities

Anthropogenic activities are human activities which cause changes in the nature. Activities such as gas injection (Gan and Frohlich, 2013) and industrial activities including hydraulic fracturing and underground mining (Li et al., 2020) can change the stress field and induce earthquakes.

2.2.4 Pre-existing weakness zones

Pre-existing weak zones in the interior of continents, remains of ancient rifting and mountain provide favorable faults that can reactivate due to changes in stresses. Numerical models using upper mantle heterogeneities from P wave tomography show that mantle flow creates stresses on ancient faults that can trigger earthquakes in areas like CEUS (Saxena et al., 2021).

2.2.5 Mantle dynamics

Mantle convection may play an important role in shaping the Earth's surface topography (e.g., Gurnis et al., 2000; Forte et al., 2007; Adam et al., 2013; Saxena et al., 2021). To study the relationship between intraplate seismicity and mantle dynamics, one approach consists in using tomography models. For example, Biryol et al. (2016) present a new tomography model of the upper mantle beneath the Southeastern United States. Their model shows a fast seismic velocity anomaly interpreted as sinking of lithosphere which could explain the intraplate seismicity observed over the South-east US. Chen et al. (2014) design a 3D P-wave velocity model and find a negative velocity anomaly beneath the NMSZ. They interpret it as a weak zone, which may facilitate the transfer of stresses into the crust. This could account for the observed seismicity.

Some studies use seismic tomography to model the instantaneous mantle flow. Forte et al. (2007) use a Newtonian viscous flow model incorporating internal buoyancy forces derived from seismic

tomography. They conclude that the sinking of the Farallon slab into the mantle creates a mantle flow beneath the NMSZ which may account for the major earthquakes in this region. Ghosh et al. (2019) show that mantle flow alone cannot account for the observed seismicity, but the combined effects of large-scale mantle flow, GPE and GIA can. Saxena et al. (2021) also model the 3D mantle flow to investigate the role of upper mantle heterogeneities. They show that mantle flow and density variations can change the stresses in the upper mantle, which can trigger earthquakes.

Ghosh et al. (2019) and Saxena et al. (2021) agree that seismicity in CEUS depends on GPE and mantle flow. However, according to Ghosh et al. (2019) the stresses induced by the mantle flow are too small to induce earthquakes, while for Saxena et al. (2021) the mantle flow can reactivate faults. Moreover, their conclusion on the specific mechanism differs in scale of processes (large scale vs. local scale). One of the main reasons is that they use different viscosity laws and input tomography models. Saxena et al. (2021) use Coulomb failure criterion and focus on smaller scale (15 km) upper mantle variations using Biryol et al. (2016) tomography model. In contrast, Ghosh et al. (2019) do not use Coulomb failure criterion and examine large scale (105 km) variations with viscosity models based on lithospheric structure.

Other studies focus mainly on the role of slabs, at a global scale (Stadler et al., 2010), or eastern North America (Hightower et al., 2024). For example, Hightower et al. (2024) focus on eastern north America, and they incorporate recent global tomography data that contains the locations of subducting slabs and the negative buoyancy of the Farallon slab to investigate how it affects the stress field. The models assess how intraplate stress changes due to the presence of weak zones or the absence of the Farallon slab . They show that the sinking Farallon slab induces seismicity in

eastern North America by the change of stresses that reactivates the faults. At a larger scale, Stadler et al. (2010) study the role of slab dynamics in mantle flow and plate tectonics through high resolution modeling of slab descent coupling with lithosphere. Slab strength and viscosity significantly impact the lithospheric mantle structure and dynamics (Stadler et al., 2010). They conclude that back arc extension and slab roll back happen as a result of sinking tectonic plates in the upper mantle.

Some of the studies discussed in this section use a similar approach consisting in using seismic tomography to model the instantaneous mantle flow (e.g., Ghosh et al., 2019, Saxena et al., 2021, Forte et al., 2007). However, they often reach different conclusions, as previously discussed. One of the main reasons is that different studies generally use different tomography models as an input. In this study, we consider several global and regional tomography models and then compute the instantaneous mantle flow, induced tectonic regimes and maximum horizontal stress (SHmax). We compare the derived tectonic regimes to the surface observations obtained mainly from the focal mechanisms to assess whether the mantle convection plays a role in the intraplate seismicity in CEUS.

2.3 Hypothesis

Mantle dynamics may significantly influence intraplate seismicity in some regions of the CEUS. We use global tomography models to model the mantle flow and the induced tectonic regimes. We gain new insights into how mantle dynamics account for surface observations, and more generally on the fundamental coupling between mantle, lithosphere and crust.

2.4 Objectives

1. To identify the most reliable database on tectonic regimes and SHmax orientations derived from focal mechanisms. Several databases are being considered as their outputs are sometimes contradictory.
2. To model the instantaneous mantle flow, the derived tectonic regimes and SHmax direction from tomography models
3. To study the sensitivity of the model parameters of the model, namely the input tomography models and viscosity laws.
4. To compare modeled and observed tectonic regimes and SHmax, to assess where the mantle dynamics may be responsible for the observed stress pattern.

2.5 Potential impact

The proposed study will improve our understanding on mantle dynamics and their influence on the distribution of earthquakes in the CEUS. It could therefore bring fundamental constraints on the coupling between deep phenomena and shallower phenomena, such as seismicity. This study will explore mantle dynamics, its interaction with the lithospheric plates, and their influence on the global tectonic systems. This work could enhance hazard prediction models for earthquakes.

Chapter 3 - Methods

This study aims to understand the influence of mantle dynamics on intraplate seismicity in the CEUS. We use global and regional tomography models to model the instantaneous mantle flow. By varying tomography models, the viscosity laws, and the conversion factor between seismic velocity anomalies and density anomalies, $R_{\rho/vs}$, we study the influence of model parameters on the mantle flow and induced tectonic regimes. Seismic velocity anomalies obtained from tomography models are converted into density anomalies using a conversion factor $R_{\rho/vs}$. Several recent conversion factors are tested in this study (Steinberger and Calderwood, 2006; Karato, 2008; Simmons et al., 2009; Lee et al., 2011; Adam et al., 2021). To compute the instantaneous mantle flow induced by these density anomalies, we solve the equations of mass and momentum under the Boussinesq approximation in a 3D spherical shell.

Mass and momentum equations:

$$\nabla . \mathrm{v} = 0 \tag{1}$$

$$-\nabla p + \nabla . \{\eta(\nabla \mathrm{v} + \nabla \mathrm{v}^{tr})\} + Ra_i \delta\rho e_r = 0 \tag{2}$$

with Ra_i, the Rayleigh number

$$Ra_i = \frac{\rho_0 g r_e^3}{k_0 \eta_0} \tag{3}$$

where p is the pressure, v is the velocity, η is the viscosity, δρ is the density anomaly, η_0 is the reference viscosity, k_0 is the reference thermal diffusivity and g is the gravitational acceleration.

The finite volume mantle convection code "ConvRS" (Yoshida, 2008, 2010; Adam et al., 2010, 2021) is used to calculate the instantaneous mantle flow.

3.1 Viscosity laws

The viscosity laws we test in this study are depth and/or temperature dependent. The depth dependent viscosity comprises a highly viscous lithosphere ($\eta=10^{24}$ Pa s) and the upper mantle with a viscosity $\eta=10^{21}$ Pa s. Our models are upper mantle models. For the temperature dependent viscosity, we use an Arrhenius type law (Equation 4)

$$\eta = \eta_{ref}(d)\exp\left(\frac{H_a}{T} - \frac{H_a}{T_{ref}}\right) \quad (4)$$

where H_a represents the activation enthalpy of mantle rock, R is the gas constant (8.31 kJ mol^{-1}), T is the dimensionless temperature, T_{ref} denote the reference temperature, $\eta_{ref}(d)$ is the dimensionless reference viscosity at $T = T_{ref}$. We use Ha=400 KJ mol-1(Adam et al., 2021a; 2021b) The viscosity laws we use in this study are described below.

Viscosity laws

1: viscosity is constant, $\eta_1=10^{21}$ Pa s

2: $\eta_2(Z)$

- $\eta=10^{24}$ Pa s Lithosphere (0-100 km depth)
- $\eta=10^{21}$ Pa s Upper mantle (100 - 660 km depth)

3: $\eta_3(Z)$, where the base of the lithosphere ($\eta_{lithosphere}=10^{23}$ Pa s) varies geographically accordingly to the models developed by

- a - CAM2016 (Priestley et al., 2019) (Figure 1a)
- b - WINTERC-G (Fullea et al., 2021) (Figure 1b)
- c - CAM2022 (Priestley et al., 2024) (Figure 1c)

4: $\eta_4(T)$ Arrhenius law with Ha=400 $KJmol^{-1}$ (Equation 4)

5: $\eta_5(T,Z) = \eta_4(T) * \eta_3(Z)$

6: $\eta_6(Z) = \eta_3(Z)$ + Weak Plate Boundaries (WPB)

7: $\eta_7(T) = \eta_4(T)$ + Weak Plate Boundaries (WPB)

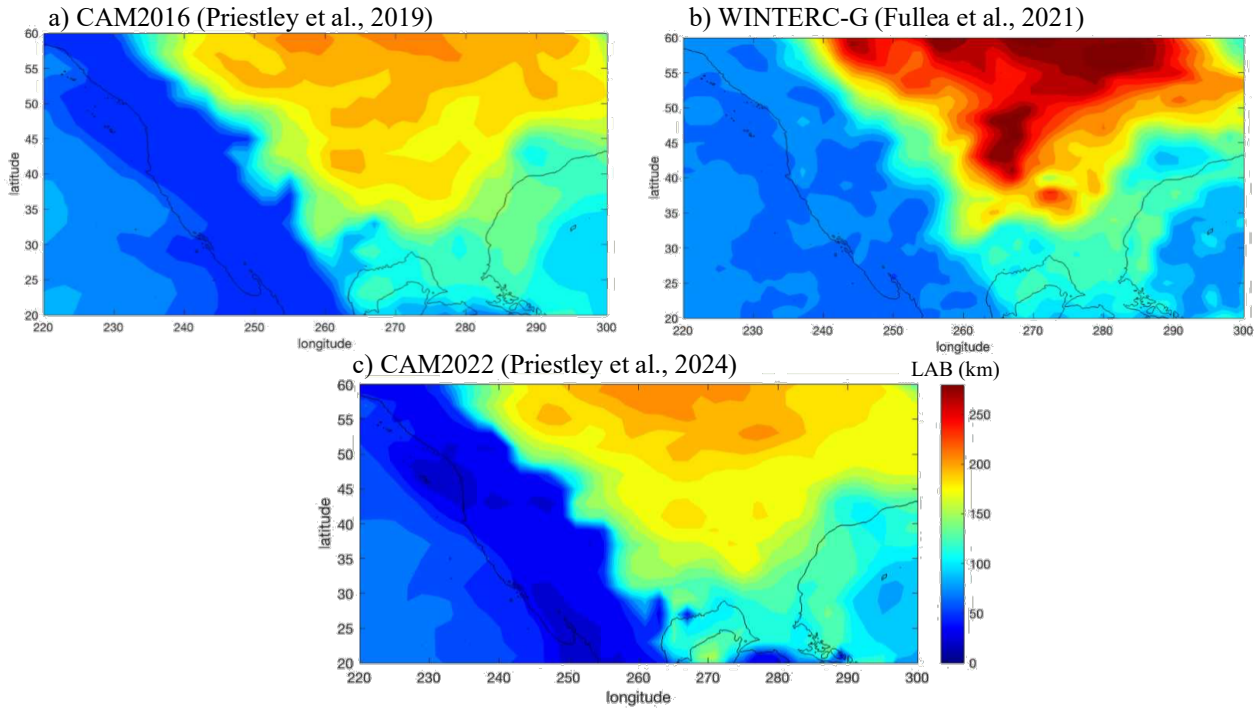

Figure 3.1: Lithosphere Asthenosphere Boundary (LAB) used in this study and derived from CAM2016 (Priestley et al., 2019), (a), WINTERC-G (Fullea et al., 2021), (b) and CAM2022 (Priestley et al., 2024), (c).

.

3.2 Tomography models

Tomography models provide the 3D structure of the Earth in terms of seismic velocity anomaly. Different tomography models use different input data (seismic travel time, waveform data) and different methods to inverse the data to obtain the result (French and Romanowicz, 2014 and references therein). Therefore, different tomography models provide different models of the Earth's structure. If a feature appears in only one or a few tomography models, it may be unreliable. However, if it shows in multiple models, it is more favorable to be a real feature of the Earth's structure. Therefore, considering several tomography models is important for identifying errors in the modeling process. In this study, we consider several global and regional tomography models.

3.2.1 Global tomography models

Global seismic tomography models provide the structure of the Earth at the global scale but may have lower resolution than regional models. SPiRaL (Simmons et al., 2021) is a one of the newest global models of wave speeds and anisotropy variations in the crust and mantle. The crust (including ice, water, sediments, and crystalline layers) is directly incorporated into the model. The default node spacing is approximately 2° in the lower mantle and 1° in the crust and upper mantle. TX2019slab (Lu et al., 2019) is a new P and S wave tomography model that contains theoretical three-dimensional subducting slab structures in the starting model. This has higher-amplitude subducting slabs compared with other models (Lu et al., 2019). SEMUCB-WM1 is the first radially anisotropic shear wave velocity model of the earth whole mantle, developed using spectral-element method (SEM) based forward waveform modeling (French and Romanowicz, 2014). These models used in our study. They are represented in Figure 3.2.

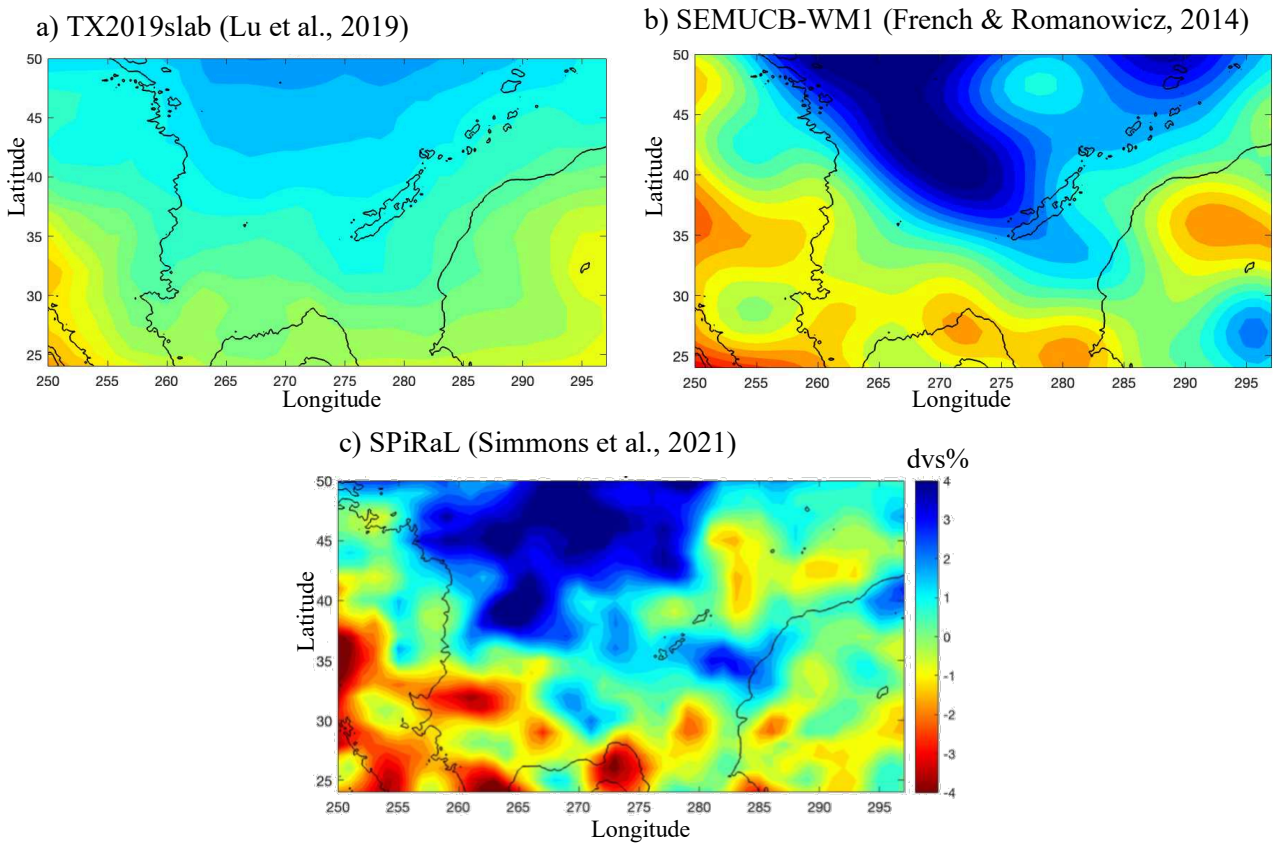

Figure 3.2: Variations of seismic velocity anomaly, dvs, imaged by different global tomography models considered in this study at 200 km depth, a) TX2019slab (Lu et al., 2019); b) SEMUCB-WM1 (French and Romanowicz, 2014); c) SPiRaL (Simmons et al., 2021). The black lines are the 0 and 2500 m isolines (data from Tozer et al., (2019)).

3.2.2 Regional tomography models

Regional models provide a more detailed view than global tomography models, mainly using data from USArray, a mobile seismic array that has imaged the North American sub-continental lithospheric mantle during the last 19 years.

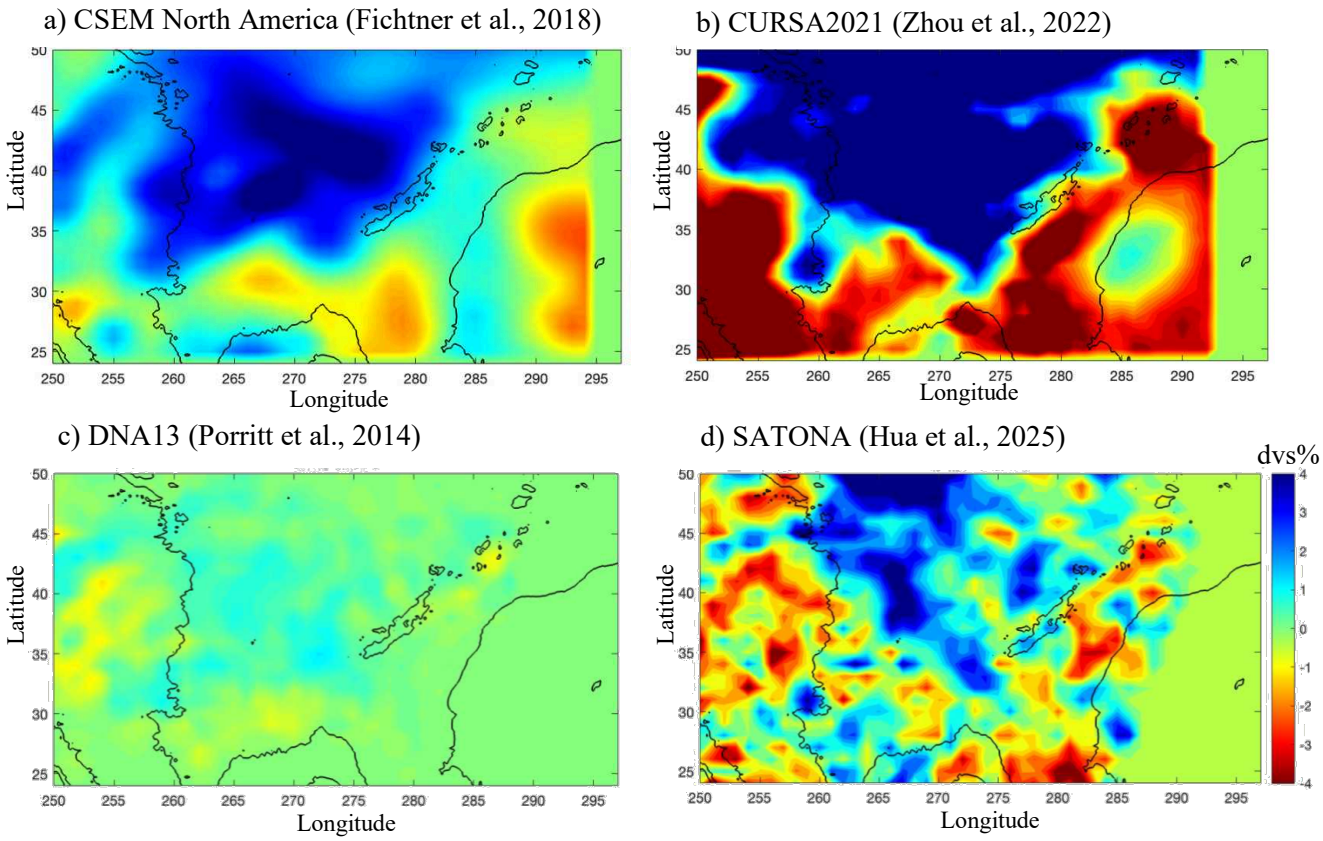

Figure 3.3: Variations of seismic velocity anomaly, dvs, imaged by different regional tomography models considered in this study at 200 km depth, a) CSEM_North_America model (Fichtner et al., 2018) ; b) CURSA2021(Zhou et al., 2022); c) DNA13(Porritt et al., 2014); d) SATONA (Hua et al., 2025). The black lines are the 0 and 2500 m isolines (data from Tozer et al. (2019)).

DNA13 model uses independent SH and SV data, teleseismic P wave observations, and surface wave phase velocities from both teleseismic earthquakes and ambient noise to determine relative wave speeds from crust to the lower mantle (Porritt et al., 2014). CSEM_North_America model contains 12 refinements derived from full seismic waveform inversions of regional to global scale models (Fichtner et al., 2018). This model presents a new framework that enables collaborative geophysical data inversion by integrating prior knowledge from earlier studies. The CUSRA2021 model is based on frequency-dependent travel time measurements, from 160 earthquake events recorded by 5,280 stations (Zhou et al., 2022). It includes large number of intraplate earthquakes

which improves the data coverage in eastern United States. SATONA is a tomography model developed using full-waveform adjoint tomography to resolve fine-scale seismic structures beneath North America (Hua et al., 2015). These are some of the regional models we use in our study. They are represented in Figure 3.3.

3.3 Conversion factors

Seismic velocity anomalies obtained from tomography models should be converted into density anomalies using a conversion factor.

The density to velocity heterogeneity ratio is expressed as,

$$\frac{\delta\rho}{\rho_{ref}} = R_{\rho/v}\frac{\delta v}{v_{ref}} \quad (5)$$

where $\delta\rho$ is the density anomaly and ρ_{ref} the density along the 1600 K adiabat (Karato, 2008). In this study, we use Steinberger and Calderwood (2006), Karato (2008), Simmons et al. (2009), Lee et al. (2011) and Adam et al. (2022) conversion factors.

3.4 Geodynamic modeling

Figure 3.4 illustrates some of our model parameters. It shows the seismic velocity anomalies provided by the SEMUCB-WM1 tomography model (panel a) and the density anomalies obtained with Adam et al. (2021) conversion factor (panel b) along a profile at latitude 45ºN. In Figure 3b the arrows represent the instantaneous mantle flow induced by the density anomalies. Figure 3c shows the viscosity when the law $\eta_6(z)$ is being implemented. In the depth cross section displayed in Figure 3b, blue regions represent cooler and denser materials associated and they are associated with a downwelling flow, while red regions indicate hot and buoyant materials that are associated with upwelling flow.

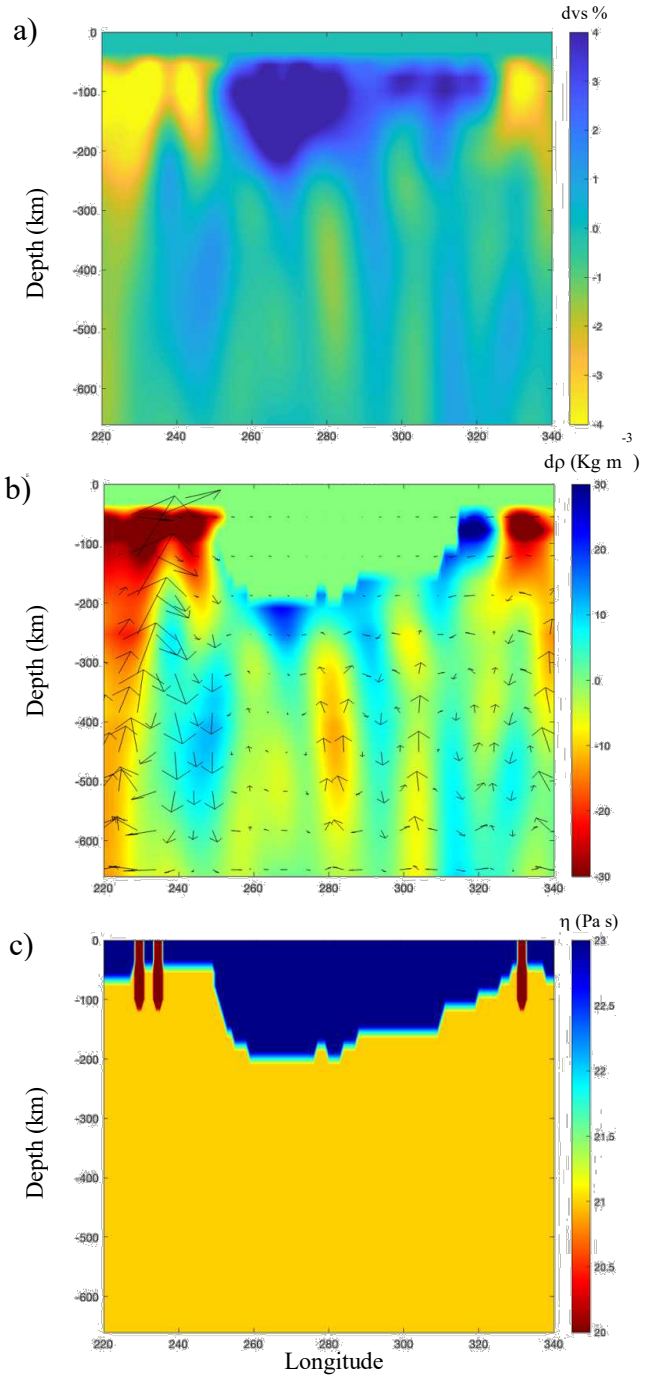

Figure 3.4: Illustration of the model parameters. Depth cross sections at latitude 45ºN across the SEMUCB-WM1 tomography model (French & Romanowicz, 2015) (a), the density anomalies computed by considering Adam et al. (2022) conversion factor (b), and the viscosity ($\eta_6(z)$) (c). Here we use CAM2022 model (Priestley et al., 2024) for the base of the lithosphere. The arrows in panel b represent the convection pattern induced by the density anomalies.

3.5 Tectonic regimes and SH_{max} computation

Using the modelled convection velocities defining the instantaneous mantle flow, we compute the stress tensor in a spherical coordinate system. Each component of the stress tensor is derived from the spatial derivative of the modeled convection velocities.

For example, σ_{rr} is computed through the equation

$$\sigma_{rr} = -p + 2\eta\frac{\partial v_r}{\partial r} \quad (6)$$

Where p is pressure and η is the viscosity. By considering the spatial derivatives of the convection velocities along the radial, r, longitude φ, and latitude θ, directions, we then obtain a 3× 3 matrix defining the stress tensor (Appendix 1).

The deviatoric stress is the stress tensor component responsible for distortion without changing the volume. Numerically, this can be calculated by subtracting the hydrostatic stress (Equation 7) from the total stress (Equation 8).

$$\sigma_{mm} = \frac{\sigma_{xx}+\sigma_{yy}+\sigma_{zz}}{3} \quad (7)$$

$$\sigma' = \sigma - \begin{bmatrix} \sigma_{mm} & 0 & 0 \\ 0 & \sigma_{mm} & 0 \\ 0 & 0 & \sigma_{mm} \end{bmatrix} \quad (8)$$

This deviatoric stress, σ', is then used to determine the principal stresses by computing the eigenvalues and eigen vectors. The tectonic regimes and the maximum horizontal stress, SH_{max}, are then computed following the method developed by Heidbach et al. (2010) (Figure 3.5). If the biggest eigenvector is vertical, the tectonic regime is normal, if the smallest eigen vector is the

most vertical, then we have a thrust regime, if the intermediate eigen vector is the most vertical, then the regime is strike-slip.

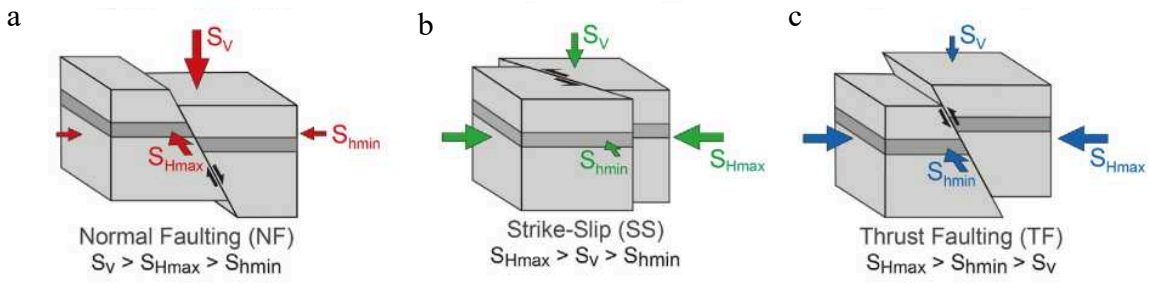

Figure 3.5: Illustration of the method used to define tectonic regimes (from Heidbach et al. (2018)). The definition uses SH_{max} (maximum horizontal stress), Sh_{min} (minimum horizontal stress) and S_V (vertical stress). Normal fault regime occurs where the vertical stress is larger than the horizontal stresses (a); strike-slip fault regime occurs where the vertical stress is the intermediate principal stress (b); thrust fault regime occurs where the vertical stress is smaller than the horizontal stresses (c).

3.6 Surface observation comparison

We compare the modeled tectonic regimes and SH_{max} with the observations obtained by several recent databases including Levandowski et al. (2018) and Snee and Zoback (2020) derived mainly from earthquakes focal mechanisms, in situ wellbore measurements and hydraulic fracturing. They are displayed in Figure 3.6. We choose to compare our results with Levandowski et al. (2018) because it provides the most comprehensive data of our study region. We study how the stress pattern changes with depth by considering depths between from 33 km to 253 km. The step along the depth direction is indeed 22 km and 1° along latitude and longitude.

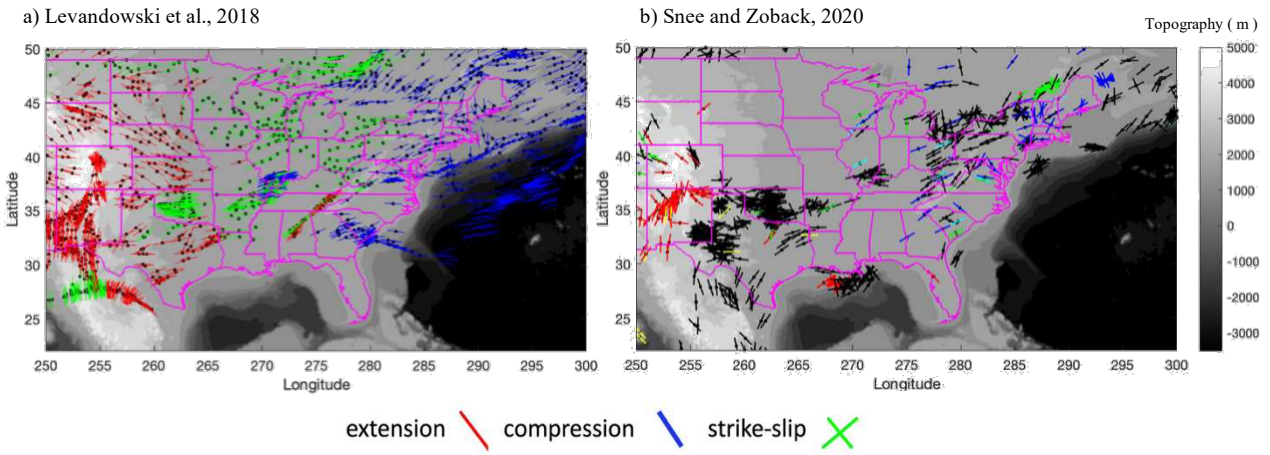

Figure 3.6: Stress maps showing observed tectonic regimes across the CEUS based on the study by Levandowski et al. (2018) (a) and Snee and Zoback (2020) (b). Lines represent the orientation of SH_{max}. Extension regimes are displayed in red, compression regimes in blue, strike slip in green, while the unknown regimes are displayed in black. Black dots represent the earthquake locations. The magenta lines mark state boundaries (https://www.census.gov/geographies/mapping-files/time-series/geo/carto-boundary-file.html). Levandowski et al. (2018) is used for the comparison between modeled and observed tectonic regimes.

3.7 Quantitative assessment of tectonic regime and SH_{max} orientations correlation

We quantify the fit between the modeled and observed tectonic regimes. The grid along which we compute the mantle flow is a one degree by one degree grid along the latitude and longitude directions. We interpolate the observations (Figure 3.6) along the same grid. Along each point of this grid, we assign a value of 0 if the modeled regime reproduces the observed one. Alternatively, we assign a value of 1 is the modeled and observed tectonic regimes differ (Figure 3.7).

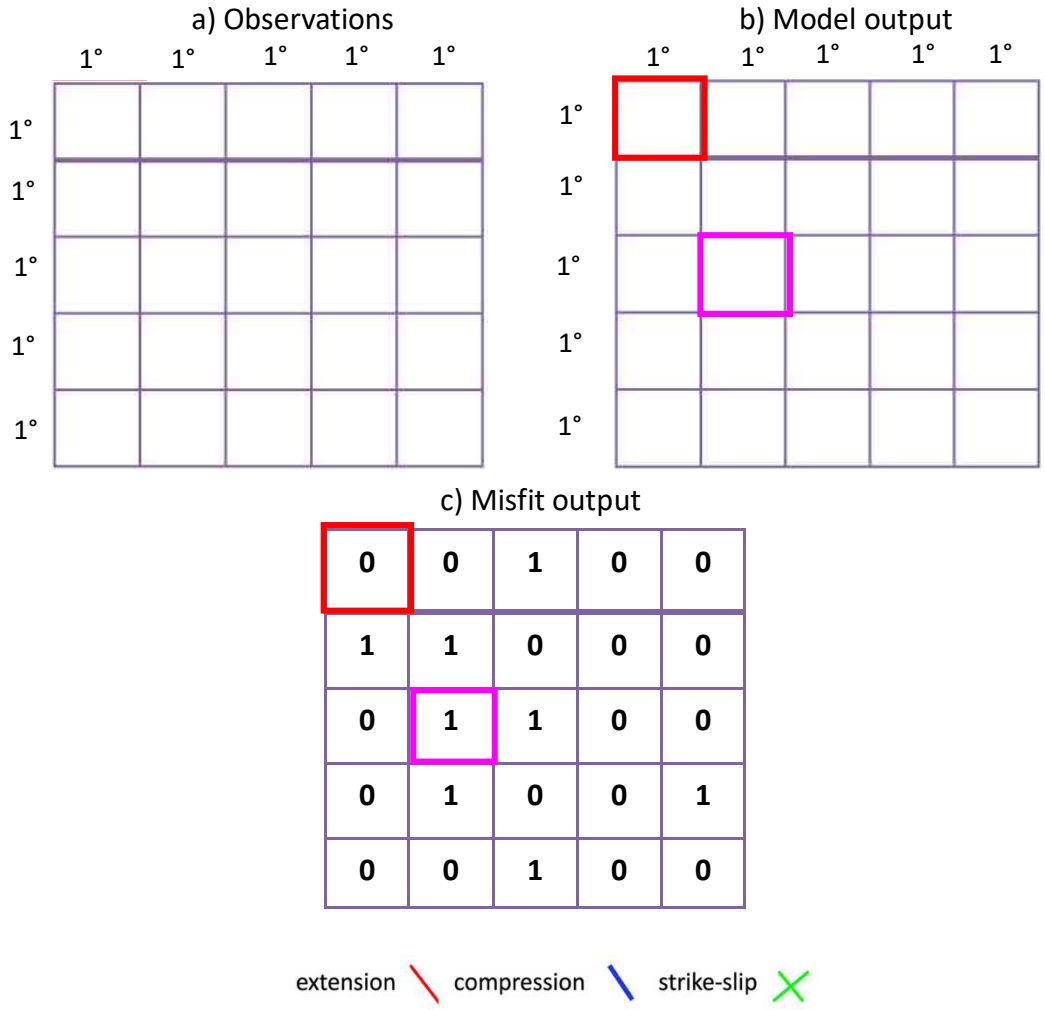

Figure 3.7: Illustration of our quantification of the fit between observed tectonic regimes (a) and modeled tectonic regimes (b). Matching cells are assigned a value of 0 (magenta color box), while different cells are assigned a value of 1 (red color box) in the resulting misfit output (c). The black boxes represent the one degree by one degree grid used in our study.

We then compute the RMS (Root Mean Square) for each model. The model with the smallest RMS provides in theory the best fit to the observations.

$$RMS = \sqrt{\frac{1}{n}\sum_{i=1}^{n}(obs_i - model_i)^2} \quad (9)$$

For the maximal shear orientation, SH_{max}, we calculate differences between the modeled and observed SH_{max} only when the modeled tectonic regimes reproduce the observed tectonic regime (Figure 3.8). An RMS for is computed for SH_{max} as well.

a) Observations

	1°	1°	1°	1°	1°
1°	134	50		20	14
1°	121	13	45	32	
1°	55	42	18	75	35
1°		48	35		77
1°	43	55		82	45

b) Model output

	1°	1°	1°	1°	1°
1°	20	10		20	5
1°	55	5	40	14	
1°	20	42	5	60	34
1°		40	20		60
1°	40	20		40	30

c) Difference

114	40		0	9
66	8	5	18	
35	0	13	15	1
	8	15		17
3	35		42	15

Figure 3.8: Illustration of our quantification of the difference (c) between observed SH_{max} orientations (a) and modeled SH_{max} orientations (b). This calculation is performed only when the modeled regimes reproduce the observed ones. The black boxes represent the one degree by one degree grid used in our study.

Chapter 4 - Results

In this chapter we display and examine the flow pattern modeled from tomography models over the North American continent, and especially over CEUS. We also investigate the tectonic regimes and SH_{max} induced by the instantaneous mantle flow. Moreover, we compare the modeled tectonic regimes and SH_{max} with the ones constrained from surface observations to see to which extent the mantle flow can account for the surface seismicity. We also study the influence of different factors such as tomography models, viscosity laws, conversion factors and weak plate boundary tests on the modeled mantle flow and the derived tectonic regimes and SH_{max}.

4.1 Tomography models

Tomography models represent the 3D structure of the Earth based on seismic velocity anomalies. Different tomography models use different input data and inversion methods, leading to a different earth structure (Chapter 3, section 3.2). Features that appear in several models are more likely to be solid features, representative of the real mantle structure. Therefore, we consider recent and widely used global and regional tomography models to reduce the error and improve reliability.

4.1.1 Global tomography models

We test the influence of global tomography models using SEMUCB-WM1 (French & Romanowicz, 2014), SPiRaL (Simmons et al., 2021) and TX2019slab (Lu et al., 2019) tomography models. First, we vary the input global tomography model, while keeping the other parameters constant. We convert seismic velocity anomalies obtained from tomography models into density anomalies using the conversion factor, $R_{\rho/vs}$ derived by Adam et al. (2021) and the depth dependent viscosity where the lithosphere thickness is based on CAM2022 model (Priestley et al.,

2024) (viscosity law $\eta_3(z)$, section 3.1), thus allowing the lithosphere thickness to vary geographically.

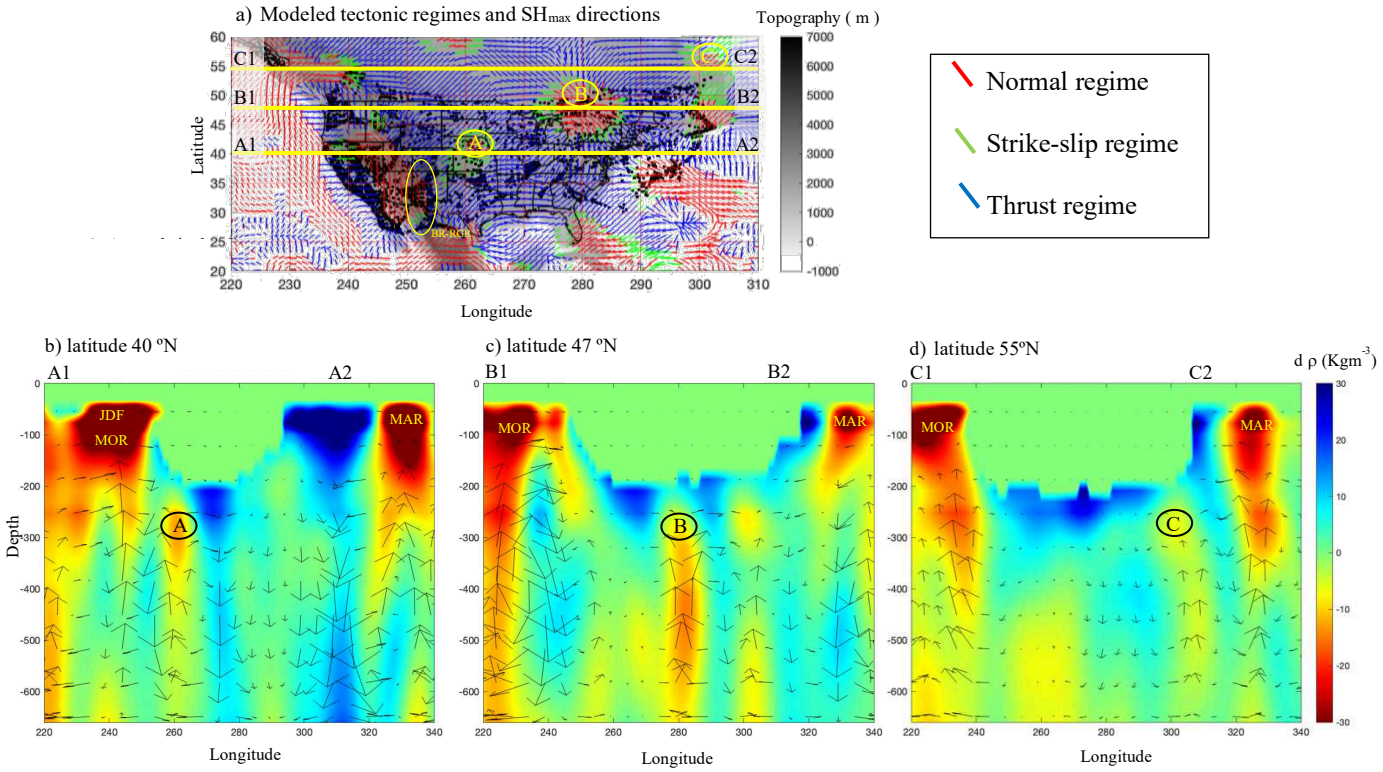

Figure 4.1: Modeled tectonic regimes and mantle flow. (a) Modeled tectonic regimes and SH_{max} directions computed with the SEMUCB-WM1 tomography model (French & Romanowicz, 2014) at 99 km depth. The model uses a depth dependent viscosity based on the CAM2022 lithosphere thickness (Priestley et al., 2024), (viscosity law $\eta_3(z)$, section 3.1), and the conversion factor between seismic velocity anomalies and density anomalies, $R_{\rho/vs}$, developed by Adam et al. (2021). Lines represent the orientation of SH_{max}. Extension regimes are displayed in red, compression regimes in blue and strike slip in green. The gray map represents the topography (data from Tozer et al. (2019)) and black dots the seismicity (data from Levandowski et al. (2018)). Thin black lines mark the state boundaries. The lowermost panels display the instantaneous mantle flow at different latitude, (b) latitude 40ºN, (c) latitude 47ºN and (d) latitude 55ºN. Abbreviations used in the Figure 4.1 are BR-RGR for Basin and Range-Rio Grande Rift, JDF for the Juan de Fuca Plate, MOR for the Mid Oceanic Ridge and MAR for the Mid-Atlantic Ridge. Arrows in the lower panel indicate the instantaneous flow induced by the density anomalies.

Figure 4.1 shows the mantle flow computed with these parameters, as well as the induced tectonic regimes. We can see that the BR-RGR region is related with an extension regime and most of the CEUS, are associated with a compressive regime. However, there are some areas, such as the ones highlighted by the letters A, B and C, where the modeled regime is either extensional and/or strike-slip. The region highlighted by the letter A is in Nebraska. Region B roughly spreads between the Greate lakes, Ontario and Quebec. Region C is near Nova Scotia, which lies at the margin of our study area.

To understand what creates these tectonic regimes, we consider depth cross sections at different latitudes (Figure 4.1b-d). The colormap on Figure 4.1b-d represent the density anomalies and the arrows, the flow induced by these anomalies. Red regions represent negative density anomalies, i.e., buoyant material, and are associated with upwelling flow, while blue regions represent positive density anomalies and are therefore associated with downwelling flow. Upwellings in a middle of a continent, such as the ones occurring at longitudes 260°E, 280°E and 300°E are unexpected. Such upwellings create extension regimes at depth 99 km (Figure 4.1a).

Additionally, we investigate how the modeled tectonic regimes changes with depth by considering depths between 33 km and 253 km. The step along the depth direction is indeed 22 km as described in chapter 3, section 3.4. Figure 4.2 shows how the stress changes with depth for models based on the SEMUCB-WM1 tomography model with depth dependent viscosity based on lithosphere thickness CAM2022 model (viscosity law $\eta_3(z)$, section 3.1) and Adam et al. (2021) conversion factor.

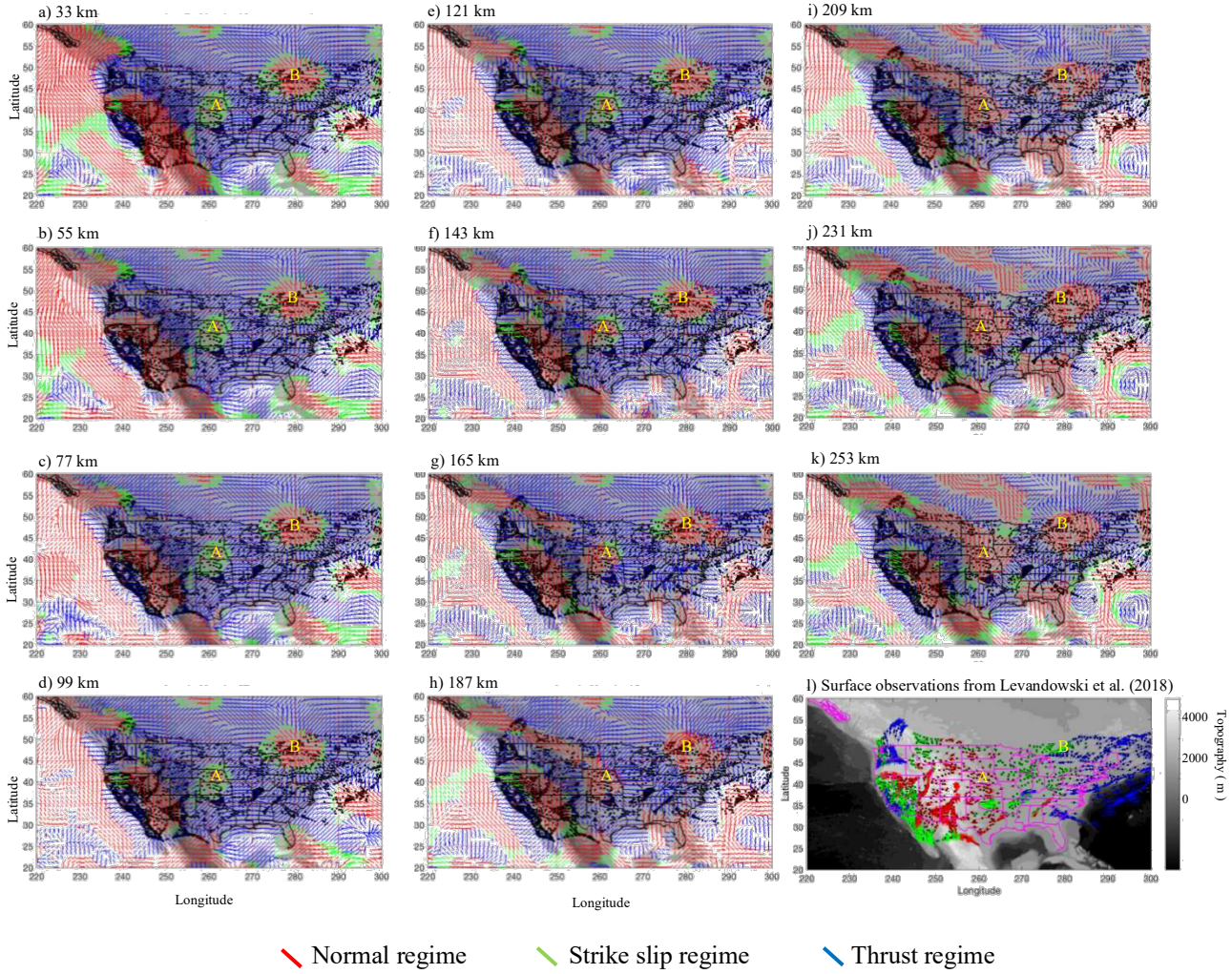

Figure 4.2: Modeled tectonic regimes varying with depth for the SEMUCB-WM1 model. The viscosity is depth dependent based on CAM2022 model (viscosity law $\eta_3(z)$, section 3.1) and the $R_{\rho/vs}$ is from Adam et al. (2021). Panels a-k: each panel shows the modeled tectonic regimes (see color scale legend) and the SH_{max} directions at depths reported on top of each panel. Black dots: seismicity from Levandowski et al. (2018). l) Surface observations taken from Levandowski et al. (2018). The black (a-k) and magenta (l) lines mark state boundaries (https://www.census.gov/geographies/mapping-files/time-series/geo/carto-boundary-file.html).

The modeled tectonic regimes and SH_{max} directions seem to be consistent over CEUS for depths 33-165 km. Most of the northern and part of the American continent, including CEUS are indeed associated with a modeled compressive regime, with two regions highlighted by the letters A, B associated with extensional regimes, surrounded by strike-slip regimes. Region C is not included

as it lies at the margin of our study area. While the extension regime (red lines) can be seen up to depths 253 km, the strike-slip regime (green lines) slowly disappears at depths 143-165 km. For depths greater than 253 km, the modeled regime pattern becomes more complex.

When comparing the modeled tectonic regimes with the surface observations obtained from Levandowski et al. (2018), we can see that our models recover partially the observed compression in the Northeastern US. However, the strike slips regimes observed in the central US are generally not recovered. The only strike-slip regimes obtained by our models are around regions A and B, between depths 33 and 165 km.

Figure 4.3 shows a zoom in over the Central and Eastern U.S. At shallow depths (33 - 77km), the Basin & Range, Rio Grande Rift region (BR-RGR hereafter) is associated with extensional regime and mix with strike slip regimes at greater depths. All seismic zones are associated with compressive regime at all depths, except for the SCSZ. SCSZ is still associated with a compressive regime at shallow depths (33-165 km) but it associates with extensional regime at depths greater than 187 km.

Table 4.1 summarizes the comparison between the modeled and observed tectonic regimes from Levandowski et al. (2018). Our model reproduces very well the observed extension regime and N-S oriented SH_{max} over the BR-RGR region at shallow depths (33-55 km), while at greater depths we observe a mix of extensional and strike-slip regimes and the SH_{max} direction changes. The compressional regime in the NMSZ is consistently retrieved at all the depths, but we do not retrieve the ENE-WSW direction, instead we have a SH_{max} direction of NNE-SSW.

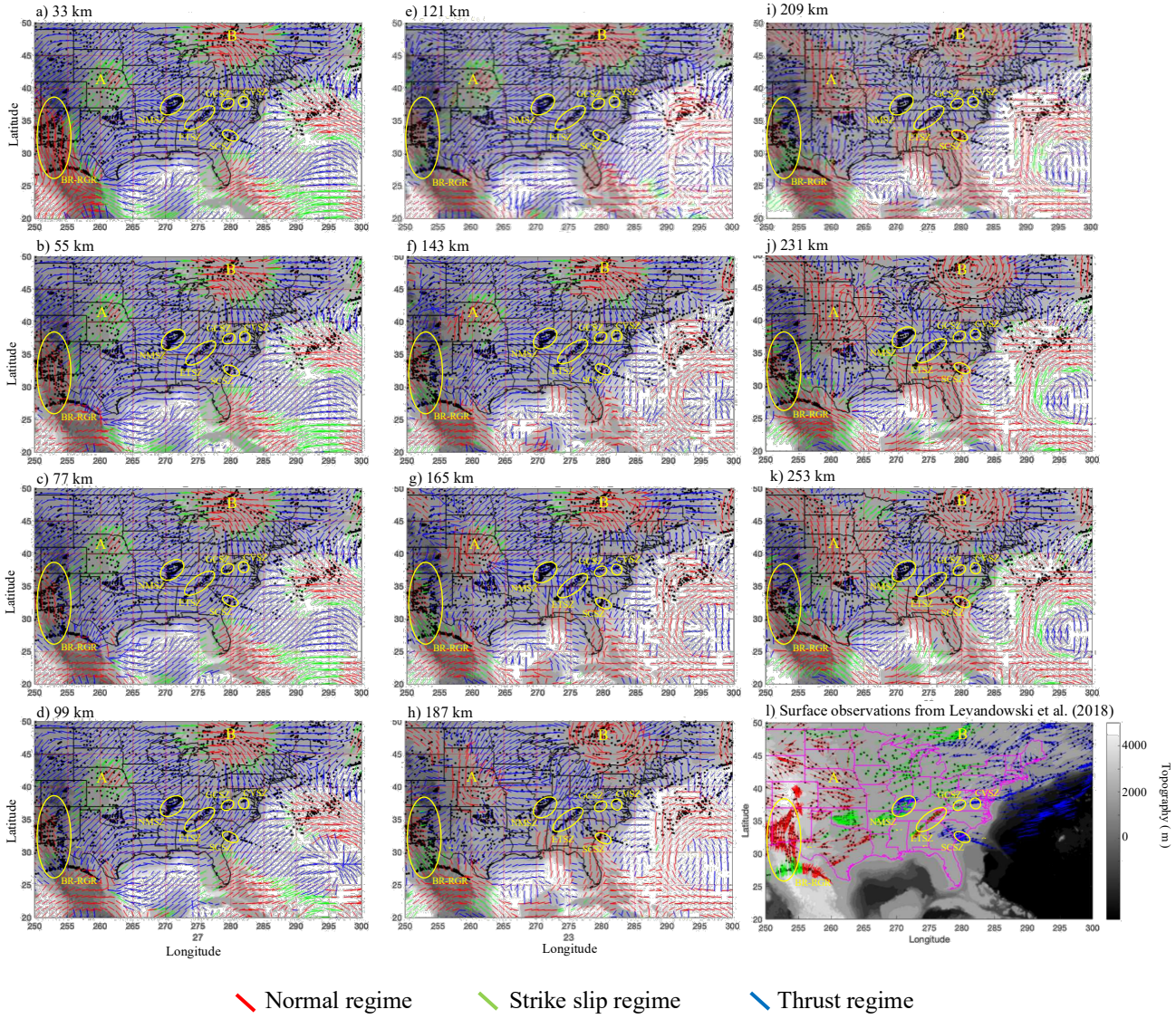

Figure 4.3: Variation of tectonic regimes with depth for the SEMUCB-WM1 model across the Central and Eastern United States (CEUS). The viscosity is depth dependent based on CAM2022 model (viscosity law $\eta_3(z)$, section 3.1) and the $R_{\rho/vs}$ is from Adam et al. (2021). Circled areas are the Basin and Range - Rio Grande Rift (BR-RGR) and the major seismic zones, including New Madrid Seismic Zone (NMSZ), Eastern Tennessee Seismic Zone (ETSZ), South Carolina Seismic Zone (SCSZ), Giles County Seismic Zone (GCSZ) and Central Virginia Seismic Zone (CVSZ). Panels a-k: each panel shows the modeled tectonic regimes (see color scale legend) and the SH_{max} directions at depths reported on top of each panel. Black dots: seismicity from Levandowski et al. (2018). l) Surface observations taken from Levandowski et al. (2018). The black (a-k) and magenta (l) lines mark state boundaries (https://www.census.gov/geographies/mapping-files/time-series/geo/carto-boundary-file.html).

The extensional and strike-slip regimes along the ETSZ are not reproduced at any depth. The GCSZ and CVSZ recover the observed compressional regime at all depths and SCSZ at 33 to 165 km depth while the GCSZ does not exhibit the observed strike-slip at any depth. While the NE-SW SH_{max} direction is reproduced in the SCSZ at depths greater than 209 km, the modeled SH_{max} orientations in the GCSZ and CVSZ remain inconsistent at all depths.

We also model the instantaneous flow and the induced tectonic regimes with the SPiRaL tomography model (Simmons et al., 2021), (Figure 4.4). We keep the other model parameters constant. As previously, we use a depth dependent viscosity based on lithosphere thickness CAM2022 model (viscosity law $\eta_3(z)$, section 3.1) and the conversion factor between seismic velocity anomalies and density anomalies, $R_{\rho/vs}$, developed by Adam et al. (2021).

In the modeled tectonic regime figure (Figure 4.4a), we can see that a large portion of the easter part of the North American continent, between latitudes 35 and 53°N and longitudes 280 and 295°E is associated with extensional regimes, surrounded by strikes-lip regimes north and south. CEUS lies south-west of this region, and therefore its eastern extremity is associated with extensional regimes north, and strike-slip regimes in the middle of southern part. Besides this, most of CEUS is characterized by compressional regimes. Even BR-RGR is associated with mainly compressional regimes mixed with a few extensional regimes.

The depth cross section along the A1A2 profile, at latitude 40 ^{o}N, (Figure 4.4b), shows a prominent upwelling associated with the A extension region, previously identified with the SEMUCB-WM1 tomography model. At latitude 47 ^{o}N (Figure 4.4c), upwellings are more widespread between

260°E and 300°E, and a similar widespread upwelling pattern can be seen in the cross section at latitude 55 ºN (Figure 4.4d).

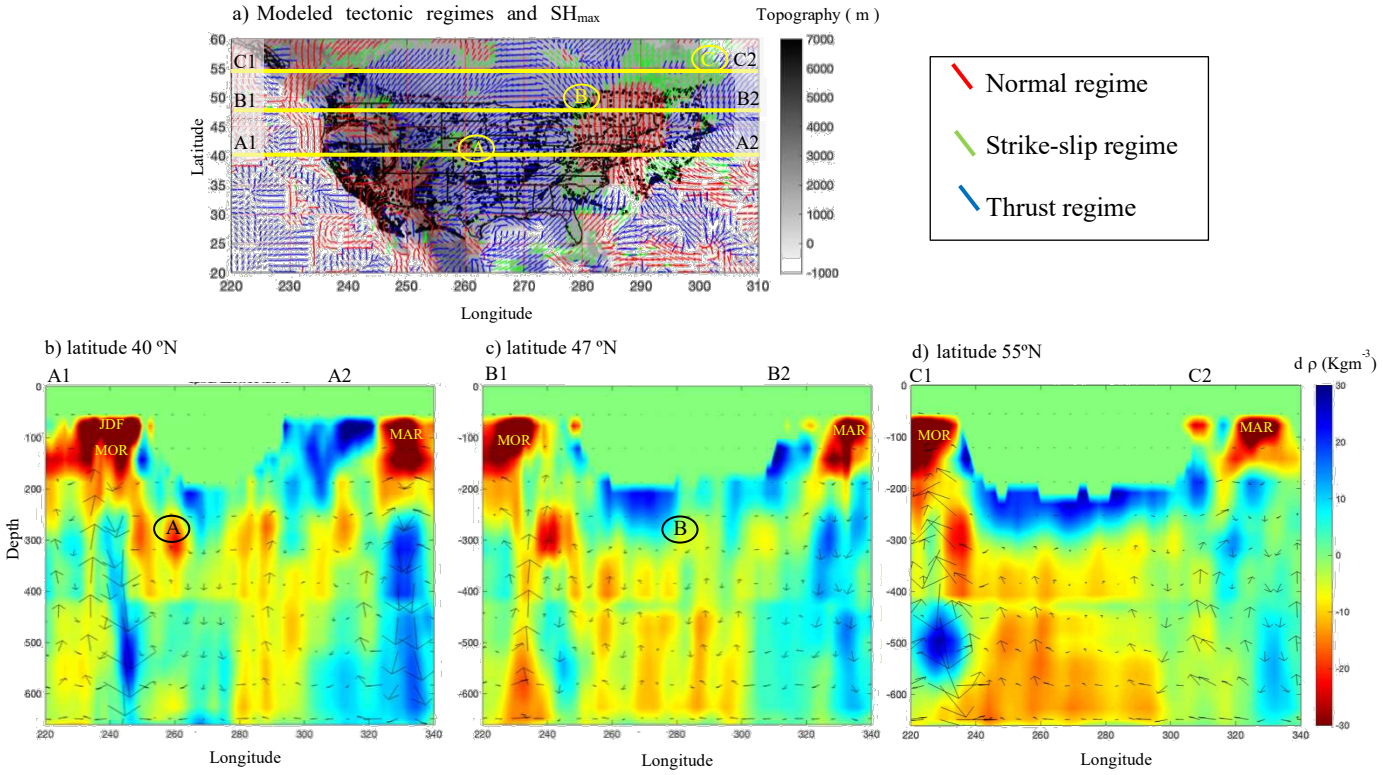

Figure 4.4: Same as Figure 4.1, for the SPiRaL tomography model (Simmons et al., 2021). Regions A, B, anc C are the upwelling zones indentified from the corresponding depth cross sections of the SEMUCB-WM1 tomography model (Figure 4.1).

We also consider how the tectonic regimes and SH_{max} directions modeled from the SPiRaL tomography model (Simmons et al., 2021) vary with depth (Figure 4.5). As previously, the viscosity is depth dependent, based on lithosphere thickness CAM2022 model (viscosity law $\eta_3(z)$, section 3.1) and the conversion factor between seismic velocity anomalies and density anomalies, $R_{\rho/vs}$, is from Adam et al. (2021).

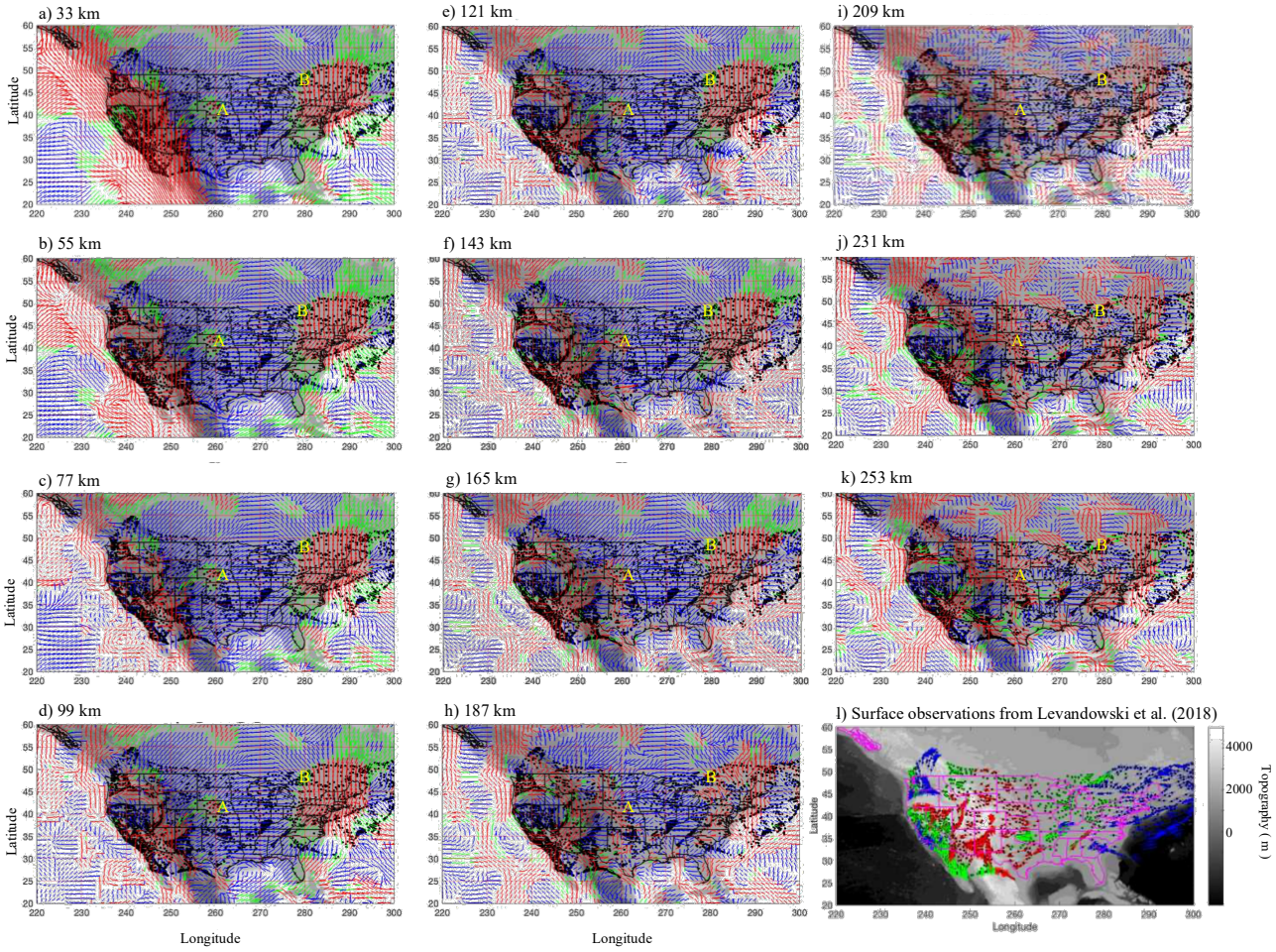

Figure 4.5: Same as Figure 4.2, for SPiRaL tomography model (Simmons et al., 2021).

At 33 km depth, most of CEUS is compression with two extension regions A and the northeastern extremity of CEUS, which lies near region B, the large region associated with extension regimes discussed earlier. The similar tectonic regime pattern can be seen up to 143 km depth. For depths greater than 143 km we do not have strike slip regimes, and the pattern becomes more complex. The regions A and B are still associated with extension until 187 km depth.

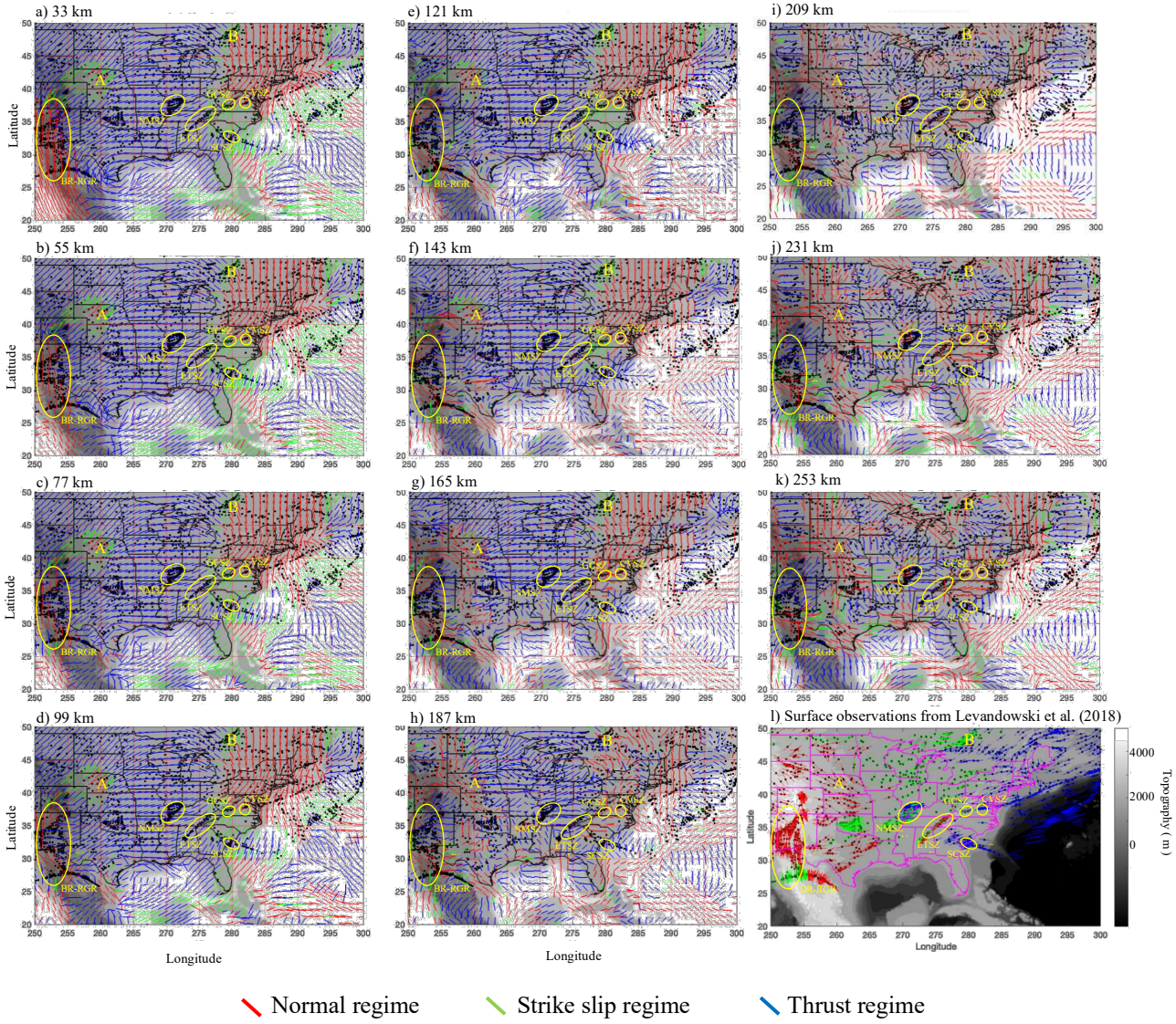

Figure 4.6: Same as Figure 4.3, for the SPiRaL tomography model (Simmons et al., 2021).

For the SPiRaL tomography model, the variation of modeled tectonic regimes with depth, across Central and Eastern U.S, is shown in Figure 4.6. At shallow depths, the BR-RGR region is associated with a combination of compressional and extensional regimes. Some strike-slip regimes are also seen at depths greater than 121 km. The NMSZ and ETSZ show compression up to 187 km depth, beyond, both extensional and compressional regimes can be observed. The SCSZ,

GSCZ and CVSZ display strike-slip regime up to 143 km depth and then at greater depths (187-253 km), SCSZ show compression regime while GCSZ and CVSZ are dominated by extension. When comparing the seismic zones highlighted by ellipses in Figure 4.6 with the surface observations from Levandowski et al. (2018), we notice that our model partially recovers the extension regimes in the BR-RGR region and shows N-S oriented SH_{max} at shallow depth from 33 km to 77 km. The observed compression regime over the NMSZ is recovered at all depths, but the modeled SH_{max} direction is slightly more oblique (~10°).

In our model, ETSZ is associated with compression regimes for depths 33-187 km. However the observed extension regimes are partially reproduced at deeper depths (209-231 km), but with a modeled SH_{max} directions different from the observed one. Most of the observed compression regimes are reproduced over the sesismic zones, except along the CVSZ. Up to 121 km depth, most seismic zones except NMSZ, exhibit the observed NE-SW oriented SH_{max}. Additionally, the strike-slip regime in the GCSZ is reproduced up to 143 km depth.

The test is repeated with the TX2019slab tomography model (Lu et al., 2019) (Figure 4.7). In the modeled tectonic regime figure (Figure 4.7a), almost the entire CEUS region characterized by compression regimes, at the exception of the northwest extremity (the easternmost part of Virginia and North Carolina) which is associated with a strike slip regime. The extension regions we found earlier (Figure 4.1a), A region in Nebraska has disappeared while B region which was roughly spreading between the Greate lakes, Ontario and Quebec has slightly shifted. In the depth cross section along A1A2 profile (Figure 4.7b), the upwelling associated with the region A is present, however with smaller relative amplitude compared to the amplitude of the upwelling occurring

outside the continental part. Indeed, in the previous models, the upwellings occurring beneath mid-oceanic ridges have a similar amplitude to the upwellings occurring beneath the North American continent (Fig 4.1, 4.3). In is not the case for the TX2019slab tomography model (Figure 4.7b). Similarly, in the depth cross sections along the profiles B1B2 (Figure 4.7c) and C1C2 (Figure 4.7d), the corresponding upwellings for regions B and C are observed, although with relatively smaller amplitudes compared to the amplitude of the upwellings occurring outside the continent.

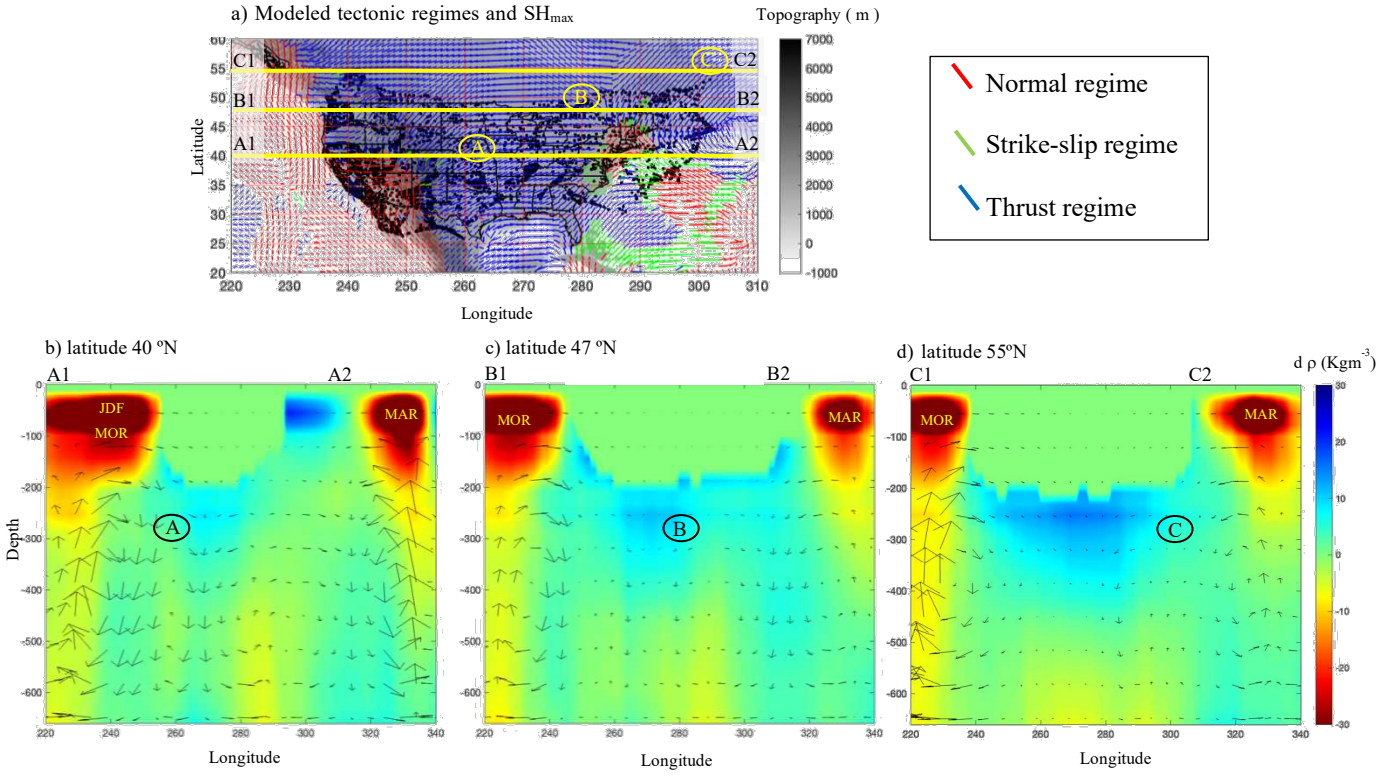

Figure 4.7: Same as Figure 4.1, for the TX2019slab tomography model (Lu et al., 2019). Regions A, B, anc C are the upwelling zones indentified from the corresponding depth cross setions of the SEMUCB-WM1 tomography model (Figure 4.1).

The modeled tectonic regime pattern remains almost unchanged from 33 km up to 143 km (Figure 4.8). For depths greater than165 km, the regime pattern becomes more complex having additional extensional regimes in the CEUS region. Additionally, the region A, previously identified as an extension region in Nebraska with SEMUCB-WM1 tomography model (Figure 4.1a) is absent at

all depths. As stated previously, CEUS is associated with compression regimes in our model. The extension in region B, previously identified with the SEMUCB-WM1 tomography model, remains

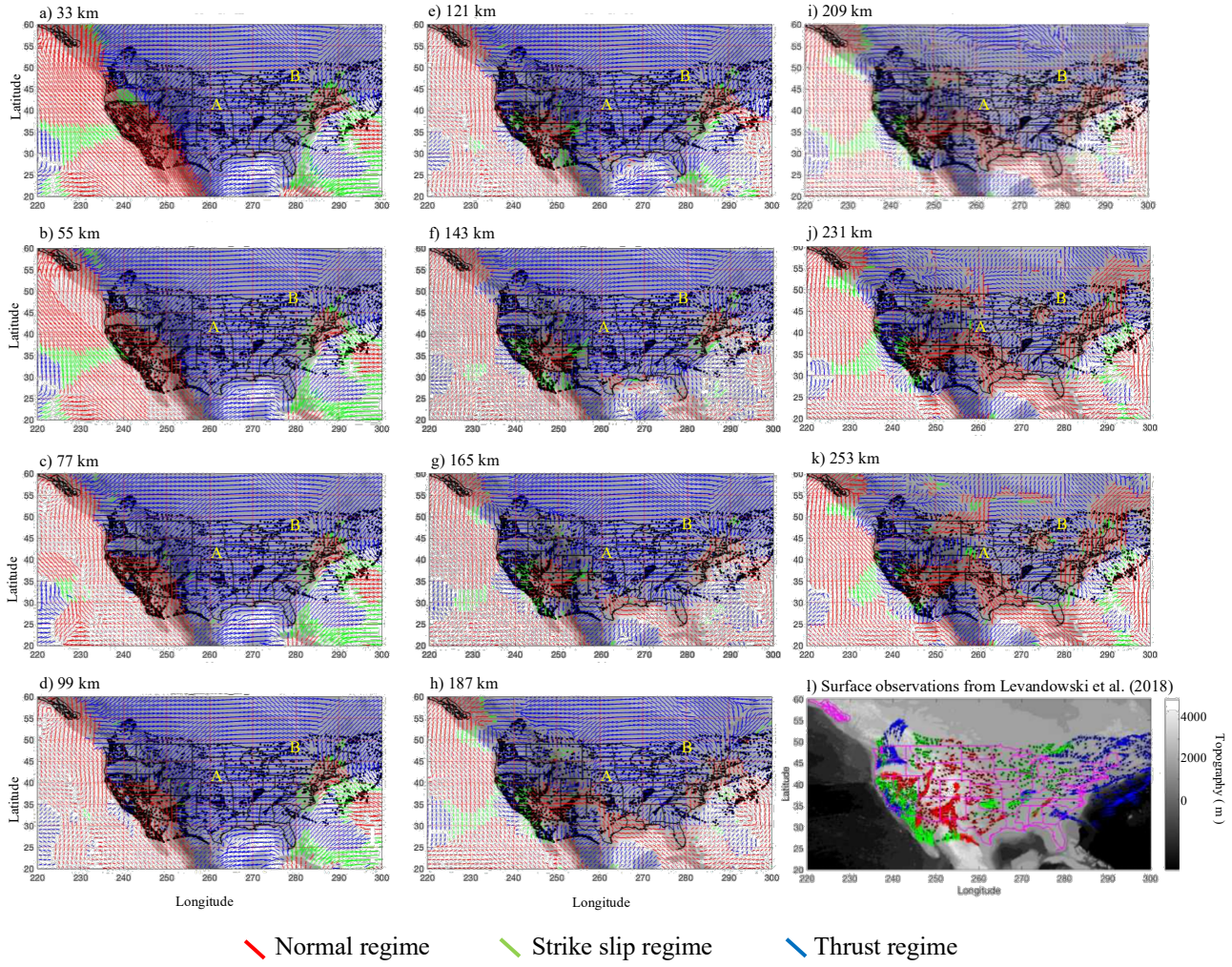

present but is shifted to the southeast.

Figure 4.8: Same as Figure 4.2, for the TX2019slab tomography model (Lu et al., 2019).

The compressional regimes in Northeastern U.S are well reproduced at all depths, and the general SH_{max} direction, NE-SW, is retrieved until 165 km depth. The extension and strike-slip regimes in CEUS are not well retrieved at any depth.

For TX2019slab tomography model, a zoomed view of CEUS, showing the variation of tectonic regimes with depths is shown in the Figure 4.9. At all depths, the BR-RGR region is associated with both compression and extension regimes, except depths between 121 km and 165 km, where strike-slip regime is also present. The NMSZ, ETSZ and SCSZ exhibit compression regime at all depths. At shallow depth, the GCSZ is related with compression, while the CVSZ is associated with strike-slip regime. At depths greater than 187 km, both zones change and show extensional regimes.

The model retrieves the observed extension regimes in the BR-RGR region and the N-S SH_{max} direction for depths from 33 km to 99 km. The compression regime and ENE-WSW oriented SH_{max} in the NMSZ are consistently reproduced across all the depths, whereas the extension and strike-slip regimes in the ETSZ are not recovered at any depth. The compressional regime in the SCSZ is retrieved at all the depths, while compression in the CVSZ and strike-slip in GCSZ are not well reproduced at any depth.

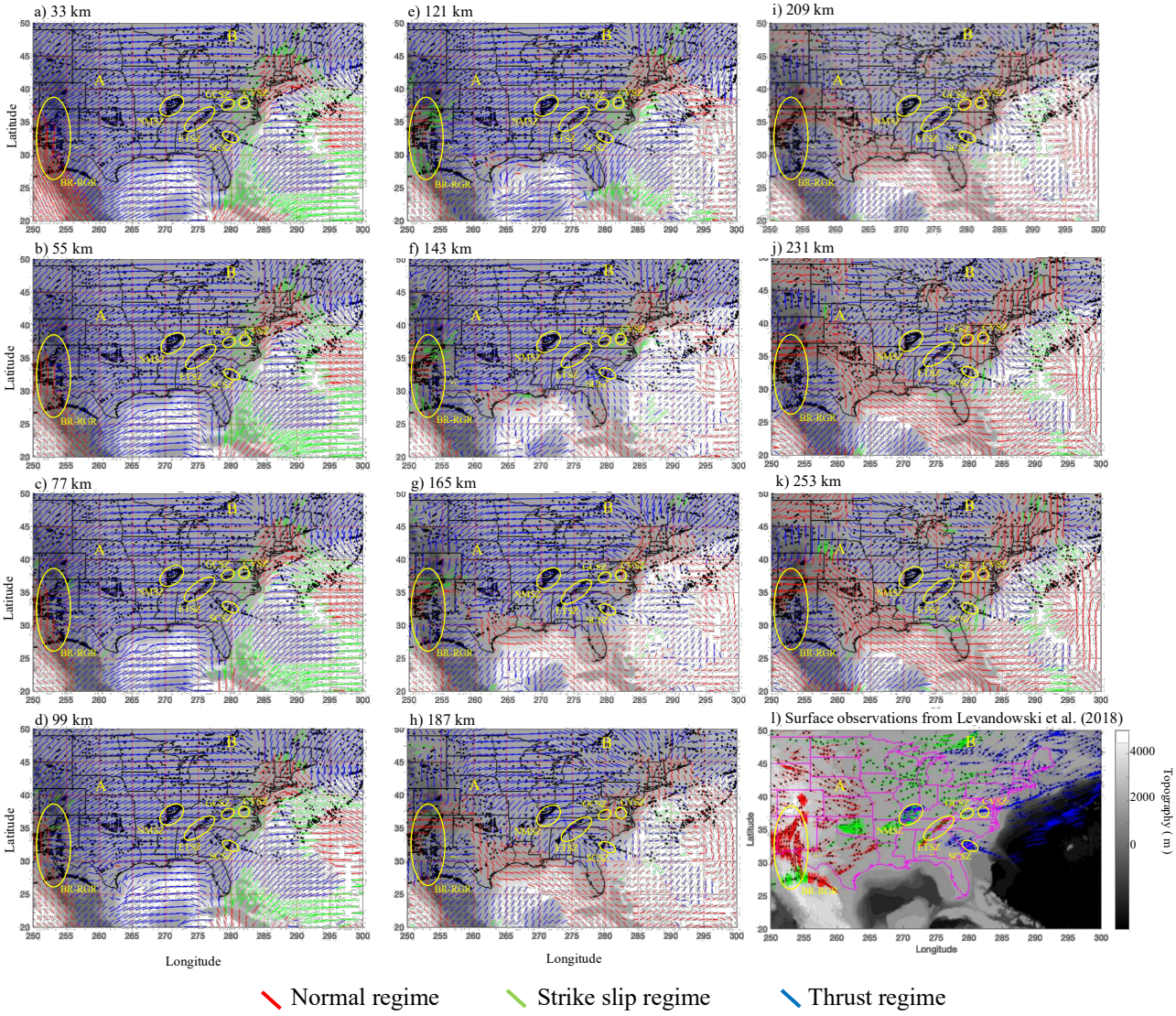

Figure 4.9: Same as Figure 4.3, for the TX2019slab tomography model (Lu et al., 2019).

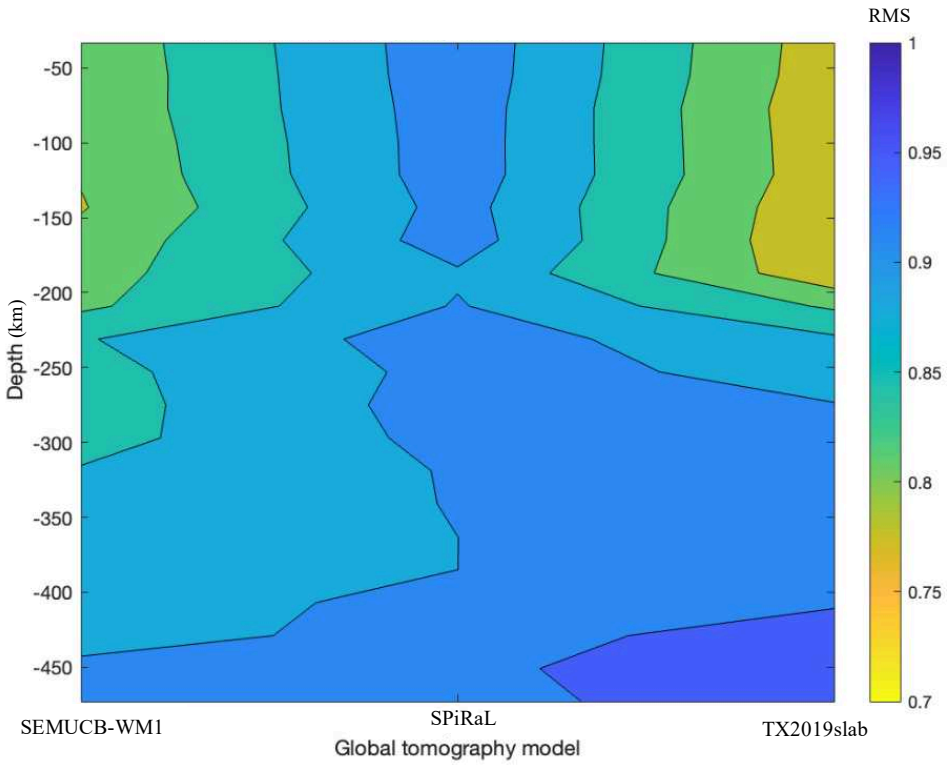

Figure 4.10: RMS (Root Mean Square) between the observed tectonic regimes, and the regimes modeled from the SEMUCB-WM1(French & Romanowicz, 2014), SPiRaL (Simmons et al., 2021) and TX2019slab (Lu et al., 2019) tomography models (see section 3.6 for the RMS computation description). The viscosity is depth dependent based on CAM2022 model (viscosity law $\eta_3(z)$, section 3.1) and the conversion factor between seismic velocity anomalies and density anomalies, $R_{\rho/vs}$ from Adam et al. (2021). Best fits are associated with an RMS~0.7 (yellow regions).

Figure 4.10 shows a map of computed RMS values for depths from 0 to 500 km, computed from the three global tomography models discussed above. The models use the same depth dependent viscosity (viscosity law $\eta_3(z)$, section 3.1), based on the CAM2022 lithosphere thickness (Priestley et al., 2024) and the same conversion factor between seismic velocity anomalies and density anomalies, $R_{\rho/vs}$, developed by Adam et al. (2021). At shallow depths (above 200 km), TX2019slab tomography model shows the smallest RMS value and the best fit to the surface observations.

4.1.2 Regional tomography models

We study the influence of regional tomography models using DNA13 (Porritt et al., 2014), CURSA2021 (Zhou et al., 2022), CSEM_North_America (Fichtner et al., 2018) and SATONA (Hua et al., 2025) tomography models. Similar to the previous global tomography model tests, we vary the input regional tomography model, and we keep all other parameters constant. Density anomalies outside the study area are set to zero. We have studied the influence of imposing the density values derived from the SEMUCB-WM1 global tomography in regions where the regional tomography models do not provide data. No significant difference has been found. Seismic velocity anomalies obtained from these regional tomography models are converted into density anomalies using the conversion factor, $R_{\rho/vs}$, derived by Adam et al. (2021). The viscosity is still the depth dependent viscosity where the lithosphere thickness is based on CAM2022 model (Priestley et al., 2024) (viscosity law $\eta_3(z)$, section 3.1).

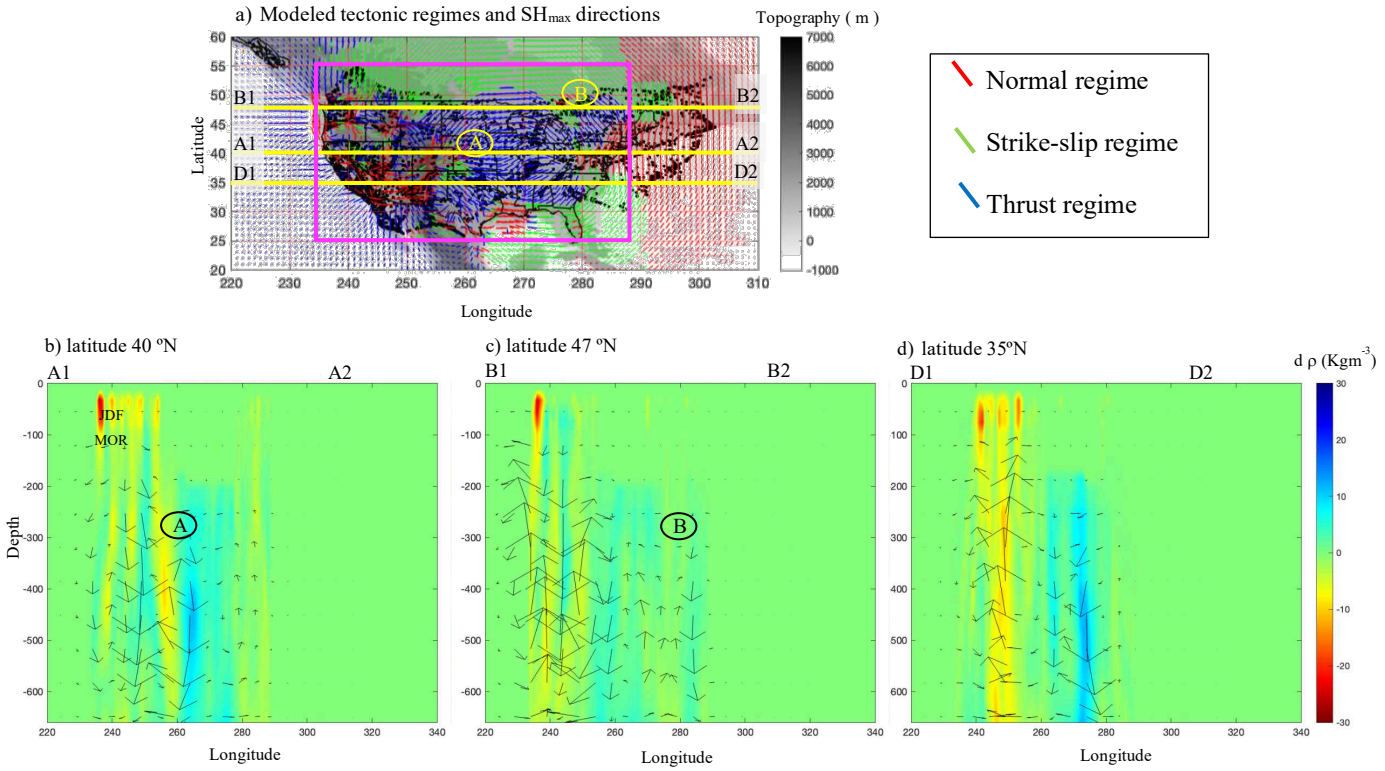

Figure 4.11: (a) Modeled tectonic regimes and SH_{max} directions computed with the DNA13 regional tomography model (Porritt et al., 2014) at 99 km depth. The model uses a depth dependent viscosity based on the CAM2022 lithosphere thickness (Priestley et al., 2024), (viscosity law $\eta_3(z)$, section 3.1), and the conversion factor between seismic velocity anomalies and density anomalies, $R_{\rho/vs}$, developed by Adam et al. (2021). Lines represent the direction of SH_{max}. Extension regimes are displayed in red, compression regimes in blue and strike slip in green. The gray map represents the topography (data from Tozer et al. (2019)) and black dots the seismicity (data from Levandowski et al. (2018)). Thin black lines mark the state boundaries. The lowermost panels display the instantaneous mantle flow at different latitude, (b) latitude 40ºN, (c) latitude 47ºN and (d) latitude 35ºN. Abbreviations used in the Figure 4.11b, JDF for the Juan de Fuca Plate and MOR for Mid Ocean Ridge. Arrows in the lower panel indicate the instantaneous flow induced by the density anomalies. Regions A and B are the upwelling zones indentified from the corresponding depth cross setions of the SEMUCB-WM1 global tomography model (Figure 4.1). The magenta box outlines the area covered by the regional tomography model data.

Figure 4.11 presents the mantle flow pattern, modeled tectonic regimes and SH_{max} directions computed with the DNA13 tomography model (Porritt et al., 2014) at 99 km depth. We only have the DNA13 regional tomography model data between the latitudes 25ºN and 55ºN and longitudes

234ºE and 288ºE as indicated by the box on Figure 4.11a. The modeled tectonic regimes (Figure 4.11a) indicates that most of the Central and Eastern U.S. is associated with a compressive regime whereas the Northern and as the Western part of the American continent are associated with strike slip and extensional regimes respectively. However, in contrast to previous global tomography model tests, the extension regions identified by the letters A and B, do not show clearly defined zones of either extensional and/or strike-slip. Note that the region B lies at the northernmost extremity of this regional tomography model. We do not expect the model output to be thorough near the borders. In the depth cross section along the profile A1A2 (Figure 4.11b), an upwelling can be seen near longitude 260°E. This creates an extension regime, on the western side of region A. We also observe an upwelling along the B1B2 profile, but it is located outside of CEUS. Along the profile D1D2 an upwelling is observed between longitude 240º and 260º. It creates the extension regime associated with the BR-RGR.

Moreover, as previous global tomography model tests, we study how the stress pattern changes with depth by considering depths between 33 km and 253 km. Figure 4.12 shows how the tectonic regimes change with the depth for models based on the DNA13 regional tomography model across the Central and Eastern United States (CEUS) with depth dependent viscosity based on lithosphere thickness CAM2022 model (viscosity law $\eta_3(z)$, section 3.1) and Adam et al. (2021) conversion factor.

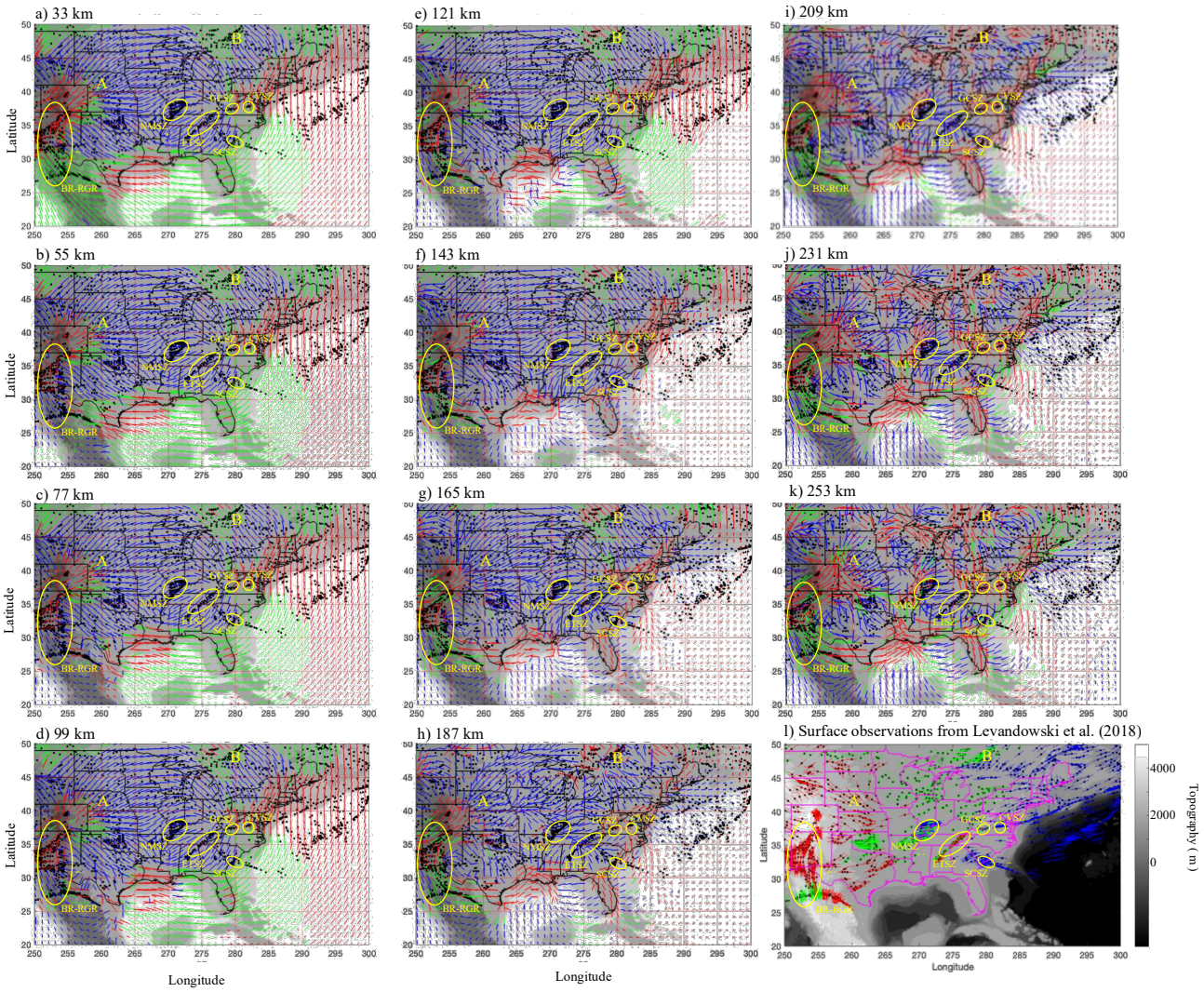

Figure 4.12: Variation of tectonic regimes with depth for the DNA13 tomography model (Porritt et al., 2014) across the Central and Eastern United States (CEUS). The viscosity is depth dependent based on CAM2022 model (viscosity law $\eta_3(z)$, section 3.1) and the $R_{\rho/vs}$ is from Adam et al. (2021). Circled areas are the Basin and Range - Rio Grande Rift (BR-RGR) and the major seismic zones, including New Madrid Seismic Zone (NMSZ), Eastern Tennessee Seismic Zone (ETSZ), South Carolina Seismic Zone (SCSZ), Giles County Seismic Zone (GCSZ) and Central Virginia Seismic Zone (CVSZ). Panels a-k: each panel shows the modeled tectonic regimes (see color scale legend) and the SH_{max} directions at depths reported on top of each panel. Black dots: seismicity from Levandowski et al. (2018). l) Surface observations taken from Levandowski et al. (2018). The black (a-k) and magenta (l) lines mark state boundaries (https://www.census.gov/geographies/mapping-files/time-series/geo/carto-boundary-file.html).

The modeled tectonic regimes and SH_{max} directions remain consistent over the CEUS for depths ranging from 33 km to 121 km, with compression in the CEUS center, surrounded by strike slip and extension regimes. At greater depths, the strike-slip regime disappears. The BR-RGR region shows a combination of extensional and strike-slip regimes at most depths except between 55 km to 99 km, where we model a combination of compressional and strike-slip regimes. At shallow depths, both the GCSZ and CVSZ show a mix of extensional and strike-slip regimes, whereas at depths greater than 121 km, they are characterized only by extensional regimes. In the model SCSZ is associated with strike-slip and compressional regimes up to 121 km. Deeper, we also find extension. Additionally, concerning the two extensional regions we noticed earlier, region A is shifted slightly to left while region B is not clearly defined, potentially because it is near the model's boundary.

Our model partially recovers the observed compression regimes in northeastern U.S and the extension over the BR-RGR region across most depths. However, the strike-slip regimes observed over BR-RGR is only recovered for shallow depths (33 km) and for depths greater than 121 km. Moreover, the strike-slip regimes observed over CEUS are generally not recovered. The compressional regime in the NMSZ is well retrieved at all the depths, whereas the extensional and strike-slip regimes in the ETSZ are not reproduced at any depth. For GCSZ we recover the observed strike-slip at shallow depths (33-99 km), while for SCSZ we partially reproduce the compressive regimes up to 143 km depth. In contrast, the observed compression in the CVSZ is not retrieved at any depth (Figure 4.12).

We also model the instantaneous mantle flow and the induced tectonic regimes with the CURSA2021 tomography model (Zhou et al., 2022). This model covers the area between latitudes 25ºN and 54.5ºN and longitudes 235ºand 294.5º (Figure 4.13). We use a depth dependent viscosity based on lithosphere thickness CAM2022 model (viscosity law $\eta_3(z)$, section 3.1) and the conversion factor between seismic velocity anomalies and density anomalies, $R_{\rho/vs}$, developed by Adam et al. (2021).

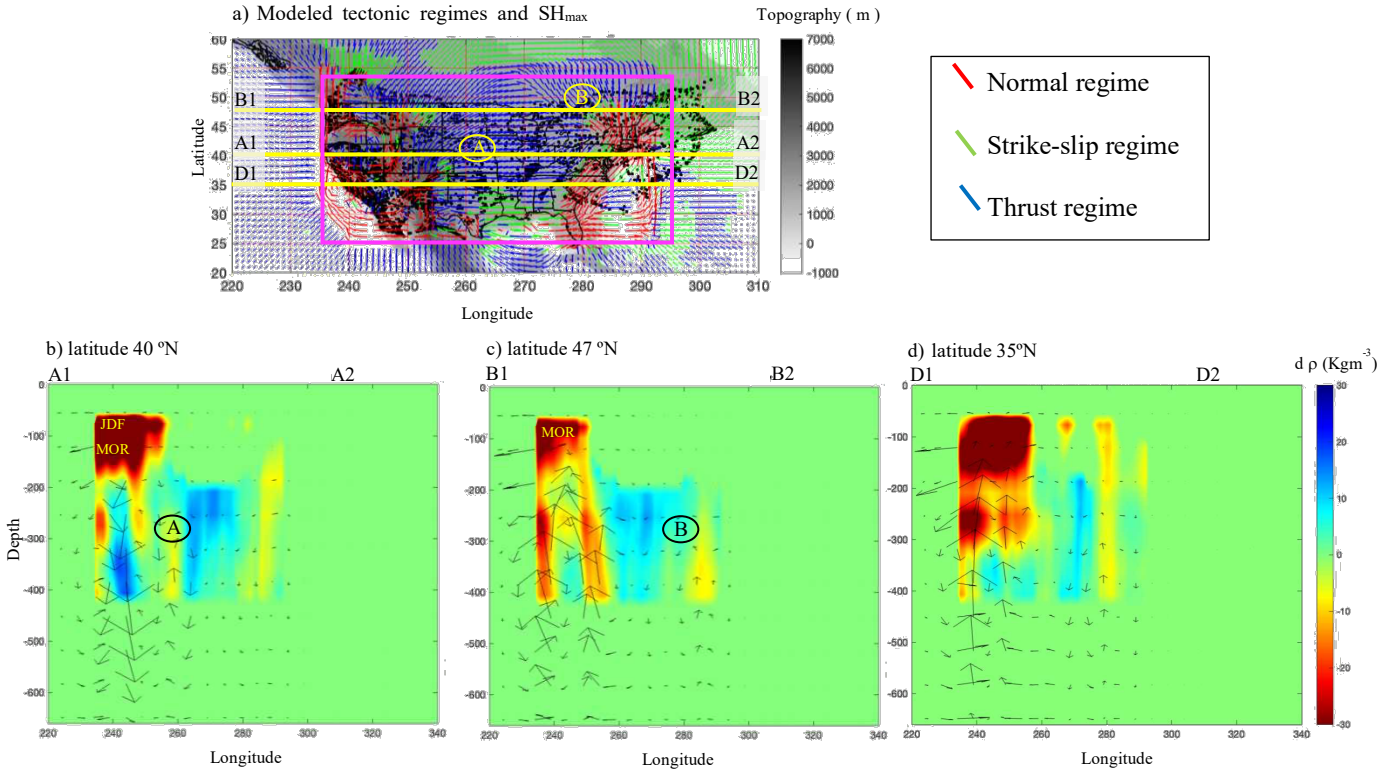

Figure 4.13: Same as Figure 4.11, for the CURSA2021 tomography model (Zhou et al., 2022). Regions A and B are the upwelling zones indentified from the corresponding depth crosssections of the SEMUCB-WM1 global tomography model (Figure 4.1).

In the modeled tectonic regime at 99 km depth (Figure 4.13a), most of the CEUS is characterized by compression regimes. The northernmost part of the American continent is dominated by strike slip regimes while the southern part contains extensions. Both these regions are near the model extremities, so these strike slip and extension regimes may be artifacts of the model set-up. In

contrast, the western U.S shows a mix of both extensional and compressional regimes whereas the eastern U.S is characterized by combination of strike-slip and extensional regimes. Extension and strike slip regimes are still observed in region B (more exactly southeast of region B) but not in region A. In the relevant depth cross section along the profile A1A2 (Figure 4.13b), a prominent upwelling associated with the region A at 260º longitude is observed. For the B extension region, which is identified earlier, a slightly shifted upwelling is visible along the profile B1B2 (Figure 4.13c). The upwelling observed along the D1D2 profile (Figure 4.13d) creates the extension regime modeled along the BR-RGR.

For the CURSA2021 tomography model also, we consider the variations of tectonic regimes at different depths while zooming in over CEUS (Figure 4.14). Until 165 km depth, most of the CEUS is compression with extension southeast of region B. The extension region has indeed been slightly shifted southeast when compared to modeled tectonic regimes with SEMUCB-WM1 global tomography model (Figure 4.1a). Moreover, we can see that for this model, the whole eastern coast is associated with an extensional regime, with SH_{max} parallel to the coast. The modeled tectonic regime is consistent up to 143 km depth. For greater depths, the pattern change. Moreover, extensional regime is present in BR-RGR region, CVSZ and SCSZ at most depths, while compressional regime can be seen in NMSZ and ETSZ up to 187 km depth and for greater depths, the NMSZ show extensional regime. The GCSZ show a mix of strike-slip and extensional regime at most depths.

The observed compressions in northeastern U.S and the N-S oriented extension in the BR-RGR region (Levandowski et al., 2018) are reproduced at most depths. The compressional regime in the

NMSZ is recovered up to 187 km depth and the strike-slip regimes in the GCSZ is partially reproduced between depths 33 km and 121 km. This model seems to reproduce the strike-slip regime observed southwest of NMSZ, unlike the previously discussed models. However, none of the observed compression regimes in SCSZ and CVSZ or extension and strike slip regimes in ETSZ are reproduced at any depth.

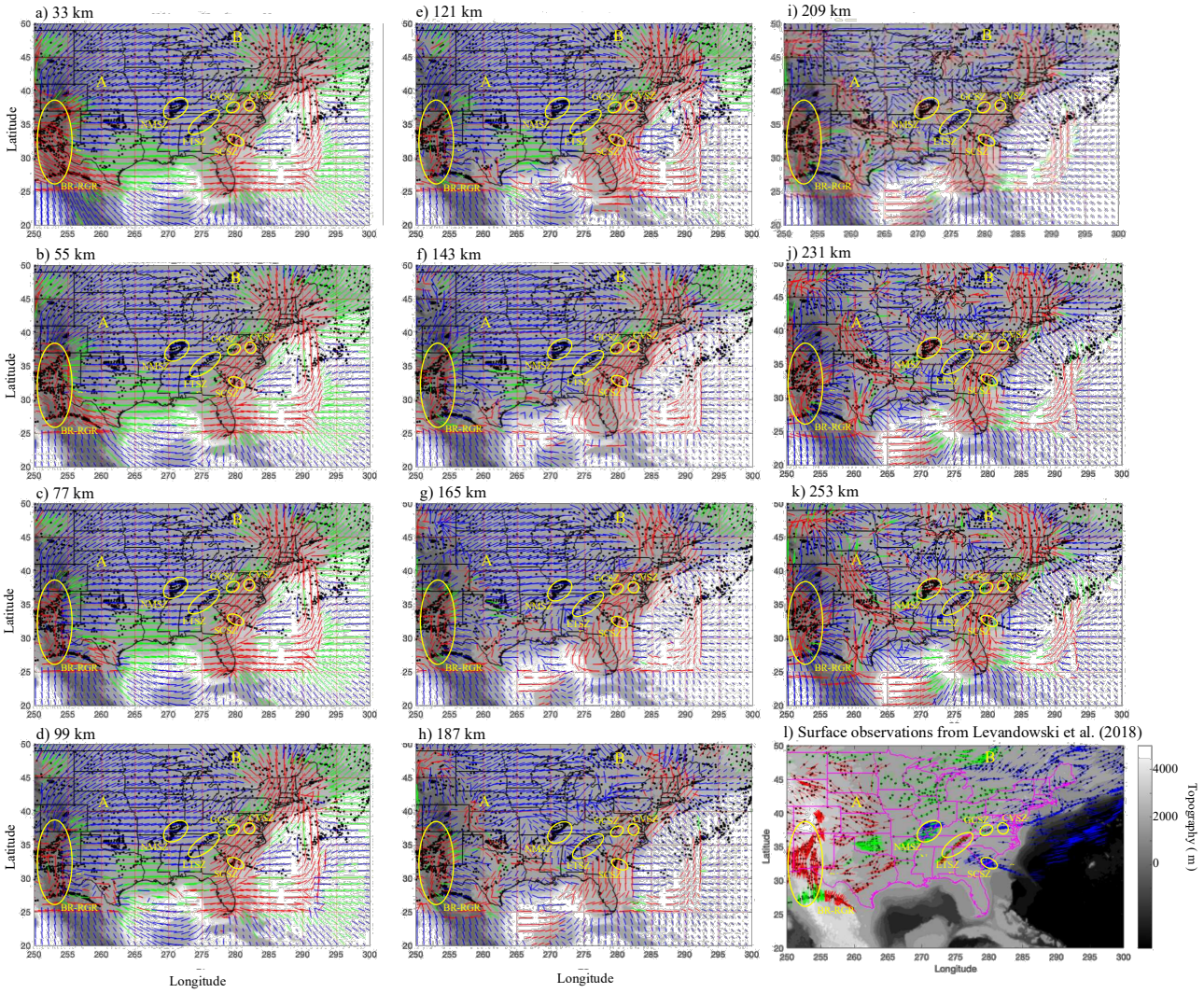

Figure 4.14: Same as Figure 4.12, for the CURSA2021 tomography model (Zhou et al., 2022).

The test is repeated using CSEM_North_America model (Fichtner et al., 2018), as shown in the Figure 4.15. This regional tomography model is confined to the region extending from latitudes 20ºN and 60ºN and longitudes 220º and 320º as shown in the magenta box (Figure 4.15a). The modeled tectonic regimes (Figure 4.15a) shows that CEUS and the northern U.S are characterized by compressional regimes. In contrast, the western and eastern U.S shows a mix of compressions, extensions and strike slip regimes. For this model, the extension previously seen in region A has disappeared, and the extension previously seen in region B has slightly shifted to the southeast. In the corresponding depth cross sections along the profiles A1A2 (Figure 4.15b) and B1B2 (Figure 4.15c), no significant upwellings are observed. In contrast, along the D1D2 profile (Figure 4.15d), two upwellings are visible. One potentially associated with the Bermuda region at longitude 290º and the other along the BR-RGR region between longitude 230º and 260º.

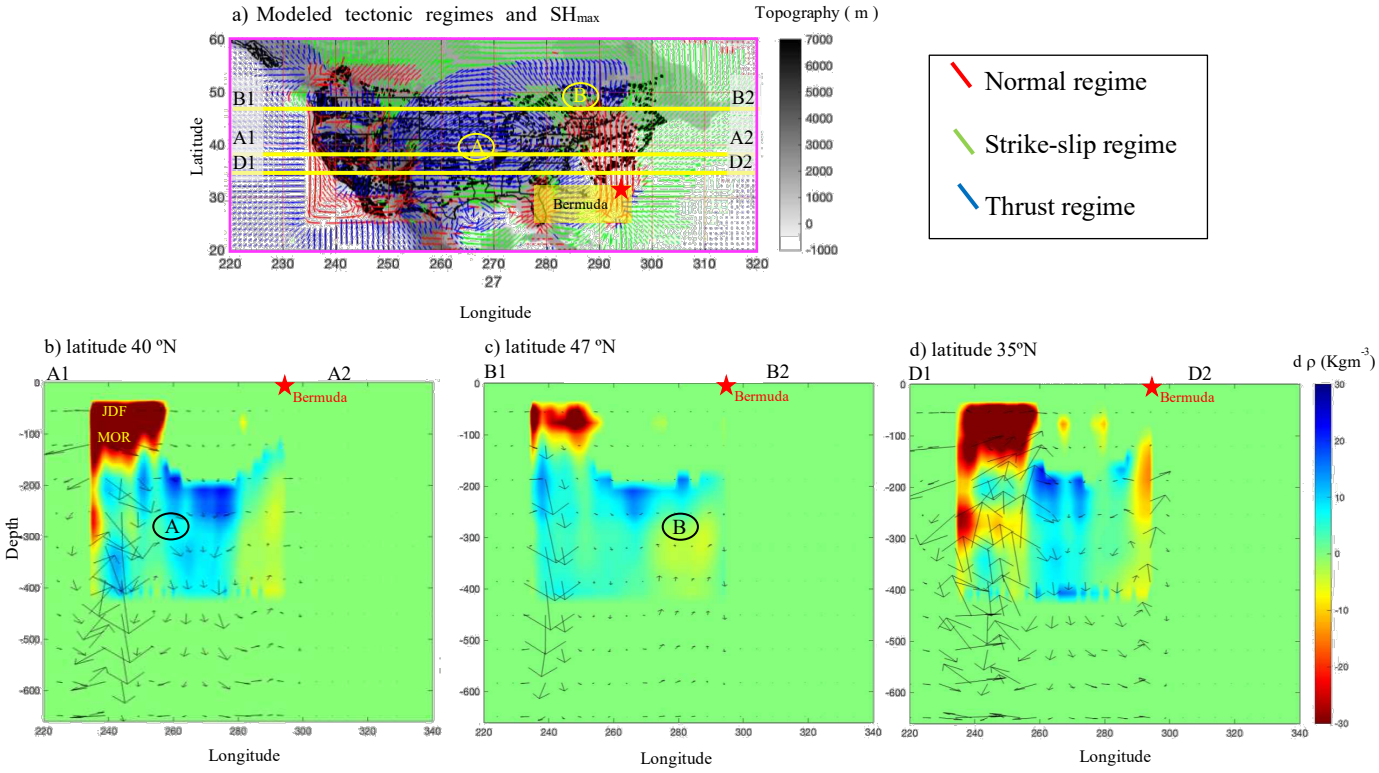

Figure 4.15: Same as Figure 4.11, for the CSEM_North_America model (Fichtner et al., 2018). Regions A and B are the upwelling zones indentified from the corresponding depth crosssections of the SEMUCB-WM1 global tomography model (Figure 4.1).

For CSEM_North_America model, the modeled tectonic regime pattern at different depths across the CEUS is analyzed in Figure 4.16. At shallow depths, CEUS is associated with compressional regimes. The BR-RGR region and the SCSZ display extensional regimes at all depths, whereas the NMSZ and ETSZ are characterized by compressional regime throughout the 33-187 km depth range. At shallow depths, the CVSZ shows a strike-slip regime, while GCSZ is characterized by a compressional regime.

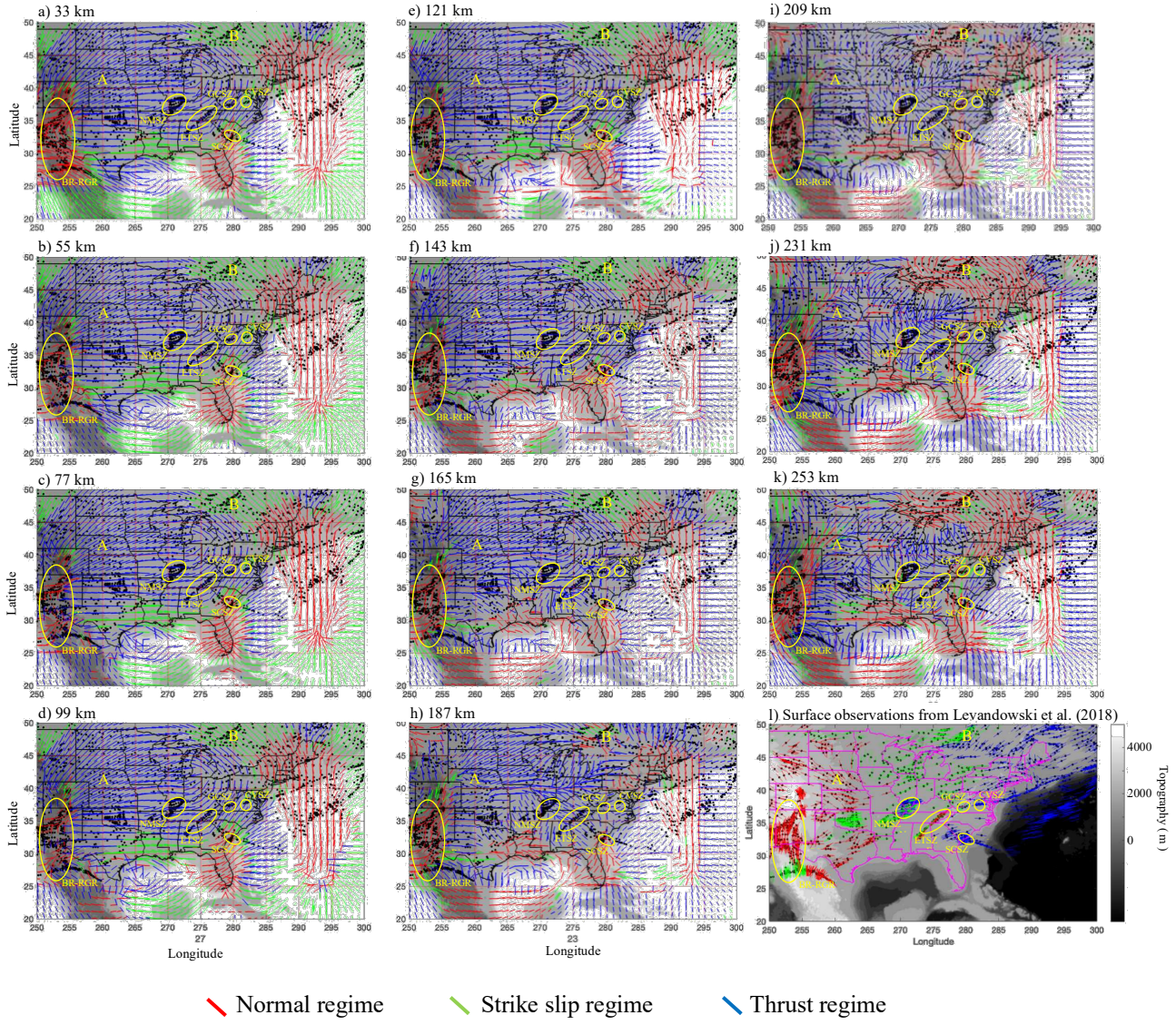

Figure 4.16: Same as Figure 4.3, for the CSEM_North_America model (Fichtner et al., 2018).

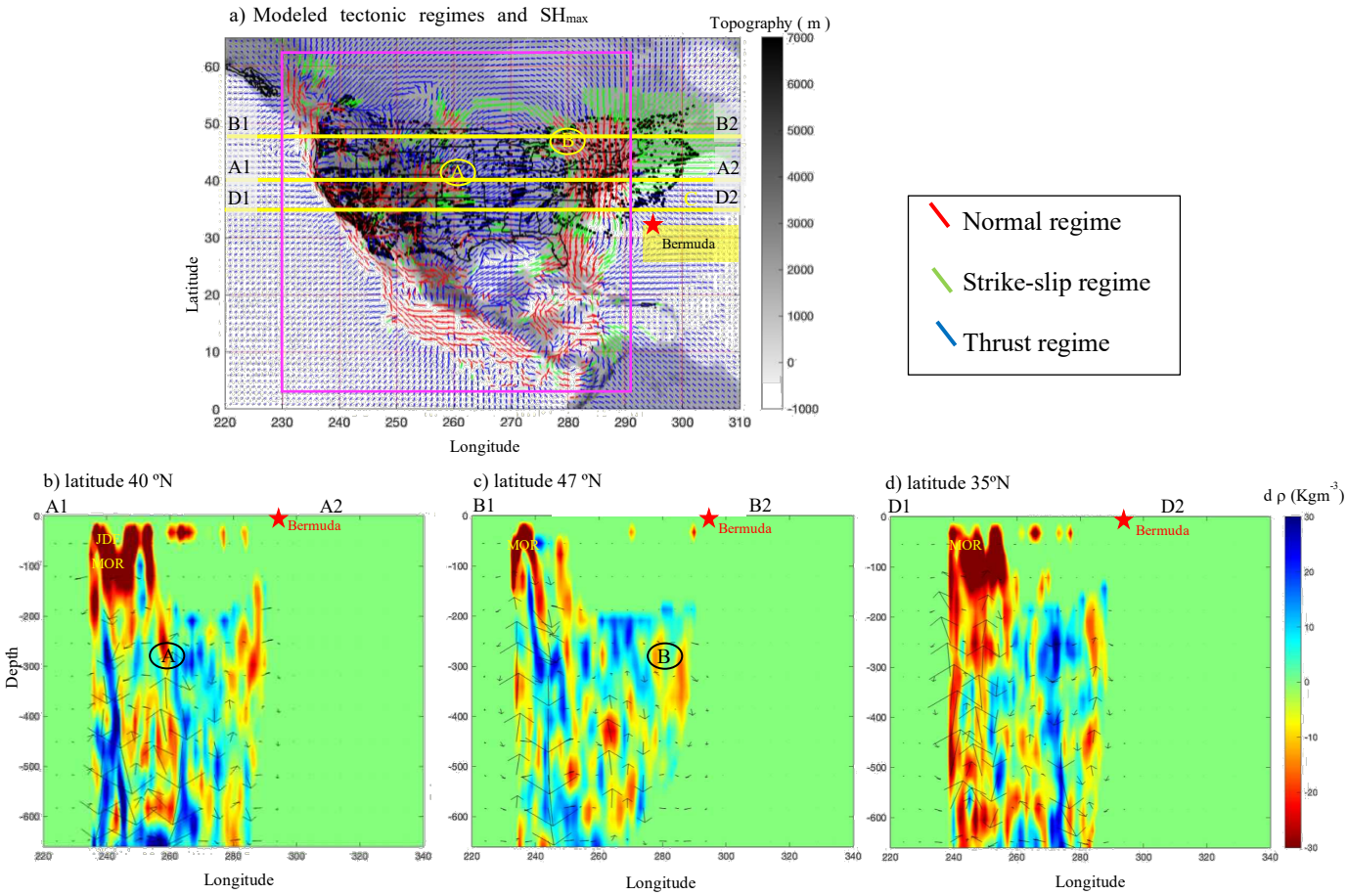

Figure 4.17: Same as Figure 4.1, for the SATONA tomography model (Hua et al., 2025). Regions A, B, anc C are the upwelling zones indentified from the corresponding depth crosssections of the SEMUCB-WM1 global tomography model (Figure 4.1).

The same analysis is conducted for the SATONA tomography model (Hua et al., 2025) (Figure 4.17). In the modeled tectonic regime (Figure 4.17a), CEUS is associated with compressional, extensional and strike slip regimes, whereas the western and eastern U.S exhibit a combination of extensional and strike-slip regimes. As observed in the CURSA2021 tomography model (Figure 4.13a), a similar pattern is seen in this model, where the entire eastern coast is characterized by extensional regimes with SH_{max} oriented parallel to the coastline. This may also be an artifact of the model setup, as this region is near the easternmost extremity of the tomography model. A and B extension regions are present, although both are slightly shifted. When considering the depth

cross sections, a prominent upwelling at 260º longitude related to the region A is observed along profile A1A2 (Figure 4.17b). A more widespread upwelling located between longitudes 260ºE and 280ºE is visible along profile B1B2 (Figure 4.17c). In addition, an upwelling that may be associated with the Bermuda is observed near longitude 280º along the D1D2 profile (Figure 4.17d).

A zoomed in view of the CEUS tectonic regime pattern at different depths for SATONA tomography model is shown in the Figure 4.18. From depths 33 km to 99 km, the BR-RGR region is dominated by extensional regimes. At depths greater than 99 km, this region becomes more complex, and we observed a mix of all the types of tectonic regimes. Up to 187 km depth, the ETSZ and NMSZ are characterized by compressional regimes, and deeper both zones become more complex, with here again a mix of several tectonic regimes. From 33 km to 121 km depth, the SCSZ exhibits strike-slip regimes and then include extensional regimes at greater depths. The CVSZ show extensional regimes at all depths, whereas the GCSZ present a combination of strike-slip and extensional regimes at shallow depths and beyond, compressional and extensional regimes can be seen.

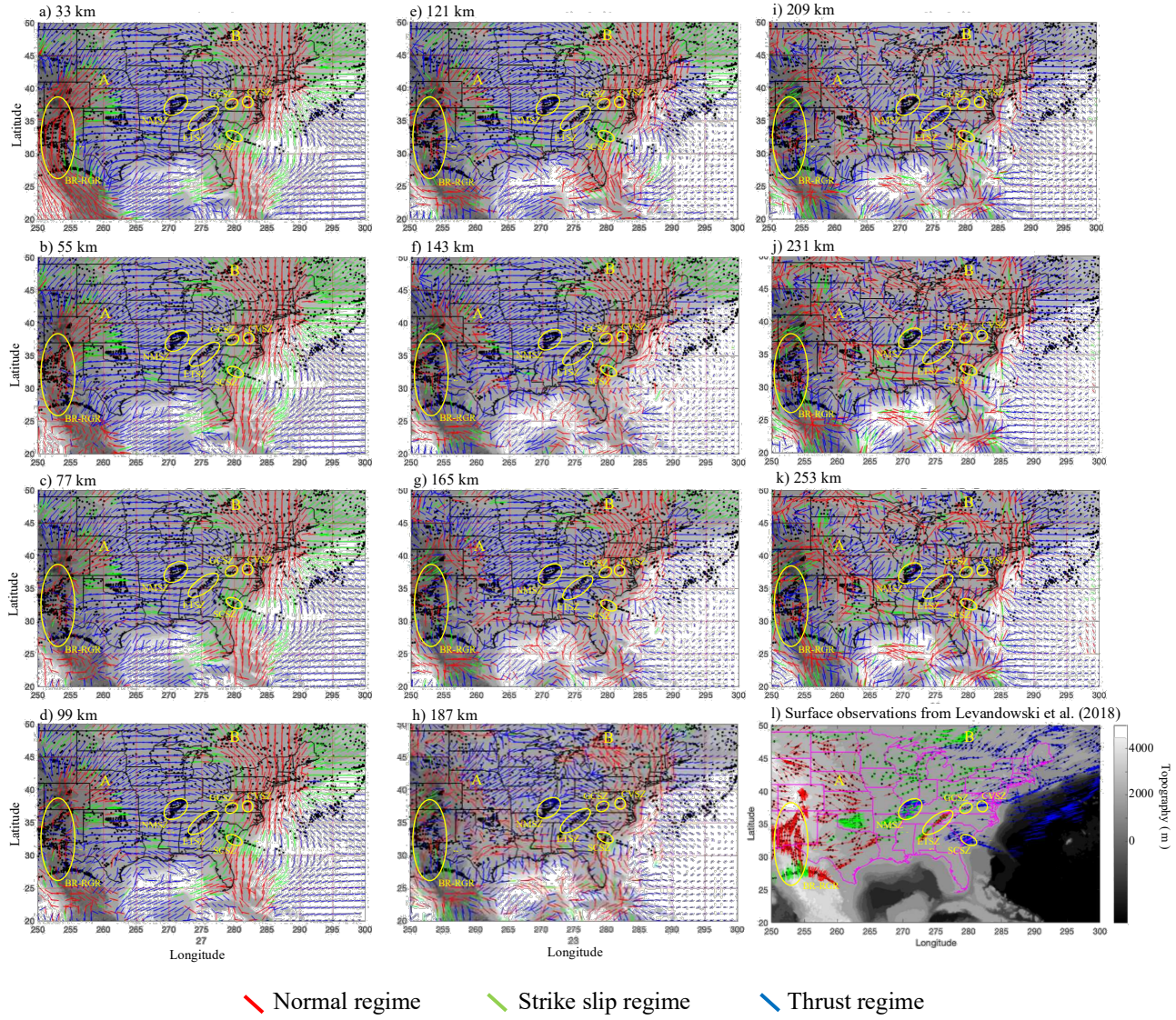

Figure 4.18: Same as Figure 4.2, for the SATONA tomography model (Hua et al., 2025).

Relative to the Levandowski et al. (2018) surface observations, the extensional regimes in the BR-RGR region and N-S SH_{max} direction at 33 km depth are well reproduced. The observed compressions in the northeastern U.S is reproduced partially at 121 - 253 km depths. The compressional regime in the NMSZ is consistently recovered across all depths, whereas the extensional regime in the ETSZ is seen only at 253 km depth. At 231 - 253 km depths, the model reproduces some of the strike-slip regimes in southwestern NMSZ and Oklahoma. Moreover, the

observed compressional and strike-slip regimes in the GCVS, as well as the compressional regimes in the SCSZ and CVSZ are not well reproduced at any depth.

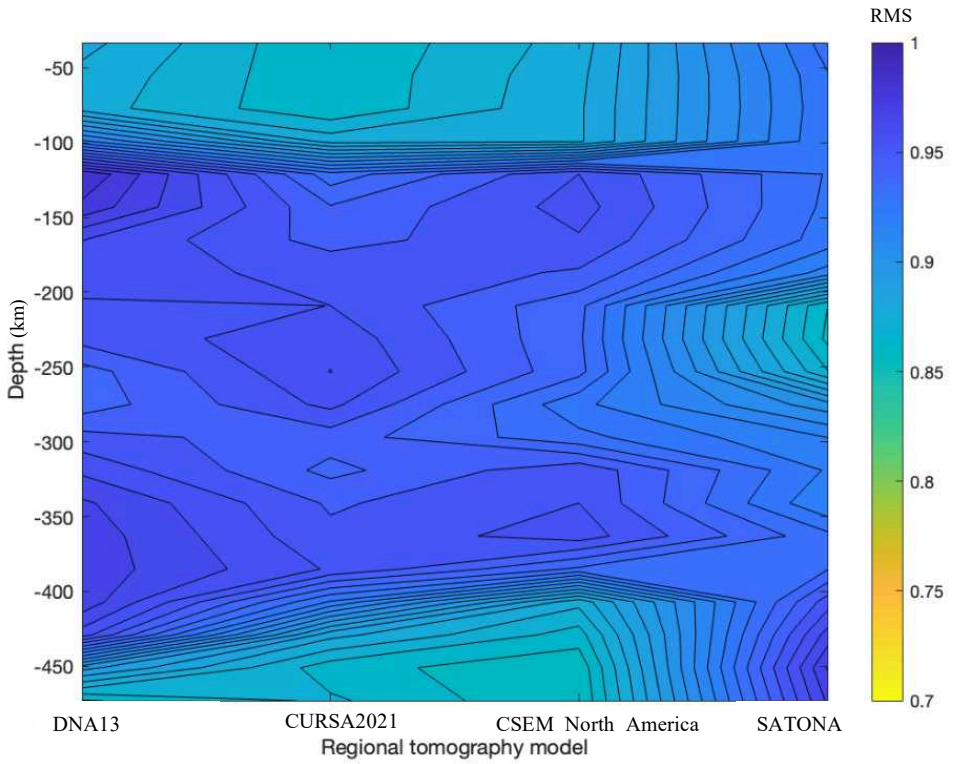

Figure 4.19: RMS (Root Mean Square) between the observed tectonic regimes, and the regimes modeled from the DNA13 (Porritt et al., 2014), CURSA2021 (Zhou et al., 2022), CSEM_North_America (Fichtner et al., 2018) and SATONA (Hua et al., 2025) regional tomography models (see section 3.6 for the RMS computation description). The viscosity is depth dependent based on CAM2022 model (viscosity law $\eta_3(z)$, section 3.1) and the conversion factor between seismic velocity anomalies and density anomalies, $R_{\rho/vs}$ from Adam et al. (2021). Best fits are associated with an RMS ~ 0.85 (cyan regions).

Figure 4.19 presents a map of computed RMS values between observed tectonic regimes, and the regimes modeled from regional tomography models for depths 0 to 500 km (y-axis), while along the x-axis we report the four regional tomography models discussed above. The models use the same depth dependent viscosity (viscosity law $\eta_3(z)$, section 3.1), based on the CAM2022 lithosphere thickness (Priestley et al., 2024) and the same conversion factor between seismic velocity anomalies and density anomalies, $R_{\rho/vs}$, developed by Adam et al. (2021). At shallow

depths (above 100 km), and at greater depths (below 400 km), DNA13, CURSA2021 and CSEM_North_America tomography models show the lowest RMS values among the models we considered, indicating comparatively better agreement with the surface observations. In contrast, the SATONA model has the lowest RMS values at depths 200- 250 km, suggesting a relatively better fit to the observations within this depth range.

When considering the regional tomography models, the difference between the RMS values is not significant. Given that the CAM2022 model indicates base of the lithosphere approximately 180 - 220 km (Priestley et al., 2024), SATONA model with depth dependent viscosity based on CAM2022 model (viscosity law $\eta_3(z)$, section 3.1) and conversion factor $R_{\rho/vs}$ from Adam et al. (2021), can be choose as our favorite regional tomography model. It shows the lowest RMS within this depth range.

Table 4.1: Modeled regimes over CEUS and other regions included in this study based on the studied global and regional tomography models using depth dependent viscosity based on CAM2022 model (viscosity law $\eta_3(z)$, section 3.1) and $R_{\rho/vs}$ from Adam et al. (2021). C, E and SS denote compression, extension and strike slip regimes respectively.

Regions	NE-US	BR-RGR	NMSZ	ETSZ	SCSZ	CVSZ	GCSZ
Observation	C	E	C/SS	E/SS	C	C	C/SS
			Global tomography models				
SEMUCB WM1 $R_{\rho/vs\text{-}Adam}$ $\eta 3(z)$	C partially all depths	E 33-77 km	C all depths	Do not converge	C 33-165 km	C all depths	C all depths
SPiRaL $R_{\rho/vs\text{-}Adam}$ $\eta 3(z)$	C all depths	E partially 33-77km	C all depths	E partially 209-231 km	C all depths	Do not converge	SS 33-143 km
TX2019slab $R_{\rho/vs\text{-}Adam}$ $\eta 3(z)$	C all depths	E 33-77 km	C all depths	Do not converge	C all depths	Do not converge	C 33-165 km
			Regional tomography models				
DNA13 $R_{\rho/vs\text{-}Adam}$ $\eta 3(z)$	C partially all depths	E partially all depths	C all depths	Do not converge	C partially 33-143 km	Do not converge	SS partially 33-99 km
CURSA2021 $R_{\rho/vs\text{-}Adam}$ $\eta 3(z)$	C partially all depths	E partially all depths	C 33-187 km	Do not converge	Do not converge	Do not converge	SS partially 33-121 km
CSEM_North_America $R_{\rho/vs\text{-}Adam}$ $\eta 3(z)$	C partially all depths	E partially all depths	C all depths SS partially 253 km	Do not converge	Do not converge	C 99-231 km	C all depths SS partially 253 km
SATONA $R_{\rho/vs\text{-}Adam}$ $\eta 3(z)$	C partially 121-253 km	E 33 km partially 55-253 km	C all depths SS partially 231-253 km	E partially 253 km	Do not converge	Do not converge	Do not converge

Table 4.1 summarizes the observed and modeled tectonic regimes for the major CEUS seismic zones obtained from each global and regional tomography model as an overall comparison with the surface observations from Levandowski et al. (2018).

4.2 Influence of the viscosity

We study the influence of viscosity, including and weak plate boundary (WPB hereafter) on the modeled tectonic regimes using SEMUCB-WM1 global tomography model (French & Romanowicz, 2014). Seismic velocity anomalies provided by the tomography model are converted into density anomalies using the conversion factor, $R_{\rho/vs}$, derived by Adam et al. (2021). We consider several viscosity laws including constant viscosity($\eta_1(z)$), depth dependent viscosity with 100 km thick lithosphere ($\eta_2(z)$), depth dependent viscosity where the lithosphere thickness is based on CAM2022 model (Priestley et al., 2024) ($\eta_3(z)$), temperature dependent viscosity ($\eta_4(T)$) and temperature and depth dependent viscosity ($\eta_5(T)$) (section 3.1). Additionally, we study the modeled tectonic regime pattern by imposing a viscosity drop along the plate margin (WPB) with depth ($\eta_6(z)$) and temperature ($\eta_7(T)$) dependent viscosities.

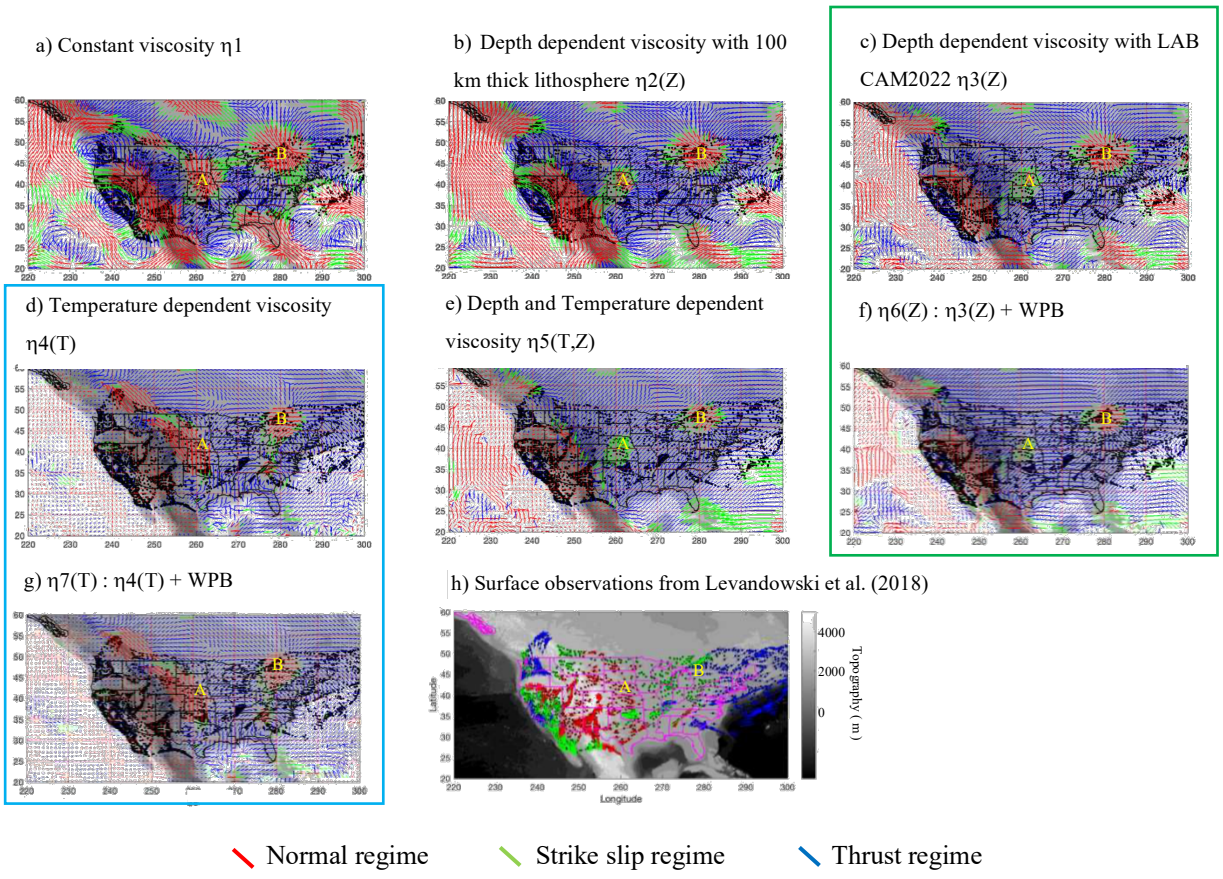

Figure 4.20: Modeled tectonic regimes with different viscosity laws discussed in section 3.1 using SEMUCB-WM1 tomography model (French & Romanowicz, 2014), (a) constant viscosity(η_1), (b) depth dependent viscosity with 100 km thick lithosphere($\eta_2(Z)$), (c) depth dependent viscosity with LAB CAM2022($\eta_3(Z)$), (d) temperature dependent viscosity($\eta_4(T)$), (e) depth and temperature dependent viscosity ($\eta_5(T,Z)$), (f) depth dependent viscosity with WPB ($\eta_6(Z)$) and (g) temperature dependent viscosity with WPB ($\eta_7(T)$) at 77 km depth. The conversion factor between seismic velocity anomalies and density anomalies, $R_{\rho/vs}$ is from Adam et al. (2021). h) Surface observations taken from Levandowski et al. (2018). The gray map represents the topography (data from Tozer et al. (2019)) and black dots the seismicity (data from Levandowski et al. (2018)). The black (a-g) and magenta (h) lines mark state boundaries (https://www.census.gov/geographies/mapping-files/time-series/geo/carto-boundary-file.html). Regions A and B are the extensional zones associated with upwellings seen in the depth cross-sections of the SEMUCB-WM1 tomography model (Figure 4.1). The green and blue boxes indicate the modeled tectonic regimes for models with (f, g) and without WPB (c,d) for $\eta_3(Z)$ and $\eta_4(T)$ respectively.

Figure 4.20 shows the modeled tectonic regimes at 77 km depth using different viscosity laws described in section 3.1. The modeled tectonic regimes at 99 km depth are shown in Figure 4.21.

Generally, the modeled tectonic regime pattern varies considerably with the applied viscosity law, showing the strong influence on the modeled tectonic regimes and SH_{max} direction. However, compressional regime remains dominant over most of CEUS in all models. Furthermore, the A and B extension regions previously identified in the SEMUCB-WM1 model (Figure 4.1a), are generally present, although the area and the associated tectonic regimes and SH_{max} orientations vary with the considered viscosity laws.

The first three models which use the depth dependent viscosity laws η1, η2(Z), and η3(Z), show a similar tectonic regime pattern within the lithosphere (Figure 4.20a-c). However, at the base of the lithosphere or at greater depths, the pattern changes (Figure 4.21a-c). Observe for example the difference between Figures 4.20b and 4.21b, where we impose the base of the lithosphere at 99 km. At depths 99 km or greater, the strike-slip regimes are observed are no longer observed and the SH_{max} direction also changes (Figures 4.20b, 4.21b).

The viscosity laws η3(Z), η4(T) and η5(T,Z) represents depth dependent viscosity, temperature dependent viscosity and depth and temperature dependent viscosity models respectively. At 77 km, in the η4(T) model, the extension along the region extends farther northwest than in the other two models and exhibits N-S SH_{max} directions, whereas other two models show NE-SW orientation (Figure 4.20 c-e). The extension along the B region is also seen in all the three models, but its extent and SH_{max} direction differ. At depth 99 km or deeper, the pattern changes for the model using the η4(T) viscosity (Figure 4.20 d, Figure 4.21 d). The extension along the region A disappears and the extent of the normal regime along the region B is smaller. The modelled pattern

remains very similar for the models using the η3(Z), and η5(T,Z) viscosities (Figure 4.20c,e, Figure 4.21c,e).

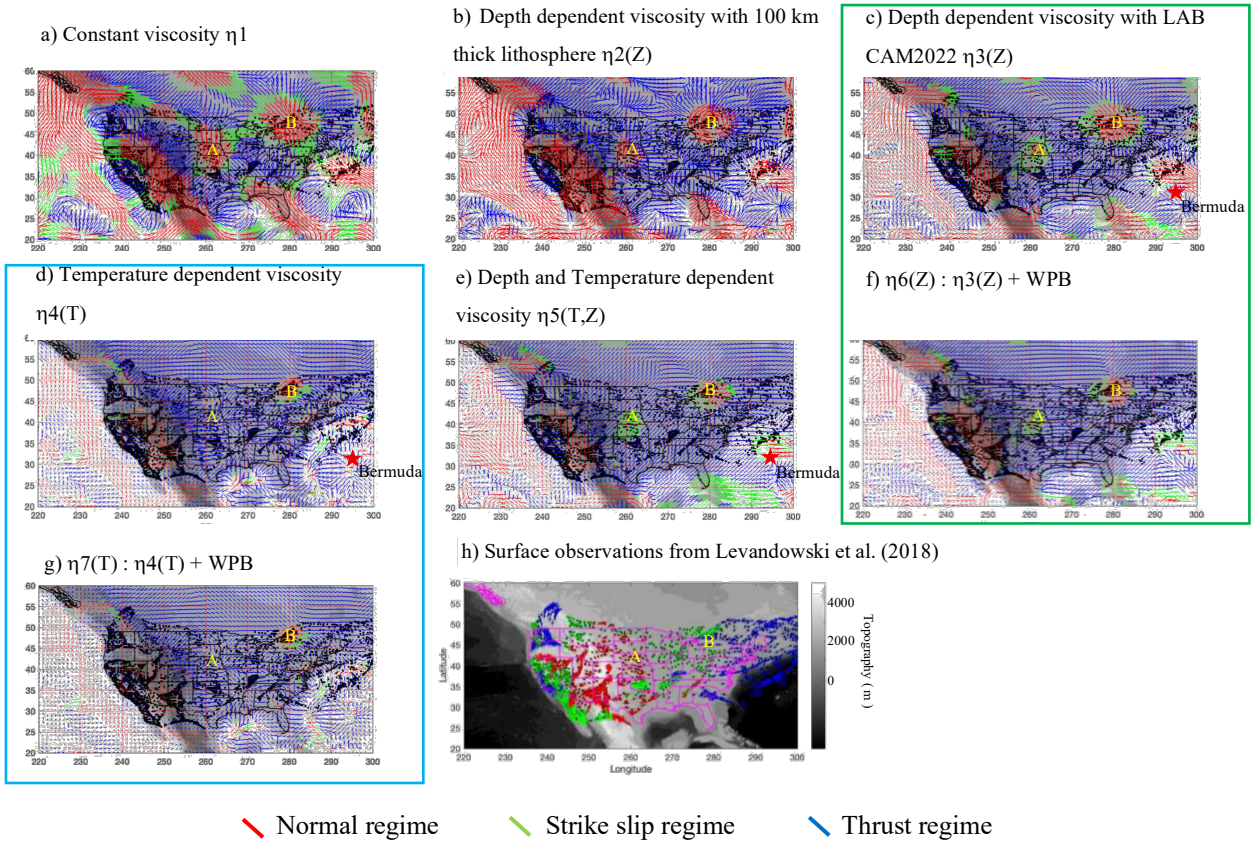

Figure 4.21: Same as Figure 4.21, i.e., modeled tectonic regimes but at 99 km depth. The red star indicates the location of Bermuda.

The η6(Z) and η7(T) models implement WPB, i.e., we impose a viscosity drop at lithospheric plate's margins. The green and blue boxes in the Figures 4.20 and 4.21 compare the models with and without WPB for models η3(Z) and η4(T) respectively. Implementing WPB when using a temperature dependent viscosity, η4(T), does not considerably change the modeled tectonic regimes and SH_{max} direction (Figures 4.20d,g, 4.21d,g). While considering the η3(Z) viscosity, the integration of WPB reduces the extent of the extension regimes found in B and Bermuda regions and strike-slip regimes in A region (Figures 4.20c,f, 4.21c,f).

Based on this discussion, we conclude that varying the viscosity (including WPB implementation) has an important effect on the modeled tectonic regimes and SH_{max} orientation.

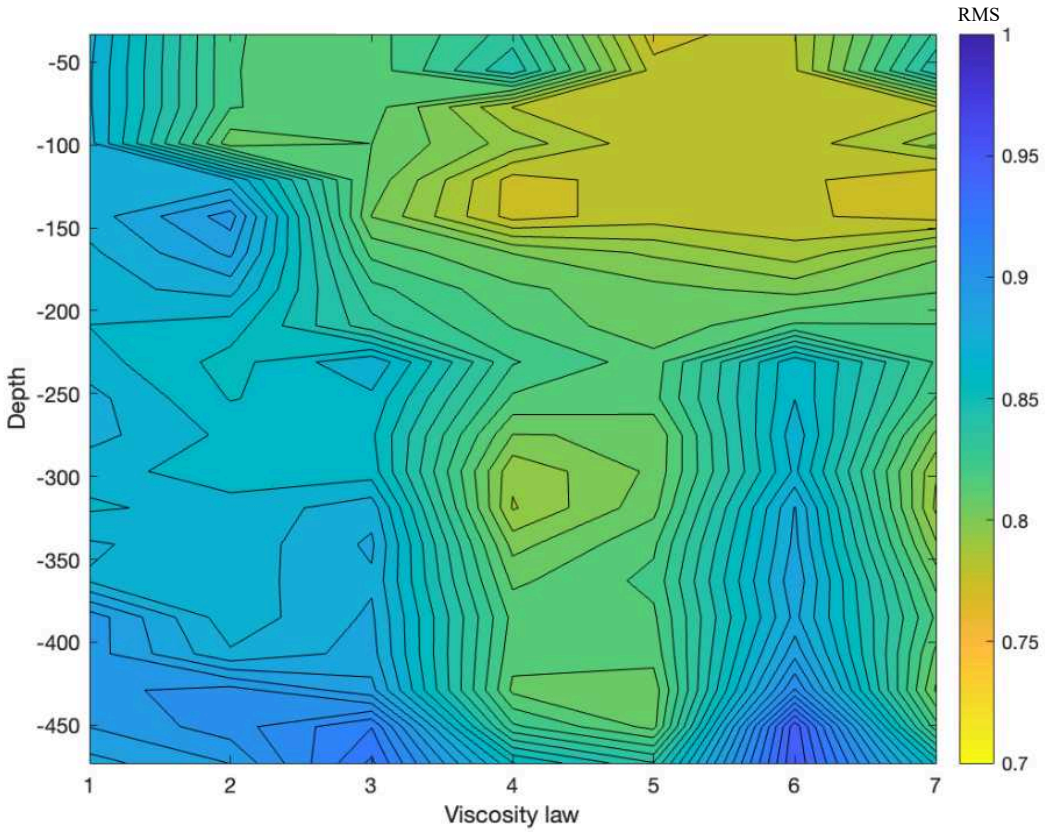

Figure 4.22: RMS (Root Mean Square) between the observed tectonic regimes and the modeled tectonic regimes using the viscosity laws discussed in section 3.1 using SEMUCB-WM1 tomography model (French & Romanowicz, 2014). The conversion factor between seismic velocity anomalies and density anomalies, $R_{\rho/vs}$ from Adam et al. (2021). Best fits are associated with an RMS ~ 0.75 (yellow regions).

Figure 4.22 show the computed RMS map between observed tectonic regimes and modeled tectonic regimes using the viscosity models discussed above. All the models use the same conversion factor by Adam et al. (2021) and SEMUCB-WM1 tomography model. The η4(T) and η7(T) models exhibit least RMS values between 100-150 km, implying consistency with the surface observations within this depth range. However, the η5(T,Z) model yields the lowest RMS values at depth 0-50 km, suggesting relatively the best fit model at the shallow depths.

4.3 Conversion factors

4.3.1 Conversion factors from previous studies

Seismic velocity anomalies obtained from tomography models are generally converted into density anomalies using a conversion factor $R_{\rho/vs}$ (section 3.3). We study the influence of these conversion factors. These tests use the SEMUCB-WM1 global tomography model and the depth dependent viscosity where the lithosphere thickness is taken from the CAM2022 model (Priestley et al., 2024) (viscosity law $\eta_3(Z)$, section 3.1). Some of the most recent conversion factors, such as the ones proposed by Steinberger and Calderwood (2006), Karato (2008), Simmons et al. (2009), Lee et al. (2011) and Adam et al. (2021) are considered in this study.

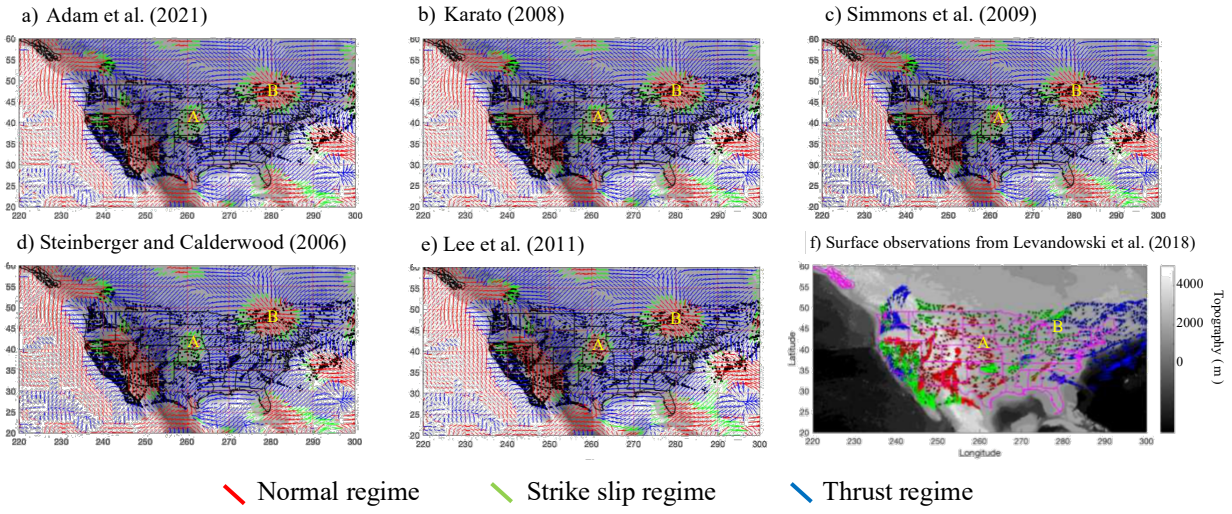

Figure 4.23: Variation of modeled tectonic regimes using different conversion factors between seismic velocity anomalies and density anomalies, $R_{\rho/vs}$, (a) Adam et al. (2021), (b) Karato (2008), (c) Simmons et al. (2009), (d) Steinberger and Calderwood (2006) and (e) Lee et al. (2011) with SEMUCB-WM1 tomography model (French & Romanowicz, 2014) at 99 km depth. The viscosity is depth dependent based on CAM2022 model (viscosity law $\eta_3(Z)$, section 3.1). The gray map represents the topography (data from Tozer et al. (2019)) and black dots the seismicity (data from Levandowski et al. (2018)). f) Surface observations taken from Levandowski et al. (2018). The black(a-e) and magenta(f) lines mark state boundaries (https://www.census.gov/geographies/mapping-files/time-series/geo/carto-boundary-file.html). Regions A and B correspond to the extensional zones associated with upwellings seen in the depth crosssections of the SEMUCB-WM1 tomography model (Figure 4.1).

Figure 4.23 shows the modeled tectonic regimes at 99 km depth using these different conversion factors. Overall, the tectonic regime patterns are similar for all conversion factor models, with CEUS mainly characterized by compression and two extensional regions A and B. However, a few minor differences are present. For instance, in the model using the Lee et al. (2011) conversion factor (Figure 4.24e), strike slip regimes occur at approximately 265ºE, 23ºN (Western Gulf of Mexico) and 290ºE, 28ºN (Western North Atlantic Ocean) whereas, compression regime is observed in other models. In addition, the extensional regimes in the A region extend farther, reaching northern Oklahoma. These differences are however minor and we conclude that $R_{\rho/vs}$ variations have surprisingly little influence on the modeled tectonic regimes and SH_{max}. Although not showed here, the models display patterns, similar with each other at each depth.

4.3.2 Conversion factor including an elastic model

The conversion factor between seismic velocity anomalies and density anomalies, $R_{\rho/v}$ we discussed in the section 3.3 can also be written as

$$R_{\rho/v} = -\frac{\alpha}{A_{VT}} \tag{10}$$

where α is the coefficient of expansion interpolated along the 1600 K adiabat (Karato, 2008) and A_{VT} is the seismic velocity temperature derivative. It accounts for both elastic (A_{VT_el}) and anelastic (A_{VT_an}) components (Karato, 2008).

The Adam et al. (2021) conversion factor include both elastic and anelastic components. However, the anelastic component varies only with depth. To study the influence of 3D anelastic variations, we use the anelastic component with the QsASR17 3D anelastic model developed by Debayle et al. (2020). QsASR17 model allows the anelastic component to vary spatially with longitude, latitude and depth.

This test is performed using the SEMUCB-WM1 tomography model (French & Romanowicz, 2014) while keeping all other parameters unchanged. We still observe the A and B extension regions discussed earlier with compression regime remains across the CEUS. However, incorporating 3D anelastic component do not produce a significant change in the modeled tectonic regime patterns at any depth (Figure 4.24).

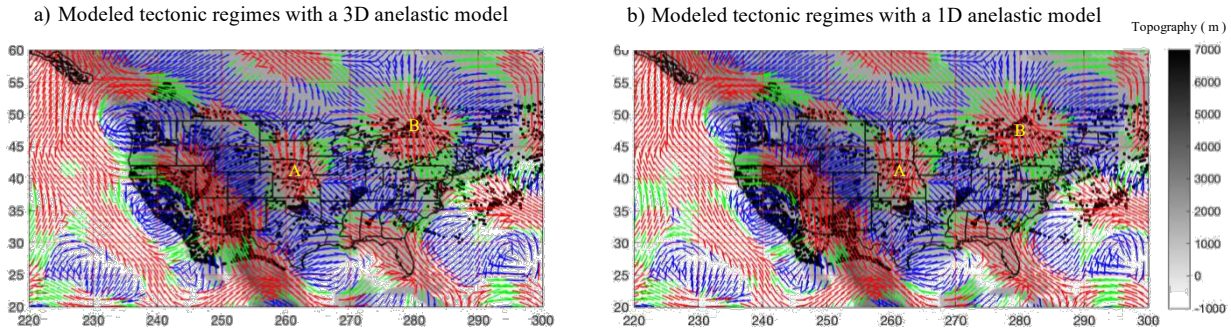

Figure 4.24: Modeled tectonic regimes with a 3D anelastic model (a) and with a 1D anelastic model (i.e., $R_{\rho/v}$ from Adam et al. (2021)) (b). The 3D anelastic component is from Debayle et al. (2020), and we use the SEMUCB-WM1 tomography model and constant viscosity (viscosity law η_1, section 3.1) at 99 km depth.

Chapter 5 - Discussion

We examine the role of mantle dynamics on intraplate seismicity along the Central and Eastern United States (CEUS). The instantaneous mantle flow is computed using the density anomalies derived from seismic velocity anomalies obtained from tomography models. We test the sensitivity of model parameters by varying each model parameter individually including tomography models, viscosity laws and conversion factor between seismic velocity anomalies and density anomalies, $R_{\rho/vs}$. Using the modeled convection velocities, we compute the stress tensor and derive the tectonic regimes and the maximal shear direction, SH_{max}, induced by the instantaneous mantle flow. We then compare the modeled tectonic regimes and SH_{max} with the surface observations inferred from earthquake focal mechanisms. This allows us to identify areas where the mantle dynamics may account for the observed intraplate seismicity.

5.1 Sensitivity of model parameters

5.1.1 Tomography models

In this study, we compare several tomography models with the idea that features appearing consistently across the models are more likely to reflect the real features of Earth structure. Based on this, we focus on the agreements and differences among the model results.

Among the tested global models, the TX2019slab tomography model (Lu et al., 2019) used with the $R_{\rho/vs}$ from Adam et al. (2021) and the depth dependent viscosity based on CAM2022 (viscosity law $\eta_3(z)$, section 3.1) reproduces most of the observed tectonic regimes over CEUS and other study regions. It also shows the lowest RMS value between the observed and the modeled tectonic regimes with an RMS value of approximately 0.7 (Figure 5.4).

Despite the differences in the modeled tectonic regimes, several tectonic regimes are consistently recovered with all the considered global tomography models. All models reproduce compressional regimes in the northeastern U.S, NMSZ and SCSZ, as well as extension regimes in BR-RGR at depths shallower than 99 km together with the observed SH_{max} orientation. However, at greater depths, most models continue to reproduce extension regimes in BR-RGR although with varying SH_{max} directions. In addition, all models reproduce the B extension region previously identified with the SEMUCB-WM1 global tomography model, although it has slightly shifted eastward when using the SPiRaL and TX2019slab tomography models (Figure 5.1). Several models show extension regimes along the A region identified with the SEMUCB-WM1 global tomography model. The depth cross sections show clear mantle upwellings beneath BR-RGR, region A and region B in most of the tomography models (Figure 5.1d-f; Figure 4.1b, c; Figure 4.4b, c; Figure 4.7b, c). Although their exact location varies slightly between models, these upwellings are present in all the global tomography models considered in this study. Most of the time, these upwellings induce extensional regimes at shallow depths (0-99 km, or roughly in the lithosphere). Note that the extensional regimes modeled along region A and BR-RGR are observed in the focal mechanisms. The focal mechanisms do not show extension along region B. The compressional regimes are modeled for region B with some of the viscosity laws (For TX2019 slab model with depth dependent viscosity laws (Appendix Figure 1) and SPiRaL and SEMUCB-WM1 model with temperature dependent viscosity laws, (Appendix Figure 2 and 3). Note that even for these models (i.e., for models that do not induce an extension regime along regions B), we still have an upwelling under region B.

A few of the tectonic regimes derived from focal mechanisms are not reproduced by any of the models. For example, strike slip regimes in the NMSZ, as well as extension and strike slip regimes in the ETSZ are generally nor reproduced. More precisely, the extension regimes along the ETSZ are only reproduced deep in the mantle (depths 209 -231 km, Figure 4.6) using the SPiRaL tomography model (Simmons et al., 2021). This suggests that the observed extension in the ETSZ may be created by shallower phenomena rather than mantle dynamics.

The tectonic regimes in the ETSZ have interpreted differently in previous studies. Some authors suggest strike-slip regime (Mazzotti & Townend 2010; Powell & Thomas 2016) which is consistent with the results of Saxena et al. (2021). In contrast, other studies have reported extensional regimes in the ETSZ including Levandowski et al. (2018), the dataset used for the surface observations in this study. We have met with Will Levandowski at the 2025 AGU meeting and have asked him if the extension he obtains along the ETSZ may be an artifact of the considered database or the data processing. He said that his newer results (Levandowski, 2026) confirm the extension regimes along the ETSZ. These may be created by shallower phenomena.

Biryol et al. (2016) identified positive velocity anomalies in the upper mantle between the ETSZ and NMSZ at depths of 200 to 660 km and interpreted them as foundering lithosphere. Later Saxena et al. (2021) evaluated the performance of Biryol et al. (2016) model using four different tomography models, including DNA13 model and also observed high velocity anomalies at similar depths. In our modeled results, the global and regional tomography models similarly show positive density anomalies and downwelling flow at the same depth range in the same region (Appendix Figure 4).

Four regional tomography models are examined in this study. As previously, we use the $R_{\rho/vs}$ from Adam et al. (2021) and a depth dependent viscosity based on CAM2022 (viscosity law $\eta_3(z)$, section 3.1). Generally, we partially reproduce the observed compression regimes in the northeastern U.S at all depths (Figure 5.2), except for the SATONA model, which reproduces these regimes only between 121 and 253 km depths (Figure 4.18). The observed compression regimes in the NMSZ are retrieved by all models at all depths except while using the CURSA2021 model, which reproduces these regimes only between 33 and 187 km depths (Figure 4.14). The models also partially retrieve the observed extension regimes in the BR-RGR region across all depths (Table 4.1, Figures 4.11- 4.18). In addition, the eastern coastline is associated with an extensional regime, with SH_{max} parallel to the coastline, pattern not observed from the focal mechanisms (Levandowski et al., 2018). This modelled extension regime may reflect a modeling artifact associated with boundary effects except CSEM_North_America tomography model. Furthermore, most of the regional models reproduce the observed few strike slip regimes in Oklahoma and north Texas, feature not retrieved with the global tomography models. However, similar to the most of global tomography models, none of the regional tomography models reproduce the observed strike-slip regimes in the ETSZ at shallow depths.

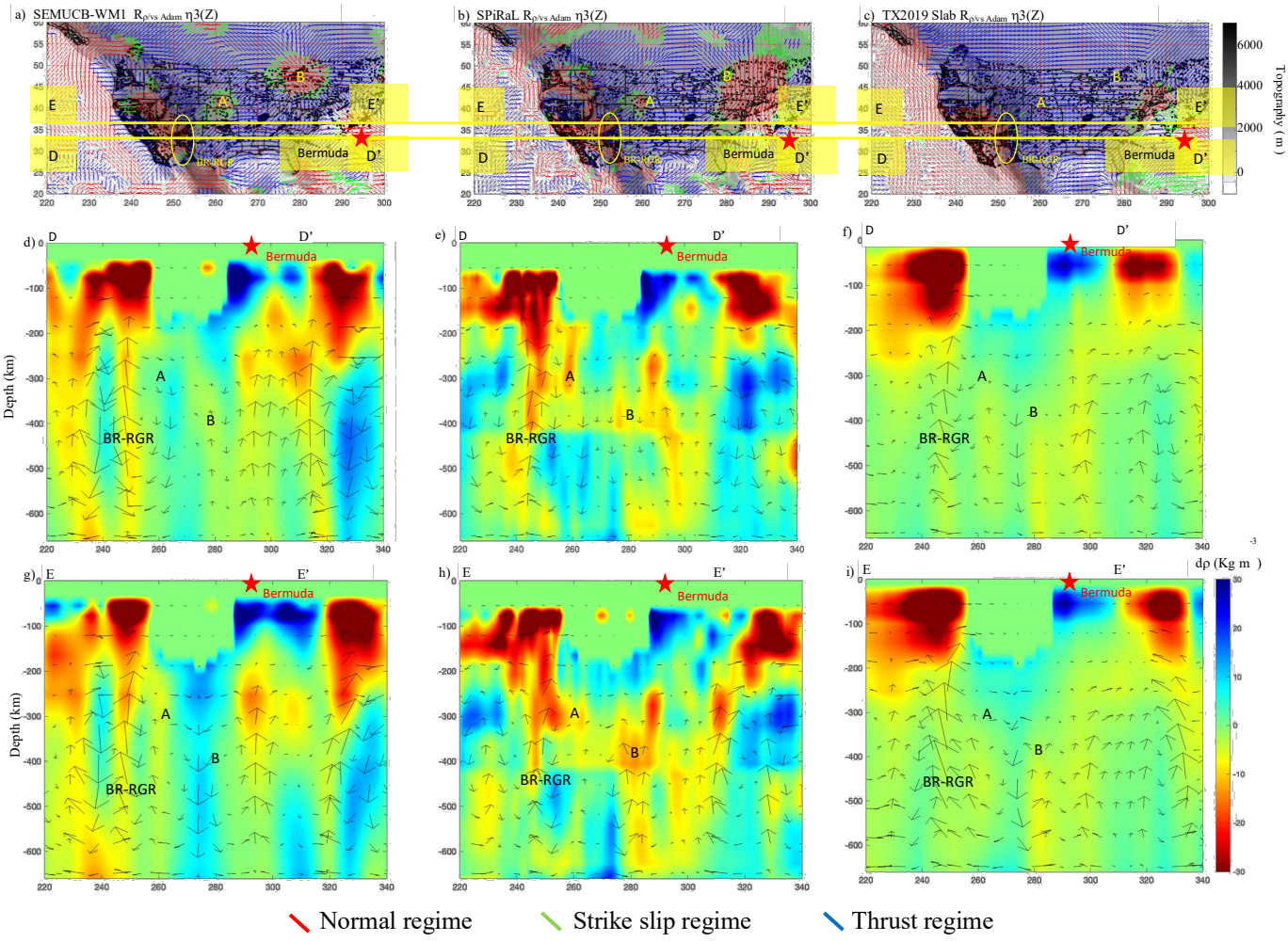

Figure 5.1: Modeled tectonic regimes at depth 99 km using (a) the SEMUCB-WM1 tomography model (French & Romanowicz, 2015), (b) the SPiRaL tomography model (Simmons et al., 2021), and (c) TX2019slab tomography model (Lu et al., 2019) (c), as well as the $R_{\rho/vs}$ from Adam et al. (2021) and the depth dependent viscosity based on CAM2022 (viscosity law $\eta_3(Z)$, section 3.1). Corresponding depth cross-sections of the density anomalies and the induced mantle flow are shown at latitude 33°N in panels d-f and latitude 36°N in panels g-i, respectively.

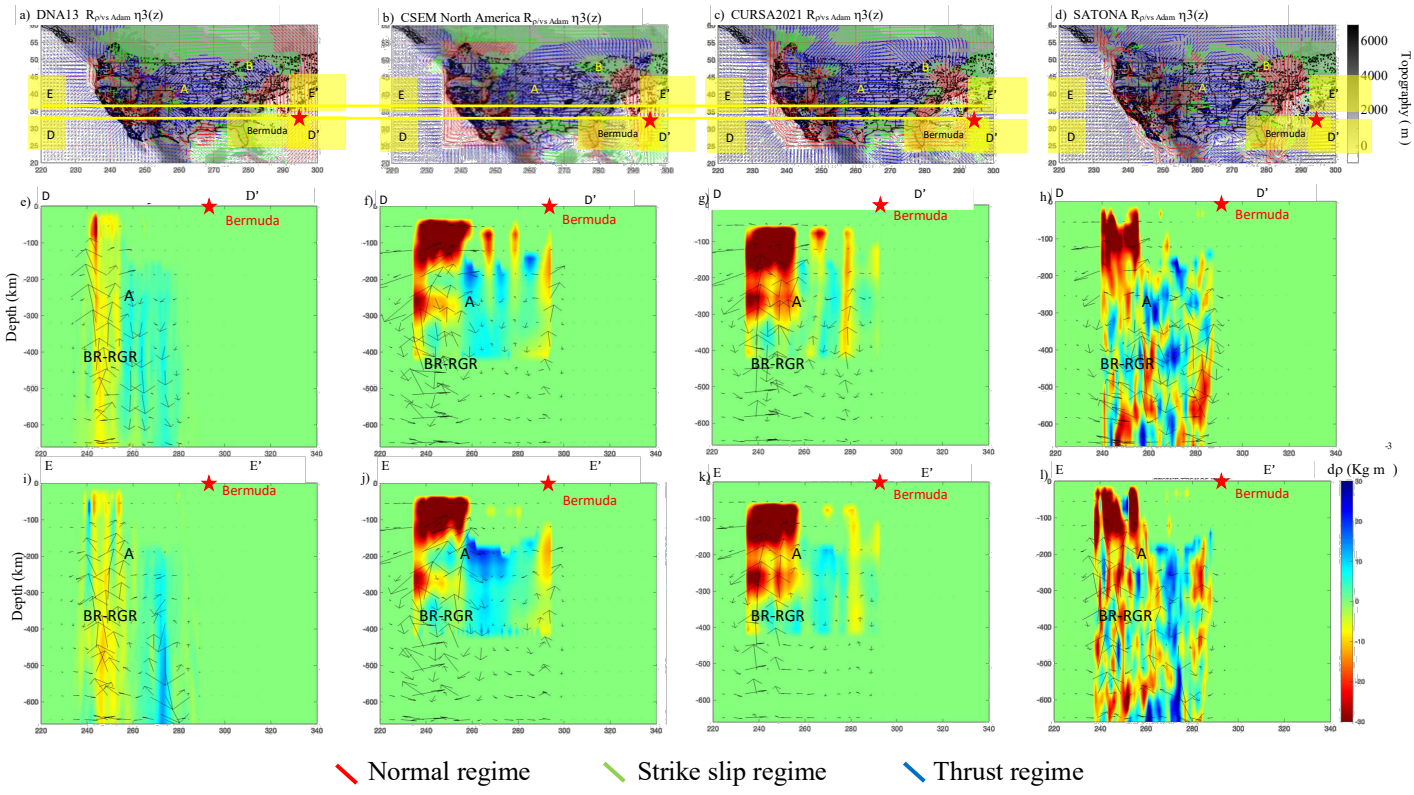

Figure 5.2: Modeled tectonic regimes at 99 km depth modeled from a) the DNA13 tomography model (Porritt et al., 2014), b) the CSEM_North_America tomography model (Fichtner et al., 2018), (c) the CURSA2021 tomography model (Zhou et al., 2022) and d) the SATONA tomography model (Hua et al., 2025), using the $R_{\rho/vs}$ from Adam et al. (2021) and a depth dependent viscosity based on CAM2022 (viscosity law $\eta_3(z)$, section 3.1). Corresponding depth cross-sections are shown at latitude 33°N in panels e-h and latitude 36°N in panels i-l, respectively.

Hua et al. (2025), who designed the SATONA model identified a high S-wave velocity anomaly "dripping" beneath CEUS, from the lithosphere-asthenosphere boundary to the mantle transition zone. This anomaly is interpreted as lithosphere dripping, involving transport of dense lithospheric material into mantle transition zone, causing lithosphere thinning. Their geodynamic modeling suggest that this dripping may be influenced by large scale mantle flow associated with the sinking Farallon slab. In our tectonic regimes modeled from the SATONA tomography model using $R_{\rho/vs}$

from Adam et al. (2021) and depth dependent viscosity (Appendix Figure 5), the extension regimes align around the boundary of the high Vs body identified in that study below 200 km depth. We see this pattern in other regional tomography models (Appendix Figure 6 and 7) except the DNA13 model and all the global tomography models.

Similar to the global models, all regional models show mantle upwellings associate for BR-RGR region and the A and B extension regions, except for the CSEM_North_America tomography model which does not show an upwelling associated with region A. Overall, global tomography models consistently reproduce compressional regimes along major seismic zones at different depths. The absence of the extensional regimes in ETSZ across most of the models suggest that additional mechanisms may be required to explain the observed tectonic regime pattern.

5.1.2 Viscosity laws

We illustrate how varying the viscosity affects the mantle flow and the induced tectonic regimes with the SEMUCB-WM1 tomography model (French & Romanowicz, 2014), (Figure 5.3). We provide a similar figure for the SPiRaL tomography model (Simmons et al., 2021) in Appendix Figure 8.

The majority of observed tectonic regimes within seismic zones are best retrieved using the $\eta 4(T)$ temperature dependent viscosity and $\eta 7(T)$ ($\eta 4(T)$ + WPB). Table 5.1 and Figure 5.4 summarize the RMS values for the viscosity models and considered tomography models as a function of depth. Between 100 and 150 km depths, both $\eta 4(T)$ and $\eta 7(T)$ has the lowest RMS values, indicating improved agreement with the observations (Figure 4.23, Figure 5.4).

For the TX2019slab model, regions A and B exhibits compressional regimes for all viscosity models, despite the presence of mantle upwelling beneath these regions(Appendix Figure 1). In contrast, the SEMUCM-WM1 and SPiRaL models show different modeled tectonic regimes for different viscosity laws. For SEMUCM-WM1 model, the $\eta 5(T,Z)$ and $\eta 6(Z)$ viscosity models retrieve only strike slip regimes in region A, while the extent of the extensional regimes in region B also varies with the included viscosity law (Figure 5.3). Similarly, for SPiRaL model, the $\eta 6(Z)$ viscosity model reproduce strike slip regimes in region A (Appendix Figure 9). In contrast, the SEMUCB-WM1 model with the $\eta 4(T)$ and $\eta 7(T)$ viscosity models retrieve compressional regimes in region A.

Although the modeled tectonic regimes vary with the viscosity law, the mantle upwelling identified beneath these regions remain in all the viscosity models considered. In addition, a mantle upwelling beneath Bermuda is consistently observed across the tested viscosity models (Figure 5.3).

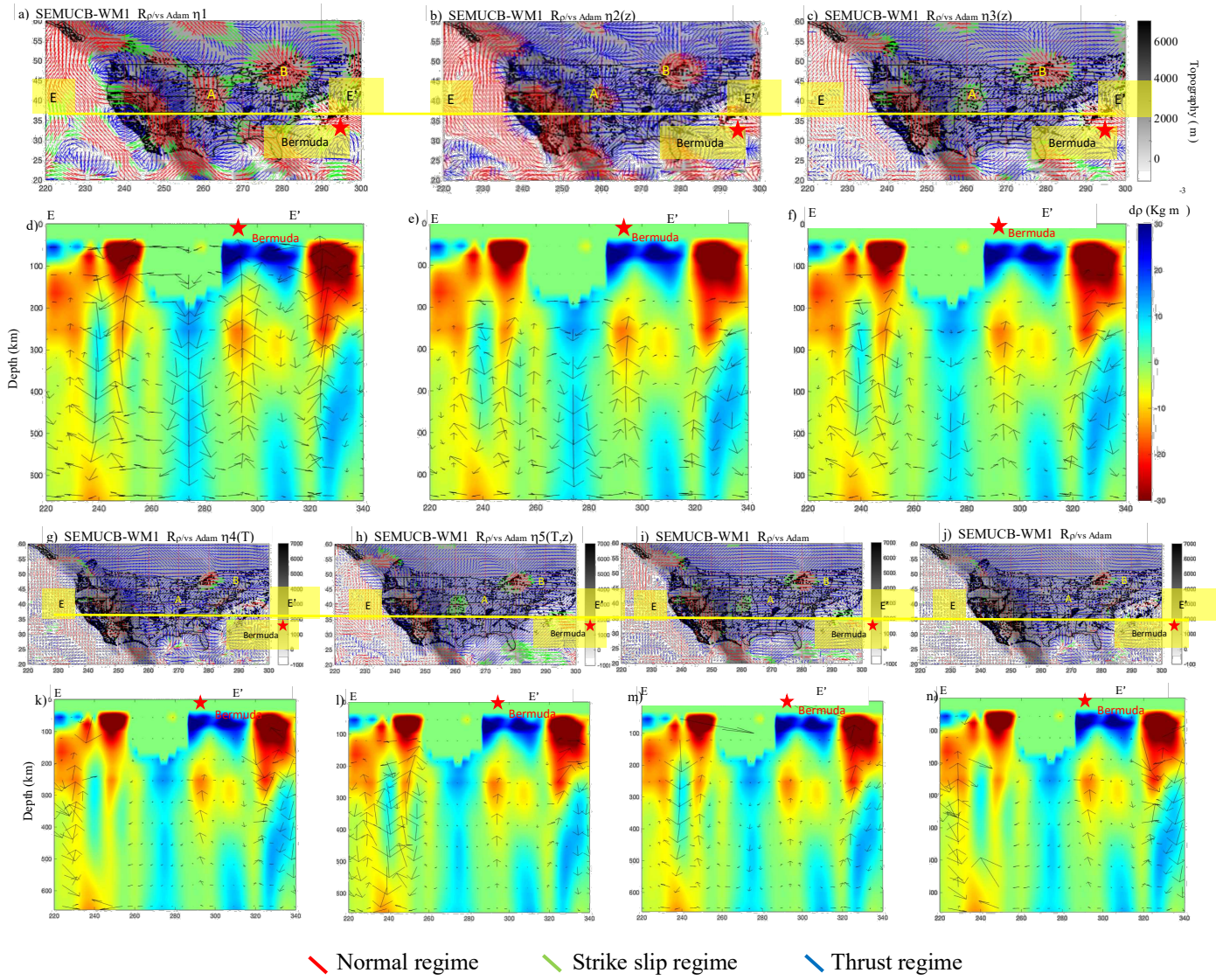

Figure 5.3: Modeled tectonic regimes at 99 km depth with different viscosity laws using SEMUCB-WM1 tomography model (French & Romanowicz, 2014). (a) constant viscosity(η_1), (b) depth dependent viscosity with 100 km thick lithosphere ($\eta_2(Z)$), (c) depth dependent viscosity with LAB CAM2022 ($\eta_3(Z)$), (g) temperature dependent viscosity ($\eta_4(T)$), (h) depth and temperature dependent viscosity ($\eta_5(T,Z)$), (i) depth dependent viscosity with WPB ($\eta_6(Z)$) and (j) temperature dependent viscosity with WPB ($\eta_7(T)$). The conversion factor between seismic velocity anomalies and density anomalies, $R_{\rho/vs}$ is from Adam et al. (2021). Corresponding depth cross-sections are shown at latitude 36°N in panels d-f and k-n.

Table 5.1: RMS values for viscosity models for various depths (33-473 km). Notation of the viscosity laws are described in section 3.1

Viscosity law/ Depth (km)	η1	η2(Z)	η3(Z)	η4(T)	η5(T,Z)	η6(Z)	η7(T)
33	0.878	0.8214	0.8183	0.8379	0.7758	0.7868	0.8363
55	0.8765	0.8214	0.8167	0.8474	0.7836	0.786	0.8482
77	0.8765	0.8214	0.8175	0.7868	0.7813	0.786	0.786
99	0.878	0.8096	0.8143	0.7978	0.7821	0.7836	0.797
121	0.8765	0.8765	0.812	0.7773	0.7836	0.7821	0.7734
143	0.8788	0.8993	0.8072	0.7773	0.7836	0.7813	0.7773
165	0.8741	0.8906	0.819	0.8072	0.7994	0.7899	0.8057
187	0.8733	0.878	0.8301	0.8159	0.8096	0.8049	0.8135
209	0.8686	0.8655	0.8371	0.8206	0.8088	0.8222	0.8214
231	0.8718	0.8592	0.8749	0.8285	0.8175	0.8678	0.8269
253	0.878	0.8615	0.867	0.8198	0.819	0.8686	0.8206
275	0.878	0.867	0.8631	0.8072	0.808	0.8733	0.8057
297	0.871	0.8655	0.8655	0.7954	0.8088	0.8702	0.7946
319	0.8678	0.871	0.8796	0.7931	0.812	0.8828	0.7923
341	0.8765	0.871	0.8836	0.8049	0.8198	0.8843	0.8017
363	0.8749	0.8725	0.8812	0.8127	0.823	0.8875	0.812
385	0.9001	0.871	0.8836	0.819	0.8198	0.8843	0.8198
407	0.8993	0.8765	0.8851	0.8167	0.8167	0.8938	0.8127
429	0.9009	0.9056	0.8914	0.8127	0.8104	0.9103	0.8065
451	0.8961	0.9064	0.9229	0.8293	0.812	0.9481	0.8238
473	0.8867	0.8961	0.9315	0.8623	0.8419	0.9504	0.86

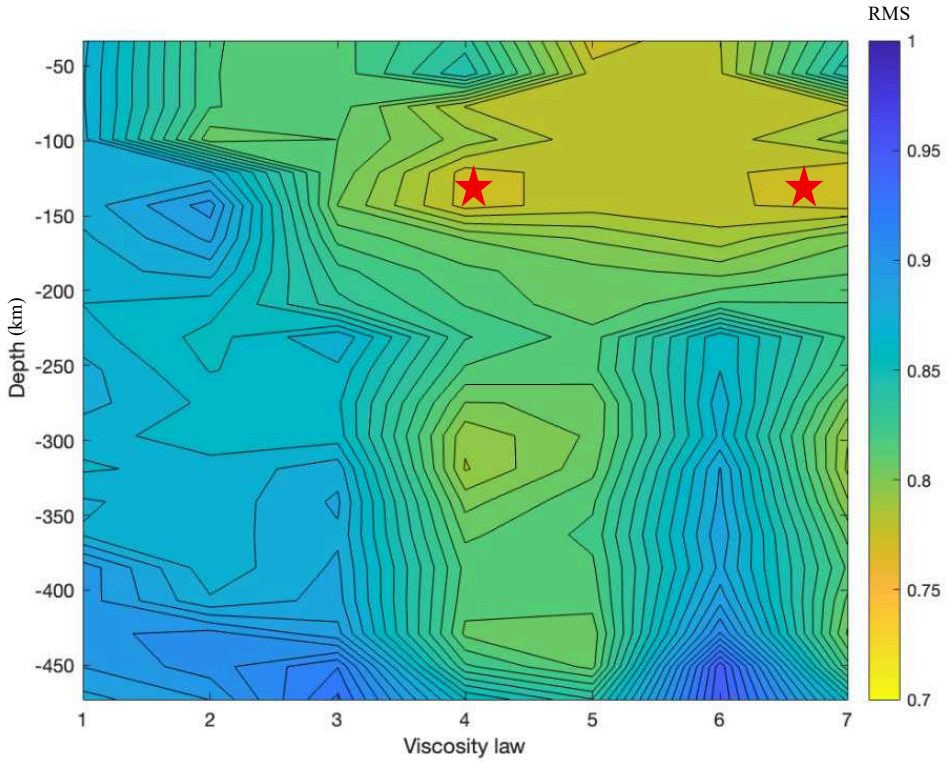

Figure 5.4: RMS (Root Mean Square) between the observed tectonic regimes and the modeled tectonic regimes using the viscosity laws discussed in section 3.1, the SEMUCB-WM1 tomography model (French & Romanowicz, 2014) and the conversion factor between seismic velocity anomalies and density anomalies, $R_{\rho/vs}$ from Adam et al. (2021). The viscosity laws are as follows: constant viscosity (η_1), depth dependent viscosity with 100 km thick lithosphere ($\eta_2(Z)$), depth dependent viscosity with LAB CAM2022 ($\eta_3(Z)$), temperature dependent viscosity ($\eta_4(T)$), depth and temperature dependent viscosity ($\eta_5(T,Z)$), depth dependent viscosity with WPB ($\eta_6(Z)$) and temperature dependent viscosity with WPB ($\eta_7(T)$). Best fits are shown by red stars.

5.1.3 Conversion factors

Some of the most recent conversion factors between seismic velocity anomalies and density anomalies are tested in this study. However, significant differences are not observed in the modeled tectonic regimes when varying the conversion factor. Therefore, this suggests that the conversion factors have a minor influence on the model tectonic regimes and SH_{max}.

5.2 Comparison with former studies

Saxena et al. (2021) also use a tomography model to study the mantle flow beneath CEUS and compute six geodynamic quantities (GPE, dynamic topography, rate of change of dynamic topography, differential stress, Coulomb stress and optimal Coulomb stress). They compute the tectonic regimes, the shear and normal stresses. They propose that the mantle flow induced by the upper mantle heterogeneities is an essential component of the mechanism to reactivate existing faults and therefore to account for the observed intraplate seismicity of CEUS. Using Biryol et al. (2016) regional tomography model, they find extension regimes along the eastern coast and compression in NMSZ in agreement with our results from the regional tomography models. In contrast, they find strike slip regimes in ETSZ. Even after including the GPE, their models do not reproduce the observed extensions along ETSZ though. While comparing the Biryol et al. (2016) regional tomography with other models such as the DNA13 tomography model (Porritt et al., 2014) they highlight a high-velocity anomaly (~200-660 km depths) beneath the region between the ETSZ and NMSZ previously identified by Biryol et al. (2016). Such a feature is also observed in some of the models considered in our study (Figures 5.1g,h, Figure 5.2i,j,l, Appendix Figure 4). Some studies associate this anomaly with the subducted Farallon slab (Chen et al., 2014; Forte et al., 2007; Liu & Stegman, 2011). Additionally, previous work propose that the southern part of the slab, which previously subducted beneath California, has since detached and is now beneath the

CEUS (Chen et al., 2014; Forte et al., 2007; Liu et al., 2008). Biryol et al. (2016) propose this high velocity anomaly as evidence of lithospheric foundering rather than a Grenville-age relict slab or a remnant of Farallon slab.

In terms of SH_{max} orientation, Saxena et al. (2021) report directions that roughly match those of Levandowski et al. (2018) across most seismic zones, except ETSZ. In this region Saxena et al. (2021) report the NNW-SSE SH_{max} direction, in contrast to NE-SW direction reported by Levandowski et al. (2018). This misfit has also been observed by Ghosh et al. (2019). They suggest the misfit may be due to the localized stress concentrations associated with variations in basement rock strength due to the presence of mafic rocks (Powell, 1994), heterogeneity which is difficult to include in either global (Ghosh et al., 2019) or regional (Saxena et al., 2021) modeling approaches. Ghosh et al. (2019) model the lithospheric stress field across CEUS arising from both GPE and basal tractions derived from a global mantle circulation model constrained by tomography and subduction history (Wen & Anderson, 1997). They test four laterally variable viscosity models and predict deviatoric stresses, strain rates and velocities. They compare the modeled maximum compressive stresses with the smoothed stress indicators from Levandowski et al. (2018). Direct comparison with our results is limited, mainly due to the fact that their tomography model is not a "classic" tomography model but also includes the subduction history (Wen & Anderson, 1997). Also, as this model is almost 30 years old, the resolution is very different.

Mantle upwellings are observed beneath several regions in our models, including the BR-RGR, region A, region B and Bermuda. Previous studies have also identified evidence for mantle upwelling beneath the Rio Grande Rift (RGR). Wilson et al. (2005) study on the lithospheric

structure beneath the Rio Grande Rift using teleseismic data from PLAteau / RIo Grande Rift Seismic TRAnsect Experiment (LA RISTRA), a passive seismic array deployed from July 1999 to May 2001. They suggested that the upwelling beneath the rift is broad and laterally distributed rather than narrowly focused beneath the surface rift axis. A similar broad, laterally distributed upwelling is evident beneath BR-RGR in our models (Figure 5.1–5.3). Gao et al. (2004) image the upper mantle structure beneath the Rio Grande Rift using P and S wave tomography. From their seismic images from 200 to 600 km depths, they find two fast seismic anomalies beneath the central Colorado Plateau and the great plains, and one slow anomaly in between. They interpret the western fast anomaly (A, Figure 5.5a) as a foundering Farallon slab, the adjacent slow anomaly (B, Figure 5.5a) as mantle upwelling possibly associate with the volatile release from the sinking Farallon slab (Hua et al., 2025) and the other fast anomaly (C, Figure 5.5a) as a downwelling in the upper mantle beneath the Great Plains. They propose this downwelling may reflect the lithospheric destabilization and eastward removal of weakened lithosphere beneath RGR (Figure 5.5b)

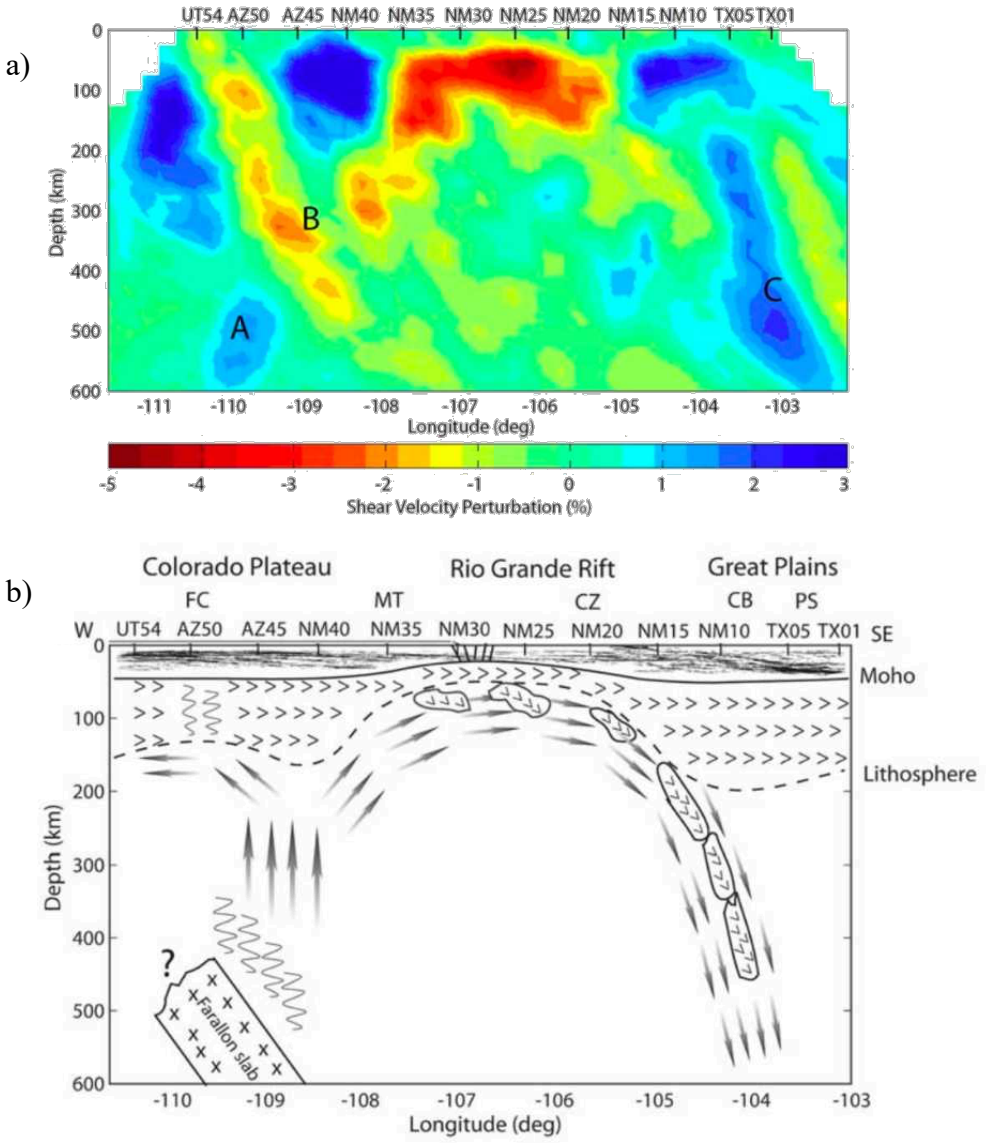

Figure 5.5: a) S wave imaging of the mantle structure showing two fast anomalies (A and C) and a slow anomaly (B); b) Schematic interpretation of mantle structure beneath the Rio Grande rift and surrounding regions, extracted from Gao et al. (2004). The stippled pattern in shallow mantle shows the lithosphere. Arrows represent the mantle flow direction, and wavy lines represent mantle enriched volatiles.

Similarly, Sosa et al. (2014) identity a low velocity zone extending to 200 km depth along the Jemez lineament, originating beneath the Colorado Plateau. They link this zone to an upwelling

sheet of hot material, and term it as the Jemez upwelling potentially produced by small scale upper mantle convection (Figure 5.6).

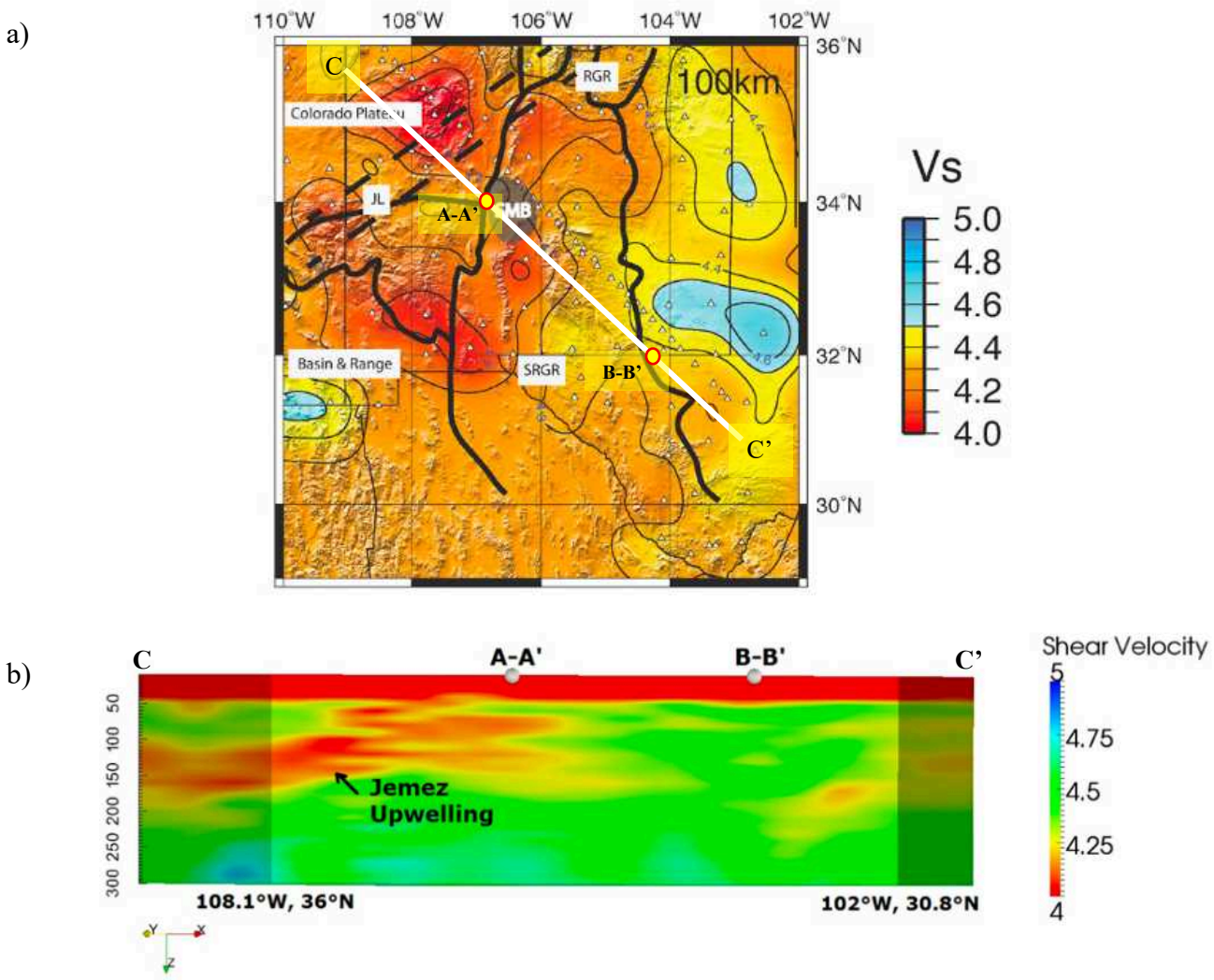

Figure 5.6: a) Shear wave velocity maps at 100 km depth and location of the CC' profile (white line) along which the LA RISTRA experiment has been conducted; b) C–C′ cross section lies on southern part of the LA RISTRA passive experiment. They identify an upwelling beneath the Jemez Lineament (JL), which they term the Jemez Upwelling, modified from Sosa et al. (2014).

They also observe sharp crustal thickness variations between the thick Colorado Plateau and the surrounding thinner extensional provinces. However, because their model only extends up to

latitude 36ºN, they could not determine whether the low-velocity anomaly continues beneath the north of Colorado Plateau. Their results show no evidence for a deep mantle source beneath the Rio Grande Rift, suggesting that present day rifting is not driven by deep mantle upwelling. In contrast, some of the tomography models considered in this study such as SEMUCB-WM1 (Figure 5.1d,g), SPiRaL (Figure 5.1e,h), DNA13 (Figure 5.2 e,i), and SATONA (Figure 5.2 h,l), show anomalies as deep as 660 km. This feature is however not corroborated by all the considered tomography models (Figures 5.1, 5.2).

Magnetotelluric studies by Feucht et al. (2019) also reveal a zone of less resistive beneath north central RGR. They interpret these anomalies as regions that either retained partial melt over geologic time or experienced more recent mantle upwelling and decompression melting. In the southern rift, they identify a low-resistivity zone beneath the transition between the BR-RGR, which they interpret as evidence for adiabatic mantle upwelling and decompression melting of the mantle. Similarly, in our models we observe deep upwelling beneath RGR along profiles at latitude 36ºN and 33ºN, corresponding to the north central (~36.5ºN latitude) and southern rift (~32ºN latitude), (Figure 5.1 and 5.2).

The upwelling associated with the A extension region (initially identified in this study from the SEMUCB-WM1 tomography model (French & Romanowicz, 2015), (Figure 4.1) is located near the eastern margin of the thick Great Plains craton. Although no specific study has focused on the mantle dynamic beneath Nebraska (outside of Saxena et al. (2021) (44ºN-24ºN, 96ºW-68ºW) and Ghosh et al. (2019) (50ºN-30ºN, 92ºW-64ºW) study area), previous studies have characterized the region being underlain by fast seismic velocities with a thick cratonic root. Obrebski et al. (2011) present the DNA10 model and identified fast upper most mantle anomalies extending to 200-300

km depths beneath the stable great plains, and they interpret it as thick cratonic lithosphere. Gao and Li (2021) further showed variations in lithospheric thickness across tectonic boundaries in eastern North America. They suggest that these sharp thickness changes may promote the edge driven mantle convection, caused by a sharp thickness contrast at a craton edge. Therefore, the observed upwelling near the craton margin (i.e., the one we point out in region A, Nebraska) may be related to localized edge driven convection associated with the cratonic and surround lithosphere thickness. Similarly, Hua et al. (2025) propose that slab induced mantle flow pulls deep, compositionally different portion of cratonic lithosphere downward. Their results suggest that subduction-related mantle flow may mobilize and thinning cratonic lithosphere through deep mantle processes, in addition to lateral erosion at craton margins. In contrast Wang et al. (2019) develop a 3D P wave velocity model of the crust and mantle beneath CEUS. They identify a high velocity anomaly in the lower mantle beneath western Nebraska, interpreted as a remanent of the Farallon slab. In their model, we also observe a low-velocity anomaly above the slab, which could induce extensions in the lithosphere.

Another upwelling occurs under the region B (initially identified in this study from the SEMUCB-WM1 tomography model (French & Romanowicz, 2014), (Figure 4.1)). The upwelling is located beneath Ontario and the Great Lakes region. Tao et al. (2025) develop a 3D anisotropic model of northeastern North America and identity strong positive horizontal flow beneath the eastern Great Lakes. They found that these anomalies align with the Cape Verde hotspot track, providing geophysical evidence for the past plume activity. Additionally, they propose that the plume activity may have contributed to the lithospheric thinning and the development of low topography, potentially influencing the formation of the Great Lakes. Our models predict an upwelling beneath

this region and extensional regimes. These results may reflect mantle buoyancy acting beneath the lithosphere that was previously thinned and mechanically weakened by earlier plume interactions. From GPS strain rate results, Ghosh et al. (2019) find a belt of contractions and expansions through the Great Lakes extending to northeast Canada. By comparing GPS data with the ICE-6G theoretical model, the authors concluded that this strain pattern is dominated by Glacial Isostatic Adjustment (GIA). Previous studies have identified a low velocity anomaly beneath New England, which correspond to B extension region although it is shifted eastward in several of our models (Figure 4.4, Figure 4.7, Figure 4.11, Figure 4.13, Figure 4.15. Figure 4.17). Levin et al. (2018) interpreted this anomaly as a localized asthenospheric upwelling produced by edge driven convection. Using tomography and shear wave splitting Frederiksen et al. (2007) found a 200 km thick low velocity anomaly corresponds to the Nipigon Embayment. They interpret this as a chemically origin mantle feature formed as a result of the rifting in the embayment. Menke et al. (2016) analyzed tomographic images of the North Appalachian Anomaly (NAA), a low-velocity feature centered in the asthenosphere beneath southern New England. They argued that the anomaly is not related to the hotspot track but instead it may have caused small-scale upwelling associated with an eddy in asthenospheric flow at the continental margin. Additionally, they propose that this upwelling is most consistent with local upwelling associated with the eastern edge of the Precambrian Laurentian lithosphere. Moreover, Lin et al. (2024) present the first electrical resistivity model of the Mid Continental Rift (MCR) derived from 3D inversion of both USArray and Lithoprobe manetotelluric data. They identified a highly conductive anomaly at the base of the western Superior cratonic lithospheric mantle, and they interpret this as a remnant of a plume trail produced by metasomatism and/or partial melting of lithospheric mantle as the Keweenaw plume (centered approximately beneath the Lake Superior region) formed. We observe

upwelling beneath the Great Lake and New England region in almost all our models. The upwelling is more widespread in the SPiRaL model (Figure 4.4), whereas several other models show smaller relative amplitude compared to the amplitude of the upwelling occurring outside the continental region (Figure 4.1, Figure 4.7, Figure 4.11, Figure 4.13, Figure 4.15, Figure 4.17).

Previous studies have suggested that the Bermuda rise, a cluster of extinct volcanoes, has been created by the edge-driven convection, a convective pattern induced by the lithospheric step between the thick north American continental lithosphere and the thin Atlantic oceanic lithosphere (King and Anderson, 1998). In the present study, however, mantle upwelling beneath Bermuda is evident in the depth cross sections from both the global and regional tomography models (Figure 5.1, Figure 5.2, Figure 4.15, Figure 4.17). This observation suggest that Bermuda rise may not be solely explained by the shallow edge driven convection but may also involve a deep mantle contribution, as an upwelling occurring at depths 400-600 km is observed in most of our models.

Overall, despite differences among the tomography models and viscosity laws, several features consistently reproduced. For instance, mantle upwellings beneath the BR-RGR, region A, region B and Bermuda remain present across most of the models. This consistency may indicate that such upwelling flows actually occur under the North American continent. Understanding their origin and dynamics could bring new constraints on the lithosphere-asthenosphere interaction.

Chapter 6 - Conclusion

In this study, we investigate the potential role of mantle dynamics in the origin of intraplate seismicity in CEUS. Using several recently published global and regional models, we compute instantaneous mantle flow, tectonic regimes and SH_{max} and compare the modeled results with those assessed from observation such as earthquake focal mechanisms. We also test the influence of model parameters including tomography models, conversion factor between seismic velocity anomalies and density anomalies, $R_{\rho/vs}$ and viscosity laws.

The main findings of this study are as follows.

- The tomography model and viscosity laws have a strong influence on the modeled tectonic regimes and SH_{max} directions, whereas the conversion factor between seismic velocity anomalies and density anomalies has only a minor effect.
- The strongest overall agreement is obtained with the TX2019slab tomography model with the Adam et al. (2021) conversion factor and depth dependent viscosity based on CAM2022 lithosphere.
- Most of the global tomography models recover the compressive regimes observed in the northeastern part of the North American continent. This pattern is generally not recovered using regional models which suggests that it is created by larger scales flows (~5,000 km wavelength, see Figure 5.1).
- Global tomography models reproduce most of the observed tectonic regimes in the seismic zones including NMSZ, SCSZ and GCSZ. The mantle upwelling beneath BR-RGR, region A, region B and Bermuda appear consistently across the tested models, suggesting these features are real rather than model artifacts.

- A high-density anomaly between the ETSZ and NMSZ is consistently seen in the models, in agreement with the previous studies and is associated with the downwelling flow in the upper mantle. This suggests the presence of dense lithospheric material or may be foundering lithosphere in this region. The observed extension in the ETSZ may be created by shallower phenomena rather than mantle dynamics.
- The tectonic regimes in the ETSZ are not well retrieved by the models, suggesting that deformation in this region may be controlled by shallower or more localized processes rather than mantle dynamics alone.

Future work should integrate GPE and GIA data and evaluate model performance by computing RMS using weighted observation map, with greater weight assigned to regions with high seismicity. Although this study compares the modeled tectonic regimes and SH_{max} with those derived from focal mechanisms, the transmission mechanisms of mantle flow induced stresses through lithosphere remain to be assessed. The problem with the present approach is that the lithosphere strength in theory bigger than the stresses induced by the mantle flow and these stresses may be insufficient to break the lithosphere. A more insightful approach would be needed to evaluate how mantle flow induced stresses could reactivate existing faults. This approach has partially been developed by Saxena et al. (2021). However, in the future would like to implement all the parameters studied within the present work and a more realistic description of the existing faults.

References

Adam, C., King, S. D., & Caddick, M. J. (2021). Mantle temperature and density anomalies: The influence of thermodynamic formulation, melt, and anelasticity. *Physics of the Earth and Planetary Interiors*, *319*, 106772.

Adam, C., Madureira, P., Miranda, J. M., Lourenço, N., Yoshida, M., & Fitzenz, D. (2013). Mantle dynamics and characteristics of the Azores plateau. *Earth and Planetary Science Letters*, *362*, 258–271.

Adam, C., Yoshida, M., Isse, T., Suetsugu, D., Fukao, Y., & Barruol, G. (2010). South Pacific hotspot swells dynamically supported by mantle flows. *Geophysical Research Letters*, *37*(8).

Becker, T. W., Lowry, A. R., Faccenna, C., Schmandt, B., Borsa, A., & Yu, C. (2015). Western US intermountain seismicity caused by changes in upper mantle flow. *Nature,* 524(7566), 458–461.

Biryol, C. B., Wagner, L. S., Fischer, K. M., & Hawman, R. B. (2016). Relationship between observed upper mantle structures and recent tectonic activity across the Southeastern United States. *Journal of Geophysical Research: Solid Earth*, *121*(5), 3393–3414.

Boyce, A., Bastow, I. D., Golos, E. M., Rondenay, S., Burdick, S., & van der Hilst, R. D. (2019). Variable modification of continental lithosphere during the Proterozoic Grenville orogeny: Evidence from teleseismic P-wave tomography. *Earth and Planetary Science Letters*, *525*.

Chen, C., Zhao, D., & Wu, S. (2014). Crust and upper mantle structure of the New Madrid Seismic Zone: Insight into intraplate earthquakes. *Physics of the Earth and Planetary Interiors*, *230*, 1–14.

Coruh, C, Bollinger, G A, & Costain, J K (1988). Seismogenic structures in the central Virginia seismic zone. *Geology; (United States),* 16:8.

Craig, T. J., Chanard, K., & Calais, E. (2017). Hydrologically - driven crustal stresses and seismicity in the New Madrid Seismic Zone. Nature communications, 8(1), 2143.

Frederiksen, A. W., Miong, S. K., Darbyshire, F. A., Eaton, D. W., Rondenay, S., & Sol, S. (2007). Lithospheric variations across the Superior Province, Ontario, Canada: Evidence from tomography and shear wave splitting. *Journal of Geophysical Research: Solid Earth*, *112*(B7).

Feucht, D. W., Bedrosian, P. A., & Sheehan, A. F. (2019). Lithospheric signature of late Cenozoic extension in electrical resistivity structure of the Rio Grande rift, New Mexico, USA. *Journal of Geophysical Research: Solid Earth*, *124*(3), 2331-2351.

Fichtner, A., van Herwaarden, D. P., Afanasiev, M., Simutė, S., Krischer, L., Çubuk-Sabuncu, Y., et al. (2018). The collaborative seismic earth model: generation 1. *Geophysical research letters*, *45*(9), 4007-4016.

Forte, A. M., Mitrovica, J. X., Moucha, R., Simmons, N. A., & Grand, S. P. (2007). Descent of the ancient Farallon slab drives localized mantle flow below the New Madrid seismic zone. *Geophysical Research Letters*, *34*(4).

French, S. W., & Romanowicz, B. A. (2014). Whole-mantle radially anisotropic shear velocity structure from spectral-element waveform tomography. *Geophysical Journal International*, *199*(3), 1303-1327.

Fullea, J., Lebedev, S., Martinec, Z., & Celli, N. L. (2021). WINTERC-G: Mapping the upper mantle thermochemical heterogeneity from coupled geophysical–petrological inversion of seismic waveforms, heat flow, surface elevation and gravity satellite data. *Geophysical Journal International, 226*(1), 146–191.

Gallen, S. F., & Thigpen, J. R. (2018). Lithologic controls on focused erosion and intraplate earthquakes in the eastern Tennessee seismic zone. Geophysical Research Letters, 45(18), 9569-9578.

Gan, W., & Frohlich, C. (2013). Gas injection may have triggered earthquakes in the Cogdell oil field, Texas. Proceedings of the National Academy of Sciences, 110(47), 18786-18791.

Gao, H., & Li, C. (2021). Lithospheric formation and evolution of eastern North American continent. *Geophysical Research Letters*, *48*, e2020GL091074.

Gao, W., Grand, S. P., Baldridge, W. S., Wilson, D., West, M., Ni, J. F., & Aster, R. (2004). Upper mantle convection beneath the central Rio Grande rift imaged by P and S wave tomography. *Journal of Geophysical Research: Solid Earth*, *109*(B3).

Ghosh, A., Holt, W. E., & Bahadori, A. (2019). Role of large-scale tectonic forces in intraplate earthquakes of central and eastern North America. *Geochemistry, Geophysics, Geosystems*, *20*(4), 2134-2156.

Grollimund, B., & Zoback, M. D. (2001). Did deglaciation trigger intraplate seismicity in the New Madrid seismic zone? In *Geology*. www.copyright.com.

Gurnis, M., Mitrovica, J. X., Ritsema, J., & van Heijst, H. J. (2000). Constraining mantle density structure using geological evidence of surface uplift rates: The case of the African superplume. *Geochemistry, Geophysics, Geosystems*, *1*(7).

Heidbach, O., Rajabi, M., Cui, X., Fuchs, K., Müller, B., Reinecker, J., Reiter, K., Tingay, M., Wenzel, F., Xie, F., Ziegler, M. O., Zoback, M.-L., & Zoback, M. (2018). The World Stress Map database release 2016: Crustal stress pattern across scales. *Tectonophysics*, *744*, 484–498.

Heidbach, O., Tingay, M., Barth, A., Reinecker, J., Kurfeß, D., & Müller, B. (2010). Global crustal stress pattern based on the World Stress Map database release 2008.

Hightower, E., Gurnis, M., & Mao, W. (2024). Influence of Farallon slab loading on intraplate stress and seismicity in eastern North America in the presence of pre-existing weak zones. *Geochemistry, Geophysics, Geosystems, 25(6), e2024GC011493.*

Hua, J., Grand, S. P., Becker, T. W., Janiszewski, H. A., Liu, C., Trugman, D. T., & Zhu, H. (2025). Seismic full-waveform tomography of active cratonic thinning beneath North America consistent with slab-induced dripping. *Nature Geoscience*, *18*(4), 358-364.

Humphreys, E. D., & Coblentz, D. D. (2007). North American dynamics and western U.S. tectonics. *Reviews of Geophysics*, *45*(3).

Karato, S. I. (2008). *Deformation of Earth Materials: An Introduction to the Rheology of Solid Earth*. Cambridge University Press, New York.

King, S. D., & Anderson, D. L. (1998). Edge-driven convection. Earth and Planetary Science Letters, 160(3), 289–296.

Lee C.-K., S.-C. Hana, and B. Steinberger (2011). Influence of variable uncertainties in seismic tomography models on constraining mantle viscosity from geoid observations. Physics of the Earth and Planet. Int., 184 (2011) 51–62.

Levandowski, W. (2026). Seismogenic Crustal Stress in Intraplate North America: Slip Potential of Suspected Quaternary Faults in the Central and Eastern United States, Seismol. Res. Lett. 97, 1–23.

Levandowski, W., Boyd, O. S., & Ramirez-Guzmán, L. (2016). Dense lower crust elevates long-term earthquake rates in the New Madrid seismic zone. *Geophysical Research Letters,* 43(16), 8499–8510.

Levandowski, W., Herrmann, R. B., Briggs, R., Boyd, O., & Gold, R. (2018). An updated stress map of the continental United States reveals heterogeneous intraplate stress. *Nature Geoscience*, 11(6), 433-437.

Levandowski, W., Zellman, M., & Briggs, R. (2017). Gravitational body forces focus North American intraplate earthquakes. *Nature Communications*, *8*.

Levin, V., Long, M. D., Skryzalin, P., Li, Y., & López, I. (2018). Seismic evidence for a recently formed mantle upwelling beneath New England. *Geology*, *46*(1), 87-90.

Li, N., Li, B., Chen, D., Wang, E., Tan, Y., Qian, J., & Jia, H. (2020). Waveform characteristics of earthquakes induced by hydraulic fracturing and mining activities: Comparison with those of natural earthquakes. Natural Resources Research, 29(6), 3653-3674.

Li, Q., Liu, M., Zhang, Q., & Sandvol, E. (2007). Stress evolution and seismicity in the central eastern United States: Insights from geodynamic modeling.

Lin, W., Schultz, A., Yang, B., Harris, L. B., & Hu, X. (2024). Mantle plume trail beneath the ca. 1.1 Ga North American Midcontinent Rift revealed by magnetotelluric data. *National Science Review*, *11*(8), nwae239.

Liu, L., & Stegman, D. R. (2011). Segmentation of the Farallon slab. *Earth and Planetary Science Letters*, *311*(1-2), 1-10.

Liu, L., Spasojevic, S., & Gurnis, M. (2008). Reconstructing Farallon plate subduction beneath North America back to the Late Cretaceous. *Science*, *322*(5903), 934-938.

Liu, M., & Stein, S. (2016). Mid-continental earthquakes: Spatiotemporal occurrences, causes, and hazards. *Earth-Science Reviews*, *162*, 364-386.

Lu, C., Grand, S. P., Lai, H., & Garnero, E. J. (2019). TX2019slab: A new P and S tomography model incorporating subducting slabs. *Journal of Geophysical Research: Solid Earth, 124*(11), 11,549–11,567.

Lundstern, J. E., & Zoback, M. D. (2020). Multiscale variations of the crustal stress field throughout North America. *Nature communications*, 11(1), 1951.

Mazzotti, S., James, T. S., Henton, J., & Adams, J. (2005). GPS crustal strain, postglacial rebound, and seismic hazard in eastern North America: The Saint Lawrence valley example. *Journal of Geophysical Research: Solid Earth*, *110*(11), 1–16.

Mazzotti, S., & Townend, J. (2010). State of stress in central and eastern North American seismic zones. *Lithosphere*, *2*(2), 76-83.

Menke, W., Skryzalin, P., Levin, V., Harper, T., Darbyshire, F., & Dong, T. (2016). The Northern Appalachian anomaly: A modern asthenospheric upwelling. *Geophysical Research Letters*, *43*(19), 10-173.

Muir-Wood, R. (2000). Deglaciation Seismotectonics: a principal influence on intraplate seismogenesis at high latitudes. *Quaternary Science Reviews*, *19*(14–15).

Murphy, B. S., Liu, L., & Egbert, G. D. (2019). Insights into intraplate stresses and geomorphology in the southeastern United States. *Geophysical Research Letters*, 46, 8711–8720.

Obrebski, M., Allen, R. M., Pollitz, F., & Hung, S.-H. (2011). Lithosphere–asthenosphere interaction beneath the western United States from the joint inversion of body-wave travel times and surface-wave phase velocities. *Geophysical Journal International, 185*(2), 1003–1021.

Pascal, C., & Cloetingh, S. A. P. L. (2009). Gravitational potential stresses and stress field of passive continental margins: Insights from the south-Norway shelf. *Earth and Planetary Science Letters*, *277*(3–4), 464–473.

Porritt, R. W., Allen, R. M., & Pollitz, F. F. (2014). Seismic imaging east of the Rocky Mountains with USArray. *Earth and Planetary Science Letters*, *402*(C), 16–25.

Powell, C. A., Bollinger, G. A., Chapman, M. C., Sibol, M. S., Johnston, A. C., & Wheeler, R. L. (1994). A seismotectonic model for the 300-kilometer-long eastern Tennessee seismic zone. *Science*, *264*(5159), 686-688.

Powell, C. A., & Thomas, W. A. (2016). Grenville basement structure associated with the Eastern Tennessee seismic zone, southeastern USA. Geology, 44(1), 39-42.

Priestley, K., Ho, T., Takei, Y., & McKenzie, D. (2024). The thermal and anisotropic structure of the top 300 km of the mantle. *Earth and Planetary Science Letters*, *626*, 118525.

Priestley, K., McKenzie, D., & Ho, T. (2019). *A Lithosphere–Asthenosphere Boundary—a Global Model Derived from Multimode Surface-Wave Tomography and Petrology* (pp.111–123).

Saxena, A., Choi, E., Powell, C. A., & Aslam, K. S. (2021). Seismicity in the central and southeastern United States due to upper mantle heterogeneities. *Geophysical Journal International*, *225*(3), 1624-1636.

Shah, A. K., Pratt, T. L., & Horton, J. W. Jr. (2023). *Rift basins and intraplate earthquakes: New high-resolution aeromagnetic data provide insights into buried structures of the Charleston, South Carolina seismic zone*. *Geochemistry, Geophysics, Geosystems*, 24, e2022GC010803.

Simmons, N. A., Forte, A. M., & Grand, S. P. (2009). Joint seismic, geodynamic and mineral physical constraints on three-dimensional mantle heterogeneity: Implications for the relative importance of thermal versus compositional heterogeneity. *Geophysical Journal International*, *177*(3), 1284–1304.

Simmons, N. A., Myers, S. C., Morency, C., Chiang, A., & Knapp, D. R. (2021). SPiRaL: A multiresolution global tomography model of seismic wave speeds and radial anisotropy variations in the crust and mantle. *Geophysical Journal International, 227*(3), 1366–1391.

Sosa, A., Thompson, L., Velasco, A. A., Romero, R., & Herrmann, R. B. (2014). 3-D structure of the Rio Grande Rift from 1-D constrained joint inversion of receiver functions and surface wave dispersion. *Earth and Planetary Science Letters*, *402*, 127-137.

Stadler, G., Gurnis, M., Burstedde, C., Wilcox, L. C., Alisic, L., & Ghattas, O. (2010). The dynamics of plate tectonics and mantle flow: From local to global scales. *Science, 329*(5995), 1033-1037.

Steinberger, B., & Calderwood, A. R. (2006). Models of large-scale viscous flow in the Earth's mantle with constraints from mineral physics and surface observations. *Geophysical Journal International*, *167*(3), 1461–1481.

Tao, Z., Li, A., Wu, J., & Fischer, K. M. (2025). Revealing the Cape Verde hotspot track across the Great Lakes. *Geophysical Research Letters*, *52*, e2024GL110777.

Tuttle, M. P., K. DyerWilliams, M. W. Carter, S. L. Forman, K. Tucker, Z. Fuentes, C. Velez, and L. M. Bauer (2021). The Liquefaction Record of Past Earthquakes in the Central Virginia Seismic Zone, Eastern United States, Seismol. Res. Lett. XX, 1–19.

Wang, H., Zhao, D., Huang, Z., & Wang, L. (2019). Tomography, seismotectonic and mantle dynamics of central and eastern United States. *Journal of Geophysical Research: Solid Earth*, *124*, 8890–8907.

Wen, L., & Anderson, D. L. (1997). Slabs, hotspots, cratons and mantle convection revealed from residual seismic tomography in the upper mantle. *Physics of the Earth and Planetary Interiors*, *99*(1-2), 131-143.

Wilson, D., Aster, R., West, M. *et al.* Lithospheric structure of the Rio Grande rift. *Nature* **433**, 851–855 (2005).

Wu, P., & Johnston, P. (2000). Can deglaciation trigger earthquakes in North America? *Geophysical Research Letters*, *27*(9), 1323-1326.

Xie, J., Chu, R., & Yang, Y. (2018). 3-D Upper-Mantle Shear Velocity Model Beneath the Contiguous United States Based on Broadband Surface Wave from Ambient Seismic Noise. In *Pure and Applied Geophysics* (Vol. 175, Issue 10, pp. 3403–3418). Birkhauser Verlag AG.

Yoshida, M. (2008). Core-mantle boundary topography estimated from numerical simulations of instantaneous mantle flow. *Geochemistry, Geophysics, Geosystems*, *9*(7).

Yoshida, M. (2010). Preliminary three-dimensional model of mantle convection with deformable, mobile continental lithosphere. *Earth and Planetary Science Letters*, *295*(1– 2), 205–218.

Zhan, Y., Hou, G., Kusky, T., & Gregg, P. M. (2016). Stress development in heterogenetic lithosphere: Insights into earthquake processes in the New Madrid Seismic Zone. *Tectonophysics*, *671*, 56–62.

Zhou, T., Li, J., Xi, Z., Li, G., & Chen, M. (2022). CUSRA2021: A radially anisotropic model of the contiguous US and surrounding regions by full-waveform inversion. *Journal of Geophysical Research: Solid Earth*, *127*(8), e2021JB023893.

Appendix

Appendix 1

Appendix 1 contains the equations of the stress tensor.

$$\sigma_{rr} = -p + 2\mu \frac{\partial v_r}{\partial r}$$

$$\sigma_{\theta\theta} = -p + 2\mu \left(\frac{1}{r} \frac{\partial v_\theta}{\partial \theta} + \frac{v_r}{r} \right)$$

$$\sigma_{\varphi\varphi} = -p + 2\mu \left(\frac{1}{r sin\theta} \frac{\partial v_\varphi}{\partial \varphi} + \frac{v_r}{r} + \frac{cot\theta v_\theta}{r} \right)$$

$$\sigma_{r\theta} = \sigma_{\theta r} = \mu \left(\frac{1}{r} \frac{\partial v_r}{\partial \theta} + \frac{\partial v_\theta}{\partial r} - \frac{v_\theta}{r} \right)$$

$$\sigma_{r\varphi} = \sigma_{\varphi r} = \mu \left(\frac{1}{r sin\theta} \frac{\partial v_r}{\partial \varphi} + \frac{\partial v_\varphi}{\partial r} - \frac{v_\varphi}{r} \right)$$

$$\sigma_{\theta\varphi} = \sigma_{\varphi\theta} = \mu \left(\frac{1}{r sin\theta} \frac{\partial v_\theta}{\partial \varphi} + \frac{1}{r} \frac{\partial v_\varphi}{\partial \theta} - \frac{cot\theta v_\varphi}{r} \right)$$

$$\sigma = \begin{bmatrix} \sigma_{\theta\theta} & \sigma_{\theta\varphi} & \sigma_{r\theta} \\ \sigma_{\theta\varphi} & \sigma_{\varphi\varphi} & \sigma_{\varphi r} \\ \sigma_{r\theta} & \sigma_{\varphi r} & \sigma_{rr} \end{bmatrix}$$ (Equation 11)

Here σ are the stress components of the stress tensor, in the longitudinal θ, latitudinal φ, and radial r directions, v is the convection velocities in θ, φ and r directions, p is pressure and μ is the viscosity.

Appendix 2

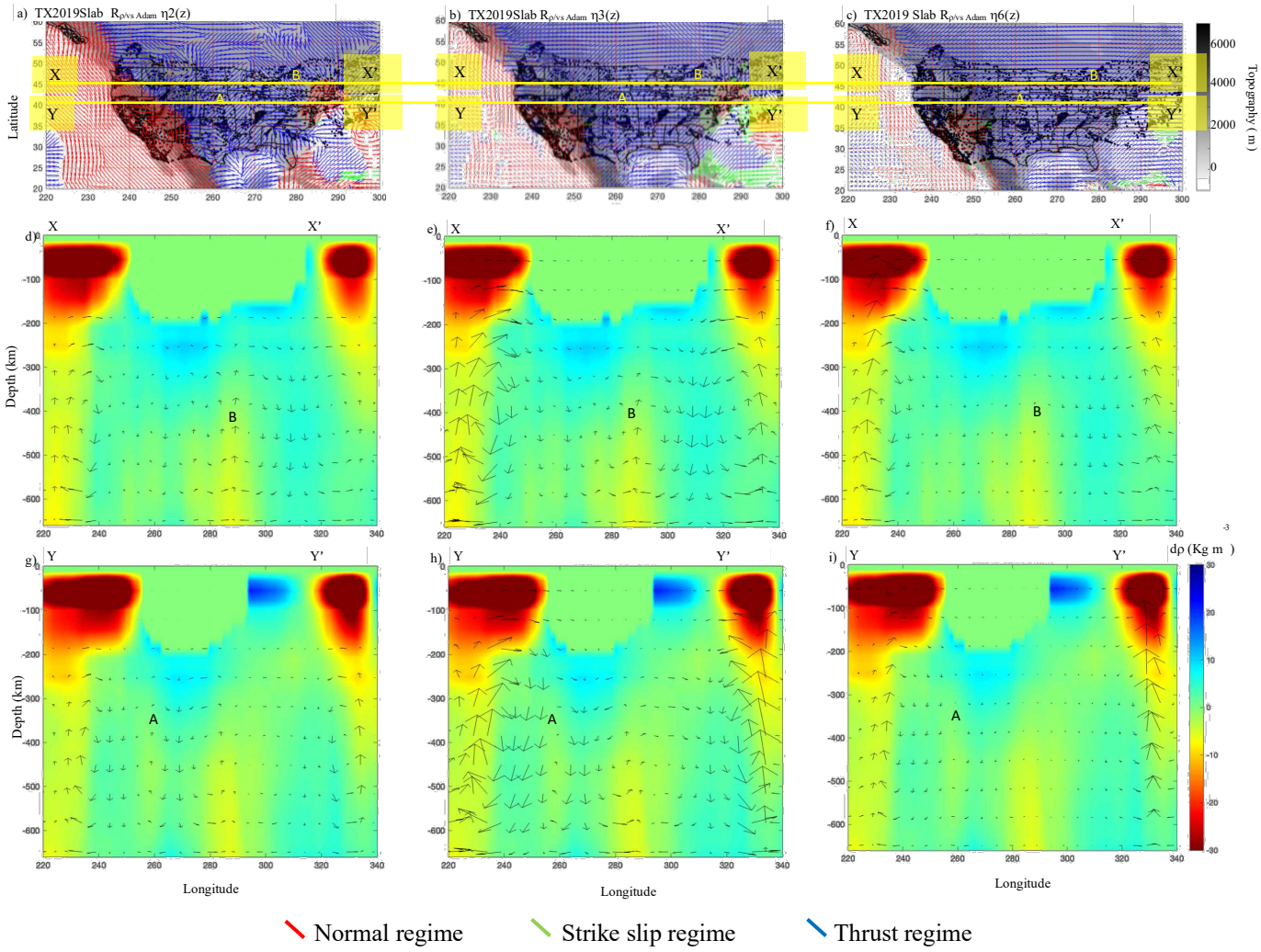

Appendix Figure 1: Modeled tectonic regimes at depth 99 km using the TX2019slab tomography model (Lu et al., 2019) with depth dependent viscosity laws, $\eta_2(Z)$, (a), $\eta_3(Z)$, (b) $\eta_6(Z)$, (c) (section 3.1) as well as the $R_{\rho/vs}$ from Adam et al. (2021). Corresponding depth cross-sections of the density anomalies and the induced mantle flow are shown at latitude 45°N in panels d-f and latitude 40°N in panels g-i, respectively.

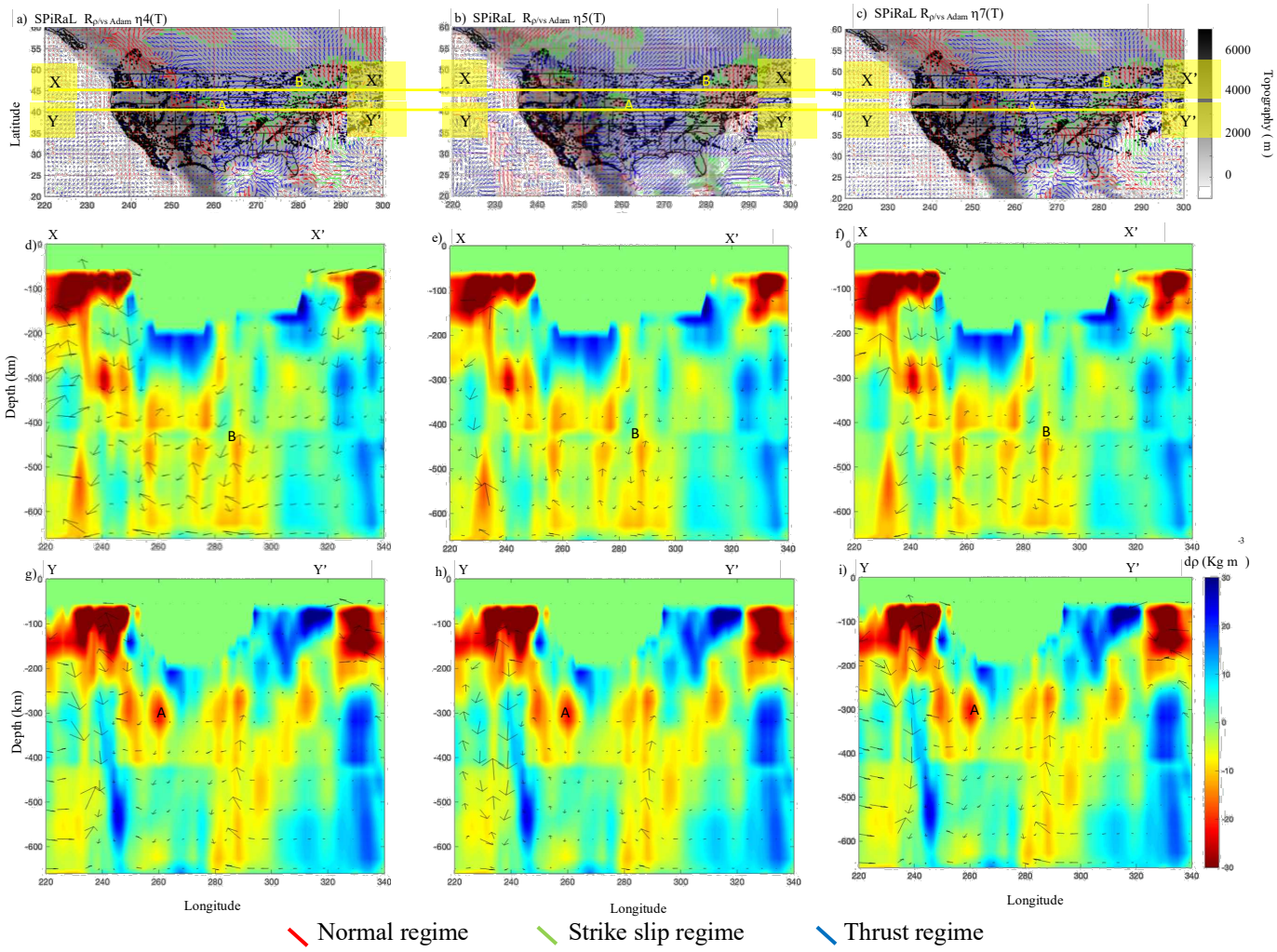

Appendix Figure 2: Modeled tectonic regimes at depth 99 km using the SPiRaL tomography model (Simmons et al., 2021), with temperature and both depth and temperature dependent viscosity laws, $\eta_4(T)$, (a), $\eta_5(T,Z)$, (b) and $\eta_7(T)$, (c) (section 3.1) as well as the $R_{\rho/vs}$ from Adam et al. (2021). Corresponding depth cross-sections of the density anomalies and the induced mantle flow are shown at latitude 45°N in panels d-f and latitude 40°N in panels g-i, respectively.

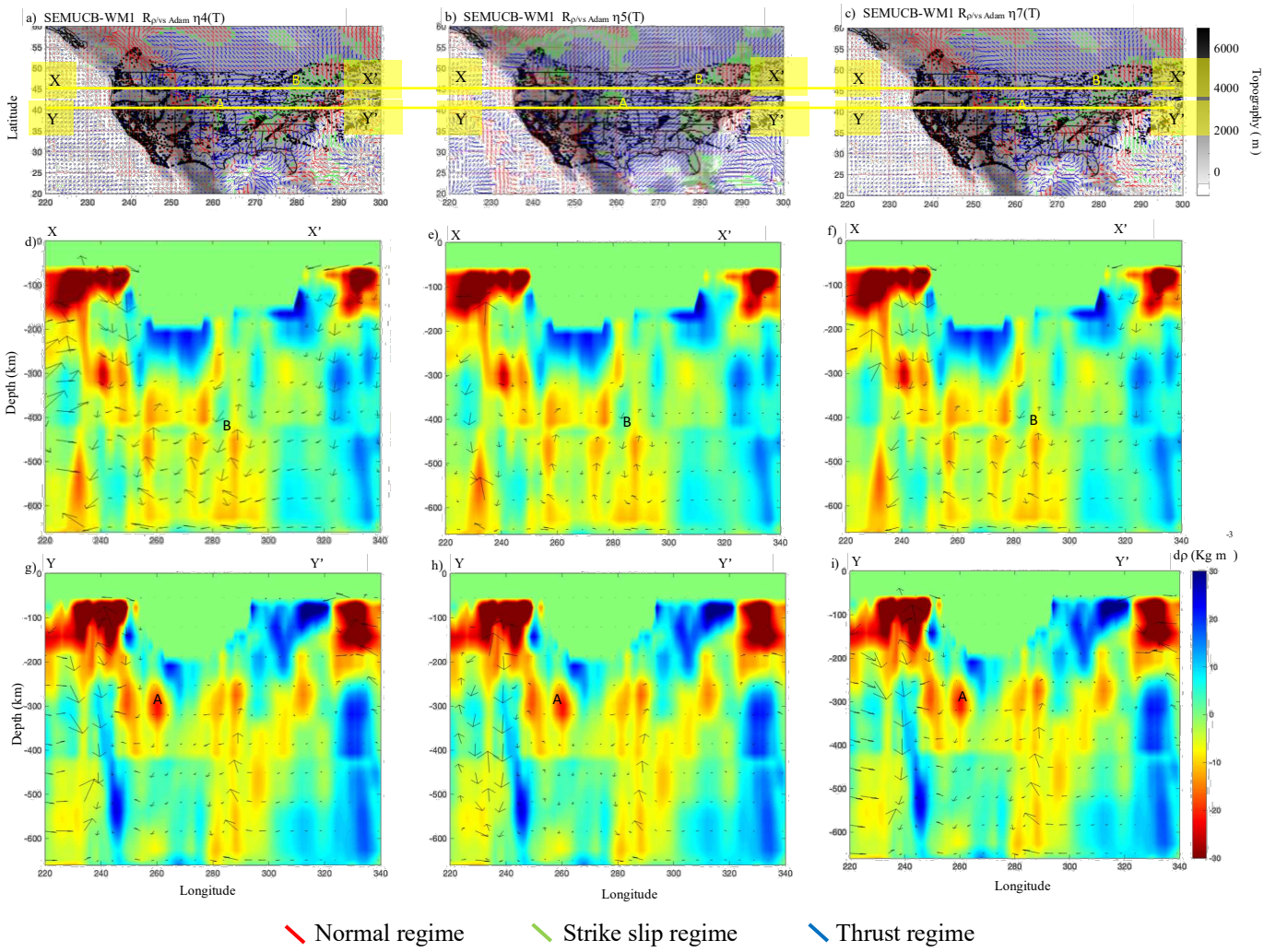

Appendix Figure 3: Modeled tectonic regimes at depth 99 km using the SEMUCB-WM1 tomography model (French & Romanowicz, 2015), with temperature and both depth and temperature dependent viscosity laws, $\eta_4(T)$, (a), $\eta_5(T,Z)$, (b) and $\eta_7(T)$, (c) (section 3.1) as well as the $R_{\rho/vs}$ from Adam et al. (2021). Corresponding depth cross-sections of the density anomalies and the induced mantle flow are shown at latitude 45°N in panels d-f and latitude 40°N in panels g-i, respectively.

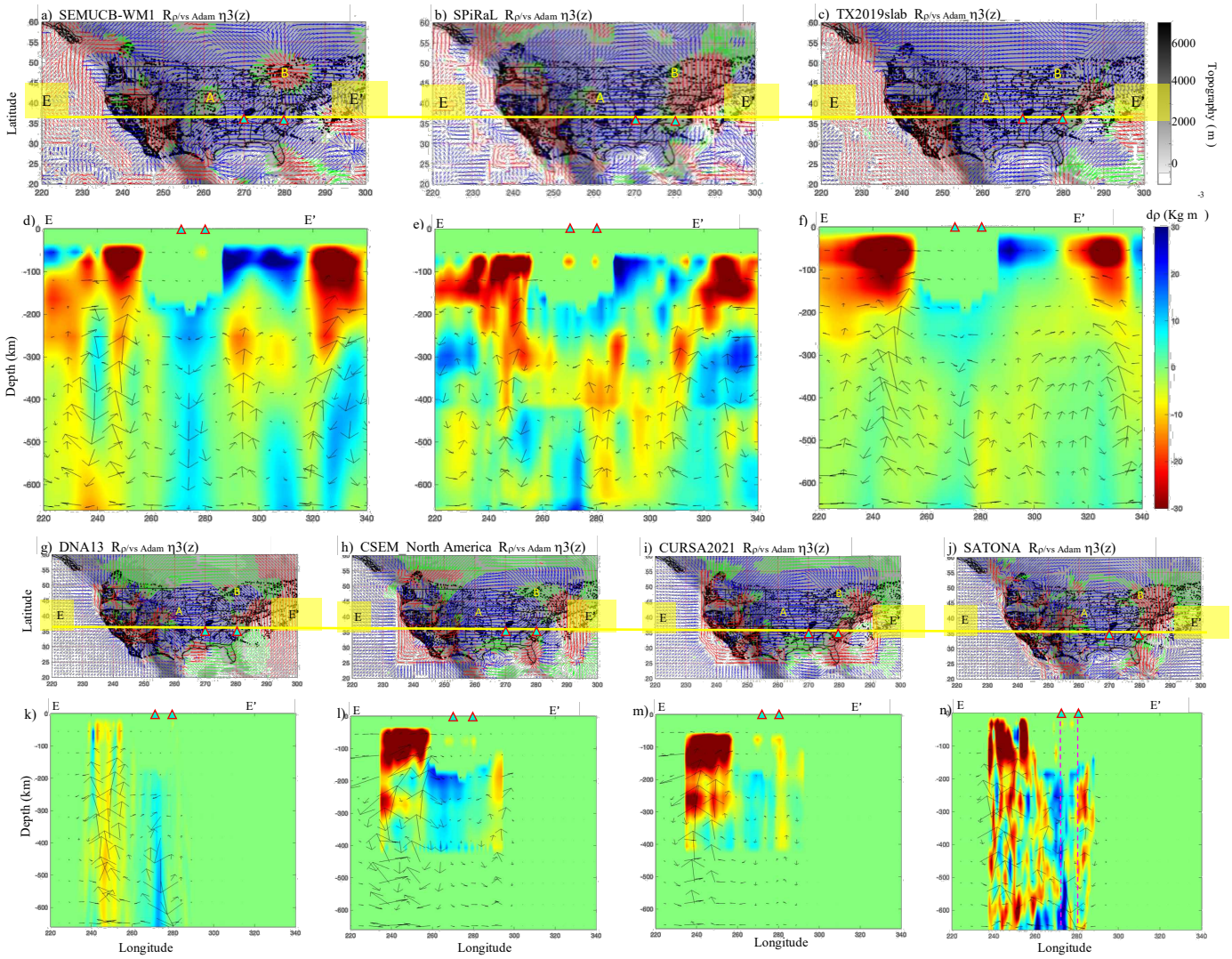

Appendix Figure 4: Modeled tectonic regimes at depth 99 km using the SEMUCB-WM1 tomography model (French & Romanowicz, 2014), (a), SPiRaL tomography model (Simmons et al., 2021), (b), TX2019slab tomography model (Lu et al., 2019), (c) DNA13 (Porritt et al., 2014), (g), CURSA2021 (Zhou et al., 2022), (h), CSEM_North_America (Fichtner et al., 2018), (i) and SATONA (Hua et al., 2025), (j). The models use the same depth dependent viscosity (viscosity law $\eta_3(Z)$, section 3.1), based on the CAM2022 lithosphere thickness (Priestley et al., 2024). Corresponding depth cross-sections of the density anomalies and the induced mantle flow are shown at latitude 36°N in panels d-f and g-j. Triangles mark the zone between NMSZ and ETSZ.

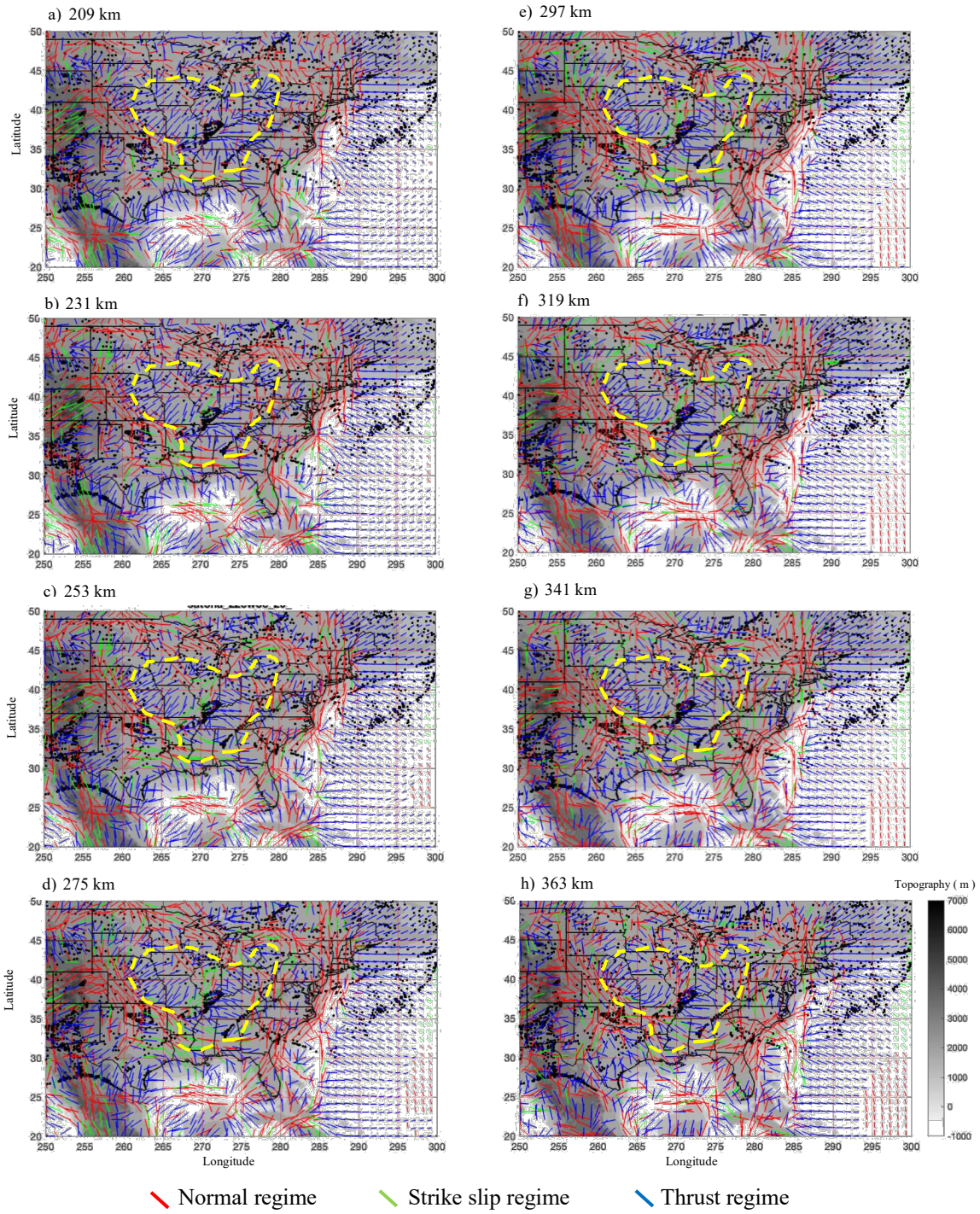

Appendix Figure 5: Modeled tectonic regimes at depths greater than 200 km for SATONA regional tomography model (Hua et al., 2025). The model use depth dependent viscosity (viscosity law $\eta_3(Z)$, section 3.1), based on the CAM2022 lithosphere thickness (Priestley et al., 2024). Yellow dashed line represents the dripping high Vs body region found by Hua et al. (2025).

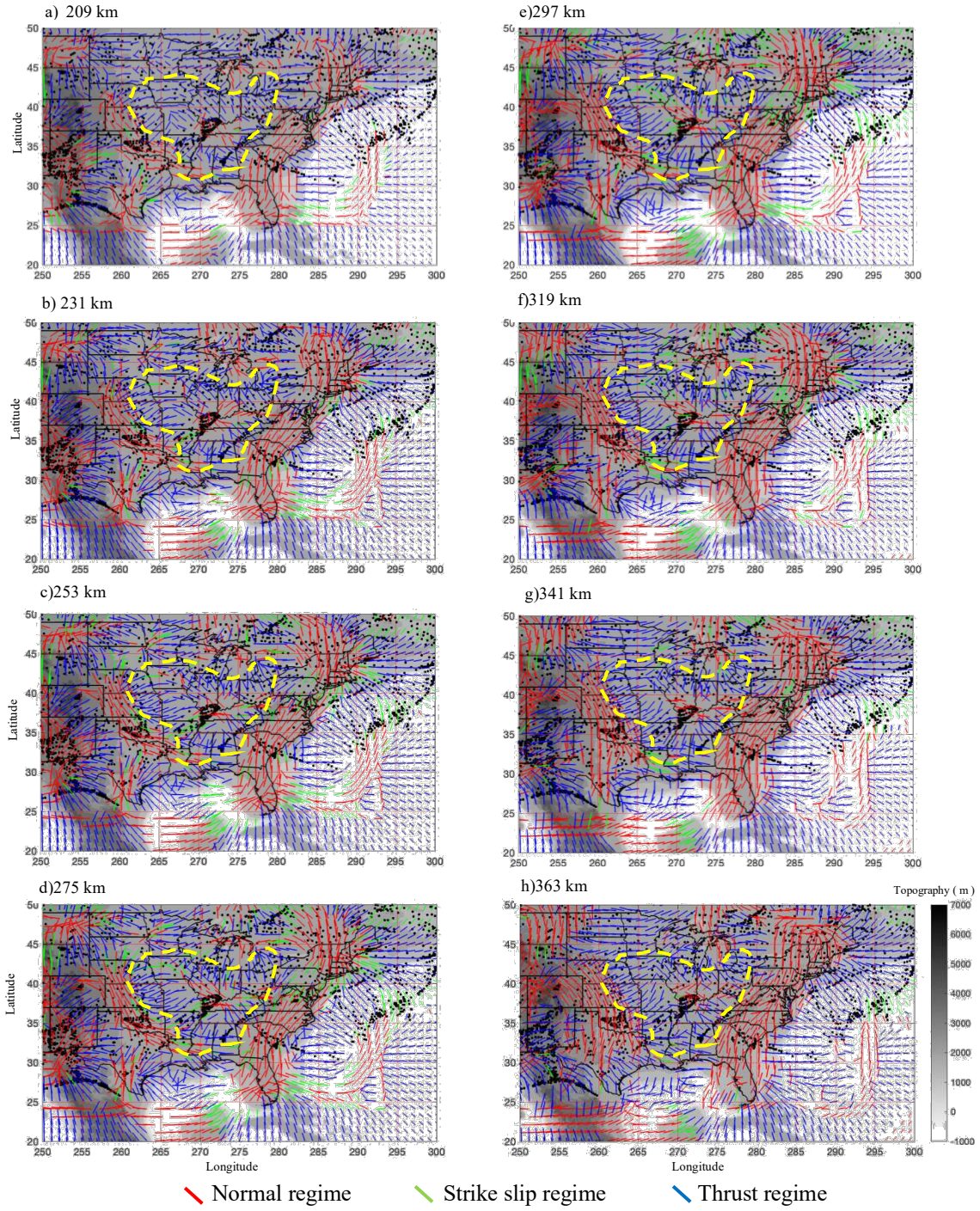

Appendix Figure 6: Modeled tectonic regimes at depths greater than 200 km for CURSA2021 regional tomography model (Zhou et al., 2022). The model use depth dependent viscosity (viscosity law $\eta_3(Z)$, section 3.1), based on the CAM2022 lithosphere thickness (Priestley et al., 2024). Yellow dashed line represents the dripping high Vs body region found by Hua et al. (2025).

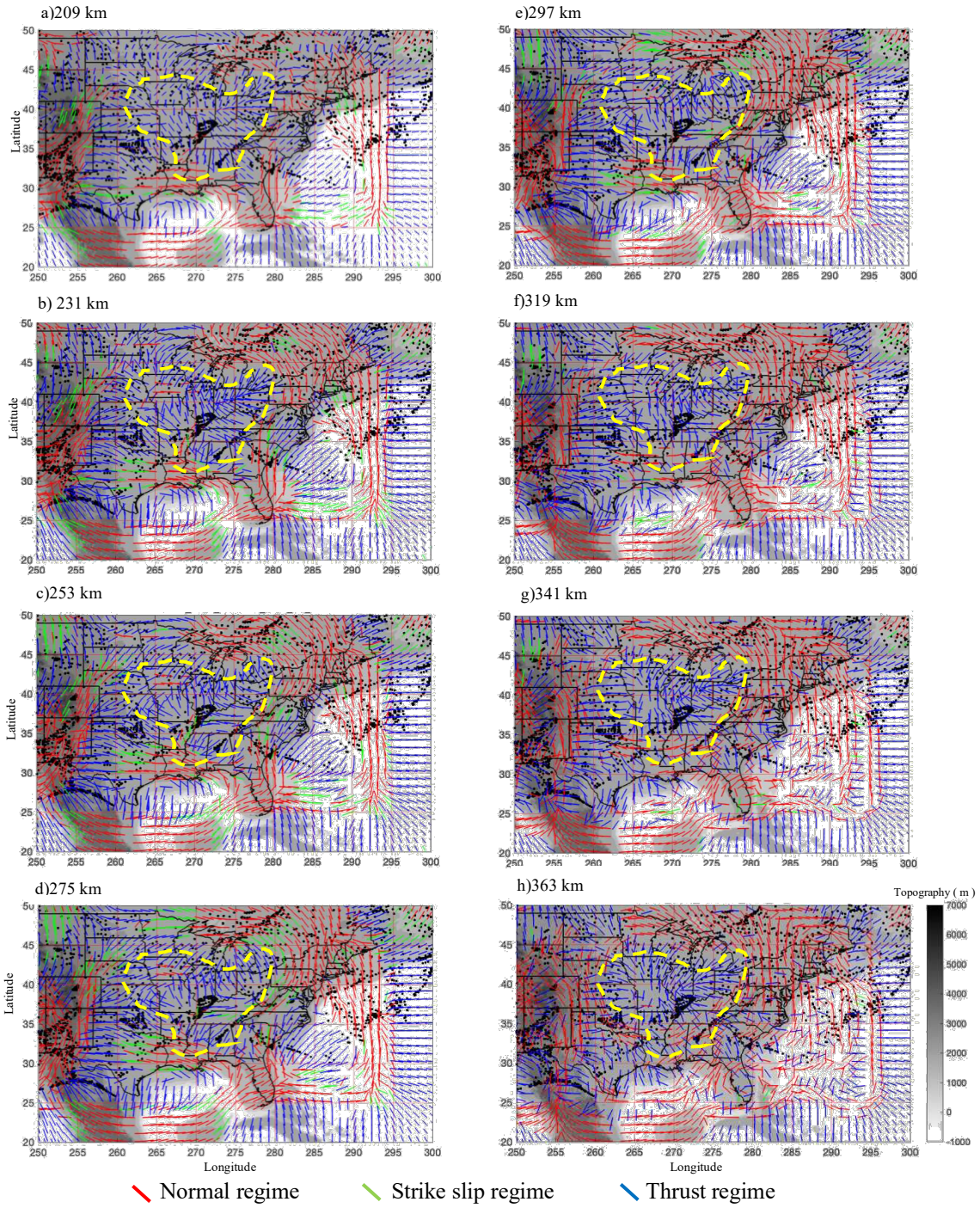

Appendix Figure 7: Modeled tectonic regimes at depths greater than 200 km for CSEM_North_America regional tomography model (Fichtner et al., 2018). The model use depth dependent viscosity (viscosity law $\eta_3(Z)$, section 3.1), based on the CAM2022 lithosphere thickness (Priestley et al., 2024). Yellow dashed line represents the dripping high Vs body region found by Hua et al. (2025).

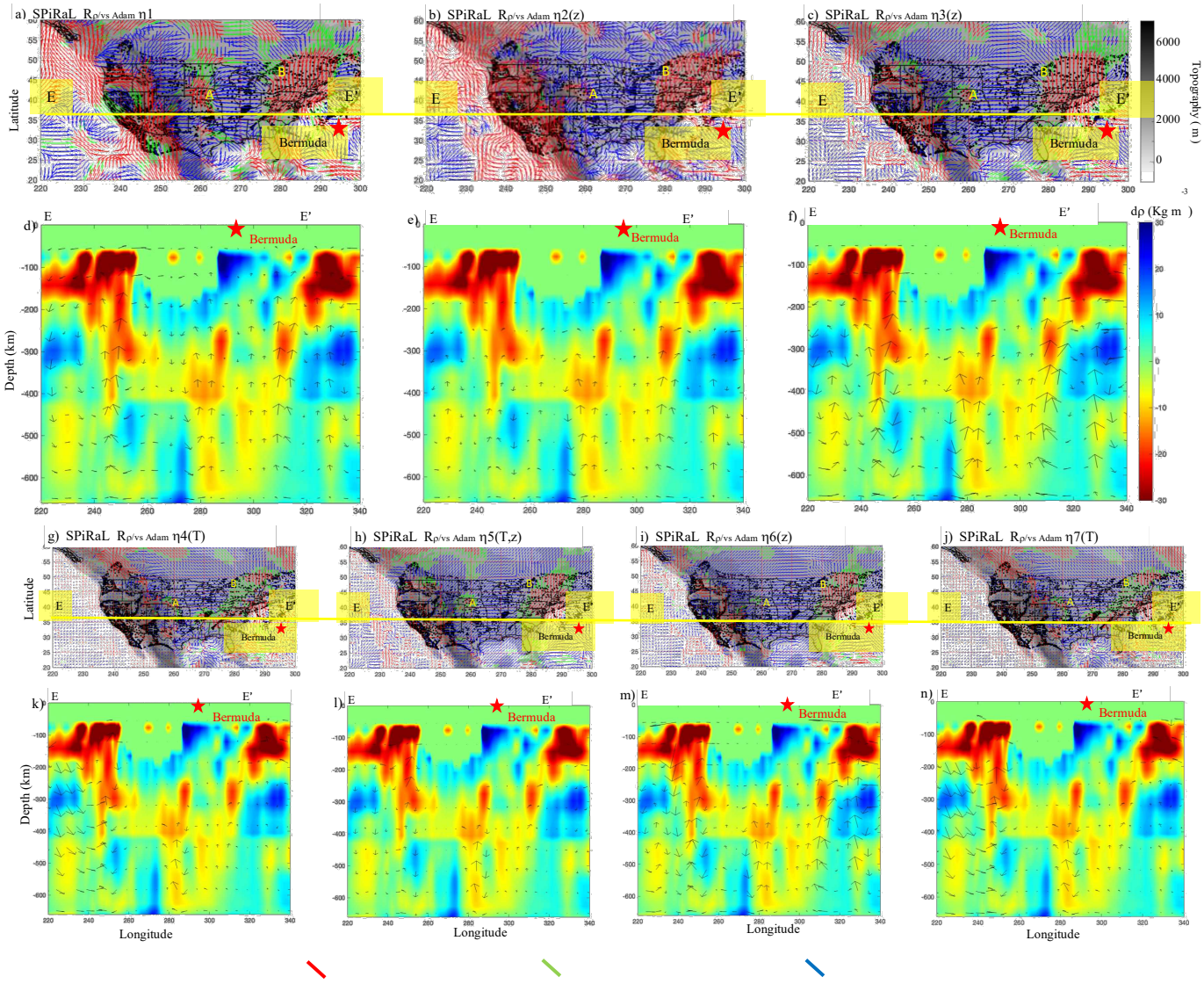

Appendix Figure 8: Modeled tectonic regimes at 99 km depth with different viscosity laws using SPiRaL tomography model (Simmons et al., 2021). (a) constant viscosity(η_1), (b) depth dependent viscosity with 100 km thick lithosphere ($\eta_2(Z)$), (c) depth dependent viscosity with LAB CAM2022 ($\eta_3(Z)$), (g) temperature dependent viscosity ($\eta_4(T)$), (h) depth and temperature dependent viscosity ($\eta_5(T,Z)$), (i) depth dependent viscosity with WPB ($\eta_6(Z)$) and (j) temperature dependent viscosity with WPB ($\eta_7(T)$). The conversion factor between seismic velocity anomalies and density anomalies, $R_{\rho/vs}$ is from Adam et al. (2021). Corresponding depth cross-sections are shown at latitude 36°N in panels d-f and k-n.

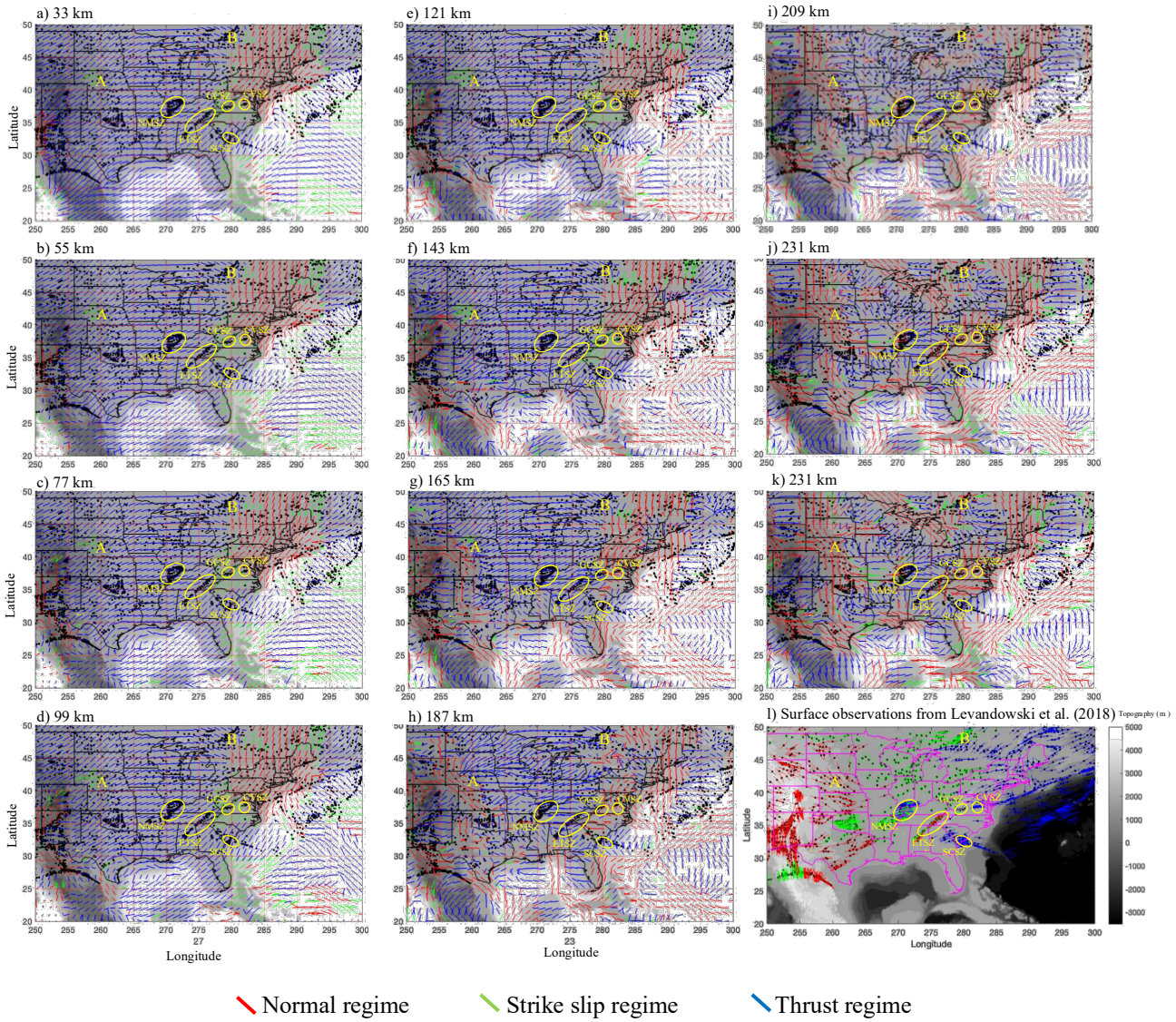

Appendix Figure 9: Variation of tectonic regimes with depth for the SPiRaL tomography model (Simmons et al., 2021) across the Central and Eastern United States (CEUS). The viscosity is depth dependent based on CAM2022 model with WPB(viscosity law $\eta_6(Z)$, section 3.1) and the $R_{\rho/vs}$ is from Adam et al. (2021). Circled areas are the Basin and Range - Rio Grande Rift (BR-RGR) and the major seismic zones, including New Madrid Seismic Zone (NMSZ), Eastern Tennessee Seismic Zone (ETSZ), South Carolina Seismic Zone (SCSZ), Giles County Seismic Zone (GCSZ) and Central Virginia Seismic Zone (CVSZ). Panels a-k: each panel shows the modeled tectonic regimes (see color scale legend) and the SH_{max} directions at depths reported on top of each panel. Black dots: seismicity from Levandowski et al. (2018). l) Surface observations taken from Levandowski et al. (2018). The black (a-k) and magenta (l) lines mark state boundaries (https://www.census.gov/geographies/mapping-files/time-series/geo/carto-boundary-file.html).